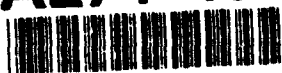


PL-TR-93-2179

AD-A274 461

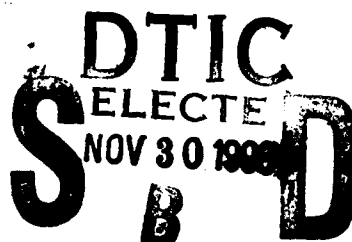


**ZODIACAL LIGHT DATA INVESTIGATION.
INTERIM RESULTS FOR THE EARTHLIMB
CLUTTER EXPERIMENT**

Wesley K. Cobb
Shawn V. Burdick
Thomas L. Murdock

General Research Corporation
5 Cherry Hill Drive, Suite 220
Danvers, Massachusetts 01923

15 July 1993



Scientific Report No. 1

Approved for public release; distribution unlimited



PHILLIPS LABORATORY
Directorate of Geophysics
AIR FORCE MATERIEL COMMAND
HANSCOM AIR FORCE BASE, MA 01731-3010

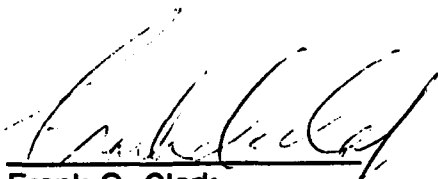
93-29092



93 11 26 145

422816

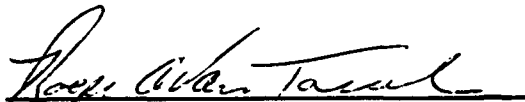
This technical report has been reviewed and is approved for publication.



Frank O. Clark
Contract Manager



Stephan D. Price
Branch Chief



Roger van Tassel
Division Director

This report has been reviewed by the ESC Public Affairs Office (PA) and is releasable to the National Technical Information Service (NTIS).

Qualified requestors may obtain additional copies from the Defense Technical Information Center. All others should apply to the National Technical Information Service.

If your address has changed, or if you wish to be removed from the mailing list, or if the addressee is no longer employed by your organization, please notify PL/TSI, Hanscom AFB, MA 01731-3010. This will assist us in maintaining a current mailing list.

Do not return copies of this report unless contractual obligations or notices on a specific document requires that it be returned.

REPORT DOCUMENTATION PAGE

Form Approved
OMB No. 0704-0188

Public reporting burden for this collection of information is estimated to average 1 hour per response, including the time for reviewing instructions, searching existing data sources, gathering and maintaining the data needed, and completing and reviewing the collection of information. Send comments regarding this burden estimate or any other aspect of this collection of information, including suggestions for reducing this burden, to Washington Headquarters Services, Directorate for Information Operations and Reports, 1215 Jefferson Davis Highway, Suite 1204, Arlington, VA 22202-4302, and to the Office of Management and Budget, Paperwork Reduction Project (0704-0188), Washington, DC 20503.

1. AGENCY USE ONLY (Leave blank)		2. REPORT DATE 15 July 1993	3. REPORT TYPE AND DATES COVERED Scientific No. 1	
4. TITLE AND SUBTITLE ZODIACAL LIGHT DATA INVESTIGATION INTERIM RESULTS FOR THE EARTHLIMB CLUTTER EXPERIMENT			5. FUNDING NUMBERS F19628-91-C-0104 PE 62101F PR3054 TA 01 WUAR	
6. AUTHOR(S) Wesley K. Cobb Shawn V. Burdick Thomas L. Murdock				
7. PERFORMING ORGANIZATION NAME(S) AND ADDRESS(ES) General Research Corporation 5 Cherry Hill Drive, Suite 220 Danvers, Massachusetts 01923			8. PERFORMING ORGANIZATION REPORT NUMBER 1949-01-93-TR	
9. SPONSORING/MONITORING AGENCY NAME(S) AND ADDRESS(ES) Phillips Laboratory 29 Randolph Road Hanscom AFB, MA 01731-3010 Contract Manager: Frank Clark/GPOB			10. SPONSORING/MONITORING AGENCY REPORT NUMBER PL-TR-93-2179	
11. SUPPLEMENTARY NOTES				
12a. DISTRIBUTION/AVAILABILITY STATEMENT Approved for public release; distribution unlimited			12b. DISTRIBUTION CODE	
13. ABSTRACT (Maximum 200 words) Zodiacal light data from the Earth Limb Clutter experiment (ELC) have been analyzed and compared with IRAS observations in order to bring the former into a common calibration framework with COBE and IRAS. There were 9 ELC spectral bands, 2 of which were broad (12 and 26 microns), and 7 of which were narrow (5.6, 9.6, 10.6, 11.5, 12.5, 13.7, 15.2 microns). The ELC data appeared to show considerable spectral structure in the zodiacal light for 9-15 micron regime. The recalibrated ELC data are also important because they contain zodiacal plane crossings at low (19°) and high (167°) solar elongations -- regions not accessible to IRAS or COBE. The antisolar crossing is particularly interesting because it is associated with nearly symmetrically placed secondary peaks at $\pm 28^\circ$ ecliptic latitude. Possible origins for these peaks are discussed.				
14. SUBJECT TERMS Zodiacal Light, Zodiacal Dustbands, Zodiacal Dust Spectra, IRAS, COBE, ELC			15. NUMBER OF PAGES 76	
			16. PRICE CODE	
17. SECURITY CLASSIFICATION OF REPORT Unclassified	18. SECURITY CLASSIFICATION OF THIS PAGE Unclassified	19. SECURITY CLASSIFICATION OF ABSTRACT Unclassified	20. LIMITATION OF ABSTRACT SAR	

CONTENTS

Acknowledgements	ix
Acronyms	xi
Foreword	xiii
1. INTRODUCTION	1
1.1 Focal Plane Temperature Effects	2
1.2 Atmospheric Radiance	2
1.3 Outgassing Contamination	2
1.4 Ground Calibration	3
2. THE ELC REPROCESSING	6
2.1 Ingestion	6
2.2 Spike Extraction	14
2.3 Lowpass Filter	20
2.4 Coaddition	26
2.5 Atmosphere Corrections	31
2.6 Renormalization	33
2.6.1 Color Corrections	35
2.7 Smoothing	37
3. DISCUSSION	48
4. SUMMARY	53
References	54
Appendix A: ELC DETECTOR COMPARISONS	55

DTIC QUALITY INSPECTED 8

Accession For	
NTIS GRA&I	<input checked="checked" type="checkbox"/>
DTIC TAB	<input type="checkbox"/>
Unannounced	<input type="checkbox"/>
Justification	
By _____	
Distribution/ _____	
Availability Codes	
Dist	Avail and/or Special
A-1	

LIST OF FIGURES

NUMBER		PAGE
1.	ELC sensor/spacecraft configuration.	4
2.	ELC focal plane layout.	4
3.	Aitoff projection of the ELC Long Roll in Zodiacal Coordinates.	5
4.	Aitoff projection of the ELC Long Roll in Galactic Coordinates.	5
5.	The unprocessed raw data for ELC Band 1 (5.6 μ). The two panels correspond to the detectors which comprise Band 1.	9
6.	The unprocessed raw data for ELC Band 2 (9.6 μ). The two panels correspond to the detectors which comprise Band 2.	9
7.	The unprocessed raw data for ELC Band 3 (10.6 μ). The two panels correspond to the detectors which comprise Band 3.	10
8.	The unprocessed raw data for ELC Band 4 (11.5 μ). The two panels correspond to the detectors which comprise Band 4.	10
9.	The unprocessed raw data for ELC Band 5 (12.0 μ). The four panels correspond to the detectors which comprise Band 5.	11
10.	The unprocessed raw data for ELC Band 6 (12.5 μ). The two panels correspond to the detectors which comprise Band 6.	12
11.	The unprocessed raw data for ELC Band 7 (13.7 μ). The two panels correspond to the detectors which comprise Band 7.	12
12.	The unprocessed raw data for ELC Band 8 (15.2 μ). The four panels correspond to the detectors which comprise Band 8.	13
13.	The unprocessed raw data for ELC Band 9 (26.3 μ). The two panels correspond to the detectors which comprise Band 9.	14
14.	The data for ELC Band 1 after despiking. The two panels correspond to the detectors which comprise Band 1.	15
15.	The data for ELC Band 2 after despiking. The two panels correspond to the detectors which comprise Band 2.	15
16.	The data for ELC Band 3 after despiking. The two panels correspond to the detectors which comprise Band 3.	16
17.	The data for ELC Band 4 after despiking. The two panels correspond to the detectors which comprise Band 4.	16
18.	The data for ELC Band 5 after despiking. The four panels correspond to the detectors which comprise Band 5.	17
19.	The data for ELC Band 6 after despiking. The two panels correspond to the detectors which comprise Band 6.	18

LIST OF FIGURES

NUMBER		PAGE
20.	The data for ELC Band 7 after despiking. The two panels correspond to the detectors which comprise Band 7.	18
21.	The data for ELC Band 8 after despiking. The four panels correspond to the detectors which comprise Band 8.	19
22.	The data for ELC Band 9 after despiking. The two panels correspond to the detectors which comprise Band 9.	20
23.	Composite of the lowpass filtered data for the two detectors making up ELC Band 1.	21
24.	Composite of the lowpass filtered data for the two detectors making up ELC Band 2.	22
25.	Composite of the lowpass filtered data for the two detectors making up ELC Band 3.	22
26.	Composite of the lowpass filtered data for the two detectors making up ELC Band 4.	23
27.	Composite of the lowpass filtered data for the four detectors making up ELC Band 5.	23
28.	Composite of the lowpass filtered data for the two detectors making up ELC Band 6.	24
29.	Composite of the lowpass filtered data for the two detectors making up ELC Band 7.	24
30.	Composite of the lowpass filtered data for the four detectors making up ELC Band 8.	25
31.	Composite of the lowpass filtered data for the two detectors making up ELC Band 9.	25
32.	Coadded data for ELC Band 1.	27
33.	Coadded data for ELC Band 2.	27
34.	Coadded data for ELC Band 3.	28
35.	Coadded data for ELC Band 4.	28
36.	Coadded data for ELC Band 5.	29
37.	Coadded data for ELC Band 6.	29
38.	Coadded data for ELC Band 7.	30
39.	Coadded data for ELC Band 8.	30
40.	Coadded data for ELC Band 9.	31
41.	Plots showing the model atmospheric radiance curves derived from FAUST and used in making the atmospheric corrections.	32

LIST OF FIGURES

NUMBER		PAGE
42.	IRAS data for the date of the ELC flight. Each curve is a superposition of 4 separate sweeps made by IRAS. The upper curve corresponds to IRAS Band 1 (12 μ), while the lower curve represents IRAS Band 2 (25 μ) data.	34
43.	Recalibrated data for ELC Band 1 (5.6 μ).	37
44.	Recalibrated data for ELC Band 2 (9.6 μ).	38
45.	Recalibrated data for ELC Band 3 (10.6 μ).	38
46.	Recalibrated data for ELC Band 4 (11.5 μ).	39
47.	Recalibrated data for ELC Band 5 (12.0 μ).	39
48.	Recalibrated data for ELC Band 6 (12.5 μ).	40
49.	Recalibrated data for ELC Band 7 (13.7 μ).	40
50.	Recalibrated data for ELC Band 8 (15.2 μ).	41
51.	Recalibrated data for ELC Band 9a (26.3 μ). The calibration used for Band 9a is based on the FAUST model used for Bands 1 - 8. See the discussion in the text.	41
52.	Recalibrated data for ELC Band 9b (26.3 μ). The calibration used for Band 9b is based on a power law model rather than the FAUST model. See the discussion in the text.	42
53.	Smoothed, recalibrated ELC data for Band 1.	42
54.	Smoothed, recalibrated ELC data for Band 2.	43
55.	Smoothed, recalibrated ELC data for Band 3.	43
56.	Smoothed, recalibrated ELC data for Band 4.	44
57.	Smoothed, recalibrated ELC data for Band 5.	44
58.	Smoothed, recalibrated ELC data for Band 6.	45
59.	Smoothed, recalibrated ELC data for Band 7.	45
60.	Smoothed, recalibrated ELC data for Band 8.	46
61.	Smoothed, recalibrated ELC data for Band 9a.	46
62.	Smoothed, recalibrated ELC data for Band 9b.	47
63.	Surface plot showing ELC sensor response (10^{-12} W/cm ² -sr - μ) as a function of time and wavelength. The temporal response is derived from the recalibrated ELC data using a bilinear rebinning which reduces the data resolution by a factor of 100.	51
64.	Surface plot showing ELC sensor response (10^{-12} W/cm ² -sr - μ) as a function of time and wavelength, but with the projection chosen to emphasize the spectral features in the data.	51

LIST OF FIGURES

NUMBER		PAGE
65.	Spectrum of the zodiacal plane as measured by ELC in the near sun crossing at 158s TALO.	52
66.	Spectrum of the zodiacal plane and putative 'dust-band' features measured by ELC.	52
A-1	Detector responses for ELC Band 1. The left hand panel shows detector 21 plotted against detector 22. The right hand panel shows the time evolution of the ratio of the two detector signals.	55
A-2	Detector responses for ELC Band 2. The left hand panel shows detector 11 plotted against detector 12. The right hand panel shows the time evolution of the ratio of the two detector signals.	56
A-3	Detector responses for ELC Band 3. The left hand panel shows detector 13 plotted against detector 14. The right hand panel shows the time evolution of the ratio of the two detector signals.	56
A-4	Detector responses for ELC Band 4. The left hand panel shows detector 29 plotted against detector 30. The right hand panel shows the time evolution of the ratio of the two detector signals.	57
A-5	Detector responses for ELC Band 5. The left hand panel shows detector 19 plotted against detector 20. The right hand panel shows the time evolution of the ratio of the two detector signals.	57
A-6	Detector responses for ELC Band 5. The left hand panel shows detector 19 plotted against detector 25. The right hand panel shows the time evolution of the ratio of the two detector signals.	58
A-7	Detector responses for ELC Band 5. The left hand panel shows detector 20 plotted against detector 26. The right hand panel shows the time evolution of the ratio of the two detector signals.	58
A-8	Detector responses for ELC Band 6. The left hand panel shows detector 3 plotted against detector 4. The right hand panel shows the time evolution of the ratio of the two detector signals.	59
A-9	Detector responses for ELC Band 7. The left hand panel shows detector 9 plotted against detector 10. The right hand panel shows the time evolution of the ratio of the two detector signals.	59
A-10	Detector responses for ELC Band 8. The left hand panel shows detector 15 plotted against detector 16. The right hand panel shows the time evolution of the ratio of the two detector signals.	60
A-11	Detector responses for ELC Band 8. The left hand panel shows detector 15 plotted against detector 31. The right hand panel shows the time evolution of the ratio of the two detector signals.	60

LIST OF FIGURES

<u>NUMBER</u>		<u>PAGE</u>
A-12	Detector responses for ELC Band 8. The left hand panel shows detector 16 plotted against detector 32. The right hand panel shows the time evolution of the ratio of the two detector signals.	61
A-13	Detector responses for ELC Band 9. The left hand panel shows detector 27 plotted against detector 28. The right hand panel shows the time evolution of the ratio of the two detector signals.	61
A-14	Diagram showing improvement in detector vs. detector behavior after cleaning and despiking for representative pair of detectors within the same band.	62

LIST OF TABLES

<u>NUMBER</u>		<u>PAGE</u>
1.	ELC Wavelength Bands	7
2.	ELC Color Corrections @ T=280K	35
3.	ELC - IRAS Comparison	36

ACKNOWLEDGEMENTS

We wish to thank Dr. Stephan Price, Dr. John Eoll, and Dr. John Chalupa for helpful discussions and suggestions. In addition, Dr. Frank Clark helped us obtain the CBSD/PC and FAUST, which was used in making atmospheric corrections. Tony D'Agati was of great assistance in coping with the arcana of Cyber tapes and files and Joe Flaherty did much of the actual ingestion work. Rebecca Sample, Rose Korté, and Jack Kenneally of MRC/Nashua helped us obtain the IRAS 2 arcminute Zodiacal History Files. Finally, we wish to thank Alison Zweil and Michelle Cote for their help in the production of this report.

THIS PAGE INTENTIONALLY LEFT BLANK

ACRONYMS

CBSD	Celestial Background Scene Descriptor
COBE	Cosmic Background Explorer
DIRBE	Diffuse Infrared Background Experiment
DN	Digital Number
ELC	Earthlimb Clutter
FAUST	Fast Atmospheric Synthesis Technique
IR	Infrared
IRAS	Infrared Astronomical Satellite
LOS	Line-Of-Sight
NEP	North Ecliptic Pole
OFVR	Out of Field of View Rejection
SEP	South Ecliptic Pole
SOP	Standard Observing Period
ZIP	Zodiacal Infrared Project
ZOHF	Zodiacal History File (IRAS)

THIS PAGE INTENTIONALLY LEFT BLANK

FOREWORD

This work has been performed under contract with the Air Force's Phillips Laboratory under the supervision of Dr. Stephan D. Price. The goal of the contract is to re-examine the zodiacal light data taken from several Air Force sounding rocket flights made during the 1970's and 1980's, and where possible, bring the data from those flights into a common calibration framework with the (generally) later data from IRAS and Cosmic Background Explorer (COBE) / Diffuse Infrared Background Experiment (DIRBE).

The flights under consideration include the Earthlimb Clutter Experiment (ELC), the Zodiacal Infrared Project (two flights: ZIP-1, ZIP-2), the Earthlimb Experiment, and High Star South.

This particular report is intended to present a summary of work done on ELC during the first contract year of the project. Over the course of this period, we have developed and applied despiking, lowpass filtering, atmospheric correction, and coaddition algorithms to the synchronously rectified and decommutated ELC data. The data were then renormalized against IRAS data taken on the day of the ELC flight. The renormalized data were then smoothed and subjected to a quick look analysis. Possible off-axis rejection and outgassing contamination effects have not been considered thus far, since the models for these effects will be developed using the ZIP data sets. An interim 'quick look' analysis of the data has been made and several potentially important features of the ELC data are discussed. We caution the reader that any report of this sort necessarily represents a snapshot of the project in time: as understanding of issues and problems evolves, results and interpretations discussed herein may evolve also.

THIS PAGE INTENTIONALLY LEFT BLANK

1 INTRODUCTION

The Earthlimb Clutter Experiment (ELC) was flown on an Aries sounding rocket in October 1983 from White Sands, New Mexico. Figure 1 shows the ELC spacecraft configuration with the sensor deployed. The sensor was uncovered approximately 90s into the flight at an altitude of 115 km, and took data for some 500s. The ELC sensor consisted of an off-axis Gregorian telescope with a 10x20 cm D-shaped primary mirror. The focal plane array had 32 detectors (spread over 11 spectral bands) spanning the infrared (IR) domain from 4-30 μm . In fact, the ELC sensor used the same optics and calibration plate as Zodiacal Infrared Project-1 (ZIP) and ZIP-2, but the focal plane had been modified by the replacement of new detectors and new filters. The ELC focal plane layout is shown in Figure 2.

During the data collection period the payload followed a northward trajectory with an apogee of 300 km. The sensor completed an initial "long roll" through 430° in the instantaneous local horizontal plane, and then performed a series of vertical and horizontal sweeps in and out of the earth limb. The sensor was then returned to a fixed attitude in order to capture an atmospheric profile prior to reentry. While the primary purpose of the experiment (as the name implies) was to gather detailed information about the nature and spatial frequency of clutter in the earthlimb, the approximately 60 seconds of data gathered during the initial "long roll" (early in the mission) is pertinent to the study of the zodiacal background.

The zodiacal data obtained by ELC were gathered with the spacecraft oriented northward -- a geometry chosen for the purpose of avoiding any potential contamination effects associated with the rocket booster trailing behind the sensor to the south.

ELC's zodiacal data is unique because of its spatial coverage: during the long roll, the sensor line-of-sight (LOS) scanned across the zodiacal plane at nearly right angles and only 19° away from the sun -- far closer to the sun than Infrared Astronomical Satellite (IRAS) and Cosmic Background Explorer (COBE) were able to observe. Figures 3 and 4 show the scan path of the long roll in ecliptic and galactic coordinates respectively.

The ELC observations were contemporaneous with the IRAS mission, and since two of the ELC bands were similar to the IRAS/COBE 12 and 25 μm bands, an obvious strategy for tying the ELC calibration to that of IRAS is to find places where the two spacecraft observed the same spot on the sky at nearly the same time, and to renormalize the ELC radiances to the IRAS values to force consistency between the two data sets. Since the bands are not identical, it is necessary to make color corrections.

For this study, we investigated several instrumental and phenomenological effects which are pertinent to the ELC calibration.

1.1 Focal Plane Temperature Effects. Before undertaking the reprocessing, a thorough examination of the ELC in-flight housekeeping telemetry data was made. Since data had been recorded continuously from several thermal sensors on and near the focal plane assembly, it was possible to verify that during the zodiacal scan, the focal plane temperature remained quite steady. The actual temperature dependence of the gain was characterized as part of the preflight testing^(2, 4, 5). Based on the measured dependence of the gain as a function of temperature and the thermal data from the housekeeping data, we concluded that the temperature dependence of the gain is not significant for the times of interest.

1.2 Atmospheric Radiance. The zodiacal light observations were all made during the period from 120-180s after launch as the spacecraft was rising from 150 to 240 km in altitude. The zodiacal scan geometry was essentially a single long roll through some 430 degrees in the instantaneous horizontal plane. The Fast Atmospheric Synthesis Technique (FAUST) model from the Celestial Background Scene Descriptor (CBSD) was used to model the atmospheric contributions.

1.3 Outgassing Contamination. There are two potential sources of outgassing contamination which must be considered: the sensor platform itself, and the booster used to lift the sensor above the atmosphere. The ELC sensor platform was virtually identical to the sensor platform used in ZIP, and since ELC was also flown on a booster similar to the boosters used for the ZIP flights, we have deferred attempting to make outgassing corrections in ELC until we have completed the development of the outgassing model for ZIP. The Aries solid-rocket booster is known to continue producing exhaust residues for several minutes after burn-out⁽⁹⁾. Since each of the ZIP flights gathered data from numerous zodiacal plane and pole region observations spread

over the course of their respective flights, the ZIP data are better suited to analyzing the outgassing problem than the ELC data are. Analyzing the temporal behaviour of the lower end of the ZIP data range (corresponding to observations far away from the zodiacal and/or galactic planes) for evidence of a monotonically decreasing background should enable us to identify any outgassing problems which may be present.

1.4 Ground Calibration. We had hoped to begin with the original digital ground calibration data and perform a completely independent calibration of the data *ab initio*. Unfortunately, the original digital records of the calibration data seem to have been lost over the years. Since we did have access to the paper records detailing the calibration, we performed an independent check of the original solution using the calibration data read directly from the detector response curves and the calibration plate data.

In comparing the resulting curves for radiance as a function of measured voltage we find that our calibration agrees with the original calibration to within a few percent in almost all cases. Where there are discrepancies, they are attributable to our more pessimistic assumptions about the knowledge of the emissive properties of the "CAT-A-LAC® Black" emissive paint used on the calibration plate. Since we were not able to find any information detailing the measured properties of the particular batch of CAT-A-LAC® paint used on the plate, it would not be productive to question the choices made at the time of the experiment.

Since our derived calibration agrees closely with the original (and since we intended to renormalize the data using IRAS at any rate) we used the original calibration as our starting point.

The next chapter describes in detail the stages used in reprocessing the ELC data.

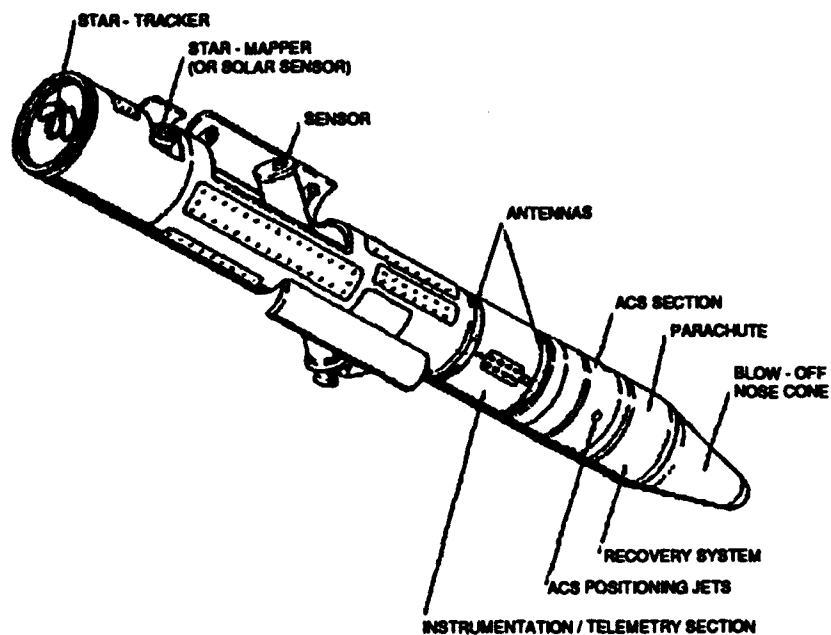


Figure 1. ELC sensor/spacecraft configuration.

<input type="checkbox"/> 29	<input type="checkbox"/> 27	26 <input type="checkbox"/>	32 <input type="checkbox"/>
<input type="checkbox"/> 30	<input type="checkbox"/> 28	25 <input type="checkbox"/>	31 <input type="checkbox"/>
<input type="checkbox"/> 23	<input type="checkbox"/> 21	20 <input type="checkbox"/>	18 <input type="checkbox"/>
<input type="checkbox"/> 24	<input type="checkbox"/> 22	19 <input type="checkbox"/>	17 <input type="checkbox"/>
<input type="checkbox"/> 9	<input type="checkbox"/> 11	14 <input type="checkbox"/>	16 <input type="checkbox"/>
<input type="checkbox"/> 10	<input type="checkbox"/> 12	13 <input type="checkbox"/>	15 <input type="checkbox"/>
<input type="checkbox"/> 7	<input type="checkbox"/> 5	4 <input type="checkbox"/>	2 <input type="checkbox"/>
<input type="checkbox"/> 8	<input type="checkbox"/> 6	3 <input type="checkbox"/>	1 <input type="checkbox"/>

↙ FPA DETECTOR DESIGNATION

SCAN DIRECTION →

Figure 2. ELC focal plane layout.

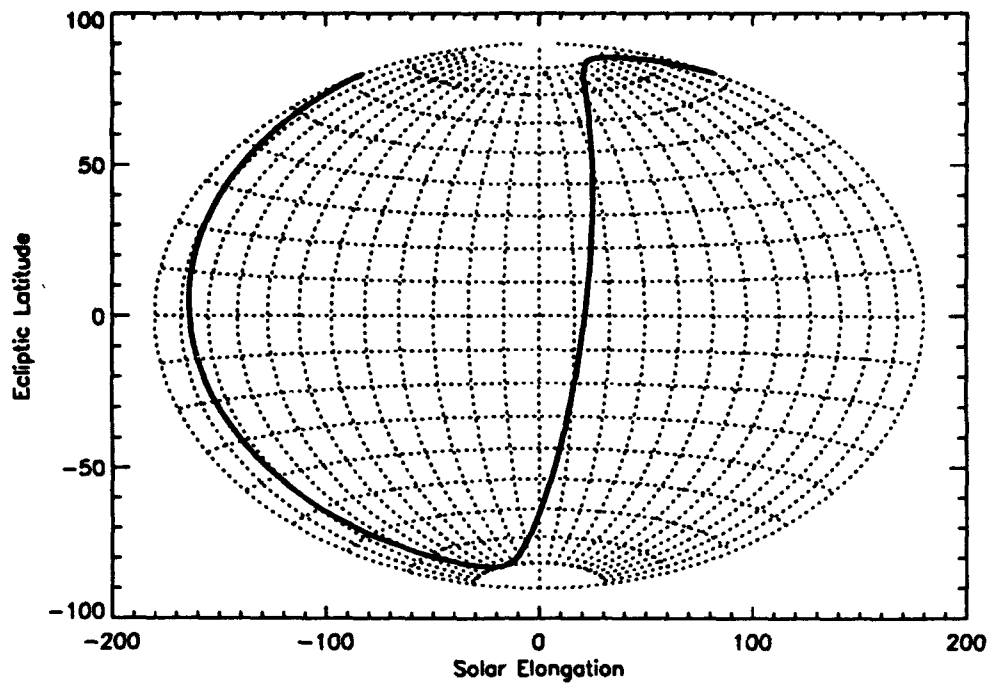


Figure 3: Aitoff projection of the ELC Long Roll in Zodiacal Coordinates.

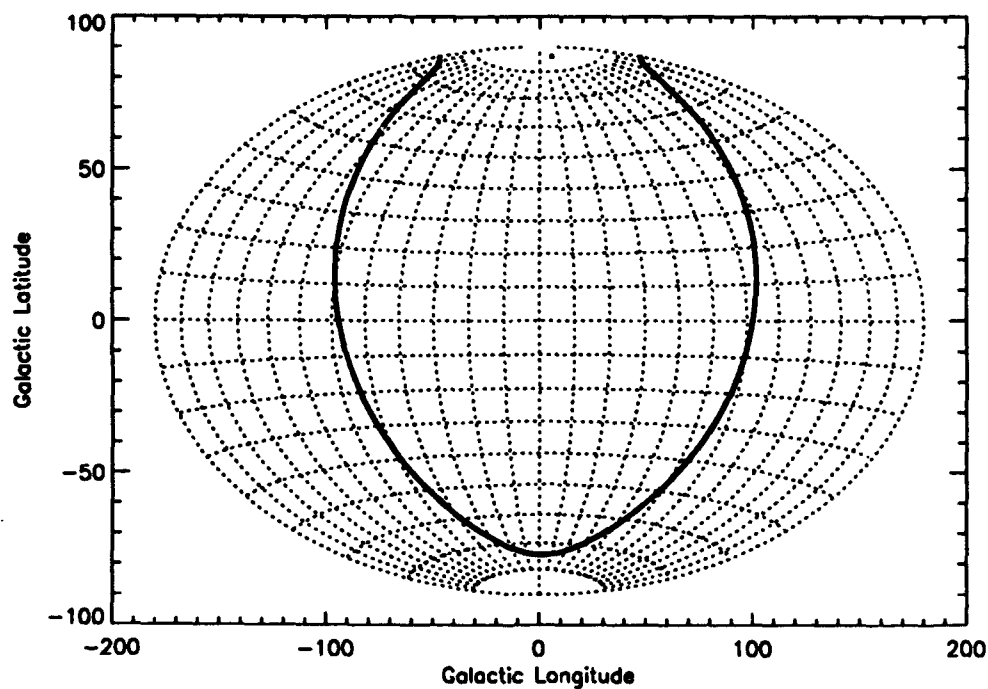


Figure 4: Aitoff projection of the ELC Long Roll in Galactic Coordinates.

2 THE ELC REPROCESSING

Our processing of the ELC digital data began with the decommutated non-spike-removed output of the original voltage data. Using the calibration as implemented by RDP Corporation⁽¹⁾ and the improved ELC aspect solution⁽⁸⁾ we produced radiance [W/cm²sr] profiles for each of the ELC detectors. These data served as the starting point for all subsequent processing. Schematically the data pipeline we implemented had the form:

INGESTION
SPIKE-EXTRACTION
LOWPASS-FILTERING
COADDITION
ATMOSPHERE SUBTRACTION
RECALIBRATION
SMOOTHING

In the balance of this chapter we explain the rationale and methodology behind each of the steps in the pipeline and graphically follow the data through the process.

2.1 INGESTION

Anthony D'Agati of Phillips Lab provided us with machine readable files containing the ELC High-Gain data and the ELC filter data. Using the improved ELC aspect solution and RDP's tools for accessing the ZIP/ELC archive format used for the files, we imported the data from the 32 ELC detectors onto our system.

From the aspect solution we were able to identify the times of zodiacal plane crossings, and sorted through the data to see which detectors had in fact observed the zodiacal light.

Detectors 1, 2, 5, 6, 7, 8, 17, 18, 23, and 24 show no evidence of the zodiacal light at all and have not been included in the subsequent analysis. The other 22 detectors do show zodiacal signatures, although the signal-to-noise ratios are very poor in some cases.

The 22 detectors which observed the zodiacal light fall into 9 spectral bands, as summarized in Table 1.

Table 1: ELC Wavelength Bands

<u>Band</u>	<u>λ</u>	<u>$\delta\lambda$</u>	<u>FPA Detector</u>
1	5.6	.92	21, 22
2	9.6	.71	11, 12
3	10.6	1.13	13, 14
4	11.5	.99	29, 30
5	12.0	7.01	19, 20, 25, 26
6	12.5	.95	3, 4
7	13.9	1.38	9, 10
8	15.2	.73	15, 16, 31, 32
9	26.2	5.63	27, 28

The full 'raw' data sets for the 22 detectors each consist of nearly 200,000 time-ordered data points spanning the period from roughly 100 s to 550 s after launch. For the purpose of the present study we were most concerned with the data from the ELC Long Roll which lasted from ~120 to ~180 s after launch. This subset of data contained approximately 19500 time-ordered data points with a temporal resolution of ~ 1/300 s. Figures 5 to 13 show plots of signal for mission times between 120 and 180 seconds for ELC bands 1 - 9.

At the suggestion of Dr. Price, as part of the ingestion procedure, we prepared diagrams showing the (as yet unreprocessed) radiance data from a given detector channel in a particular band plotted against other detector channels within the same spectral band. These diagrams are contained in the appendix to this report. For each pair of detectors, there are two plots provided: one showing the ratio of the detectors vs. time; the other showing the radiance values of the two detectors plotted against one another. The ratio plots allow one to look for systematic drifts in intra-band calibration over time. The detector vs. detector plot allows one to consider the calibration of the two detectors against one another for the sampling period spanned by the ELC Long Roll.

For times corresponding to low background signals in the radiance vs. time data, the ratios clearly show digital quantization effects. These effects appear because for sufficiently low signal strengths (e.g., 1, 2, 3, 4 Digital Numbers (DN)) the possible values which the ratios of the detector signals can take are severely limited. As expected, the quantization effects disappear as one moves to regions of higher signal strength.

The detector vs. detector plots are unsettling at first sight: they show that radiance values in one detector may differ from radiance values in another detector of the same band by several orders of magnitude. The reader is cautioned that a given point on a detector vs. detector plot near the line of unit slope typically corresponds to hundreds of data values while the points far from the unit slope line typically correspond to isolated points. Furthermore the reader is reminded that all but one of the plots in the appendix show the unfiltered, non-despiked data before gains and offsets have been corrected for.

The last figure in the Appendix (A-14) shows plots similar to the detector ratio vs. time and detector vs. detector plots but after the data have been despiked and lowpass filtered. The differences visible in the detector vs. detector plots have vanished.

Stemwedel and Rickard(10, 11) reported finding evidence for systematic drift in the intra-band calibration in ZIP, but we see no evidence for any such pathologies in the ELC data.

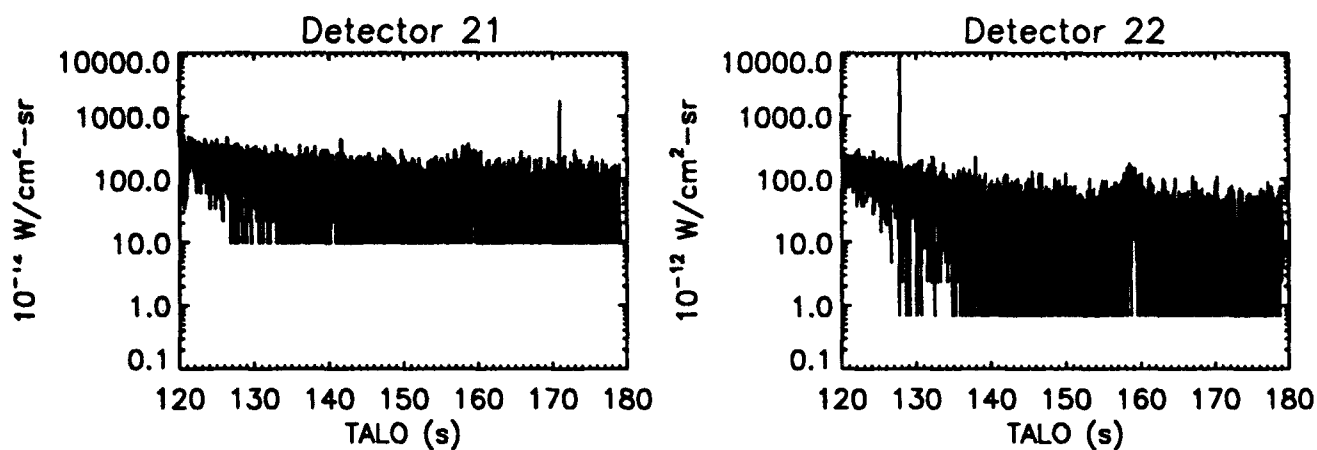


Figure 5: The unprocessed raw data for ELC Band 1 (5.6 μ). The two panels correspond to the detectors which comprise Band 1.

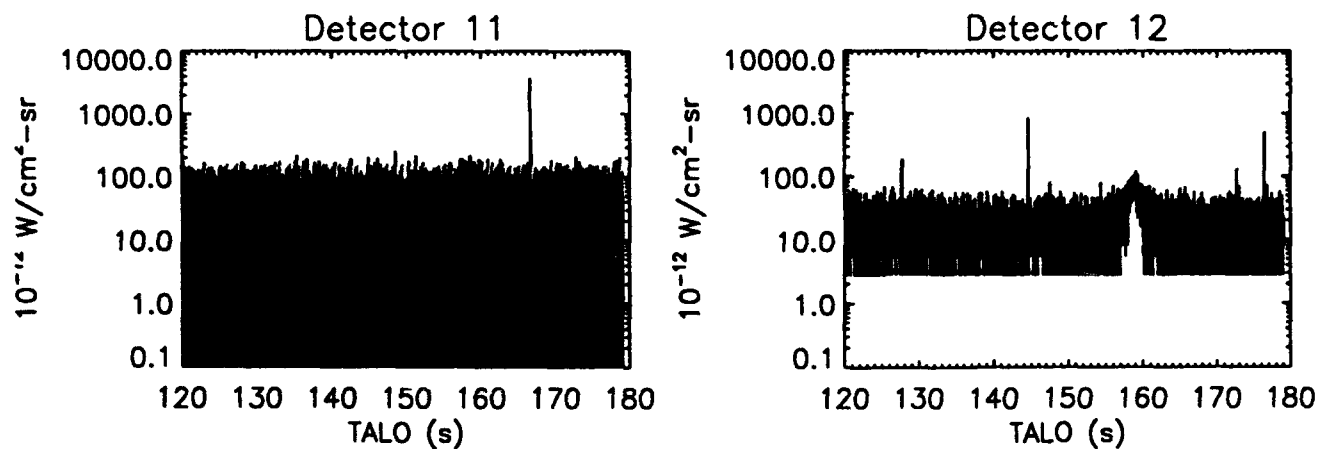


Figure 6: The unprocessed raw data for ELC Band 2 (9.6 μ). The two panels correspond to the detectors which comprise Band 2.

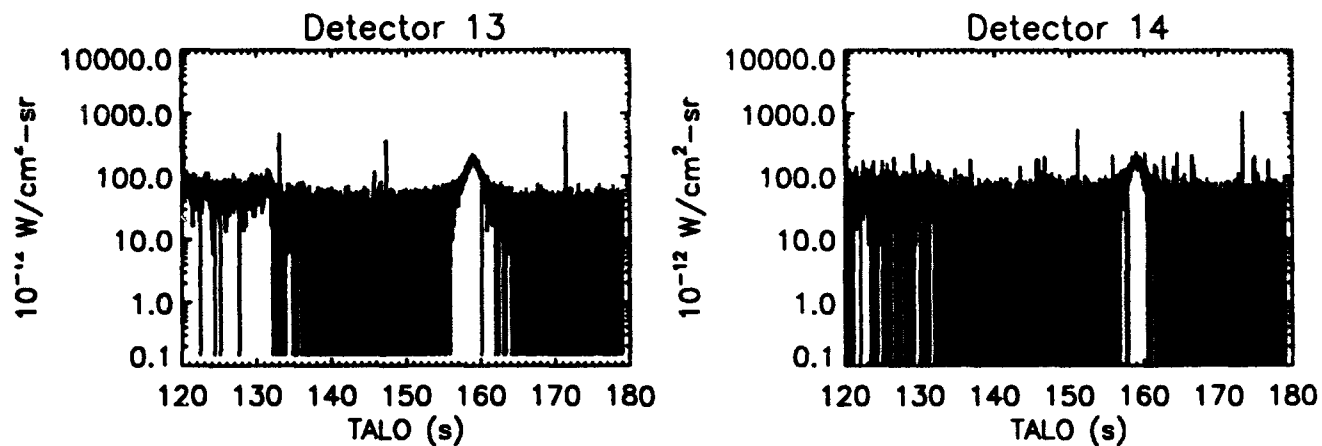


Figure 7: The unprocessed raw data for ELC Band 3 ($10.6\ \mu$). The two panels correspond to the detectors which comprise Band 3.

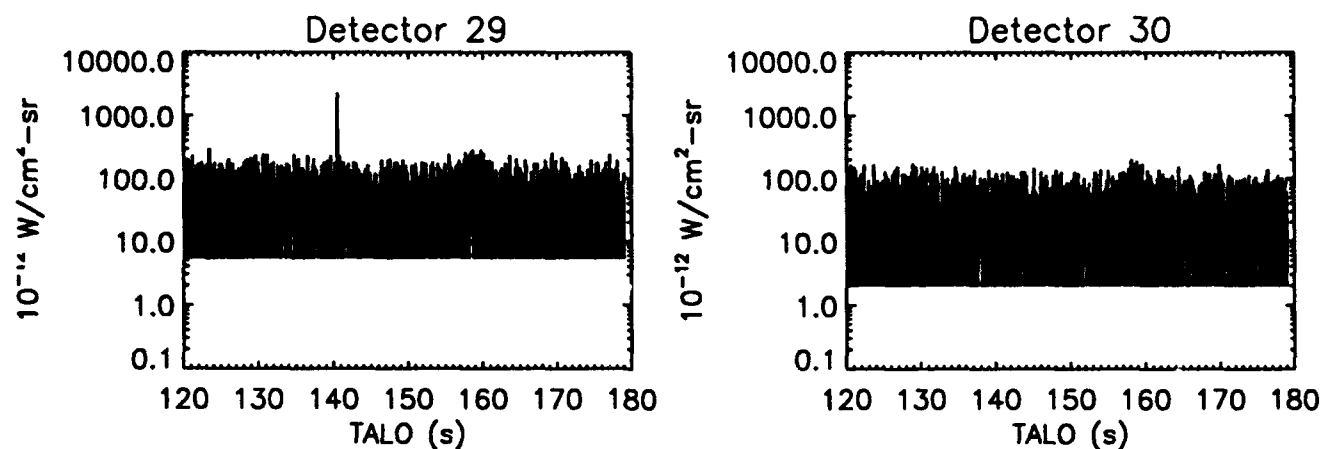


Figure 8: The unprocessed raw data for ELC Band 4 ($11.5\ \mu$). The two panels correspond to the detectors which comprise Band 4.

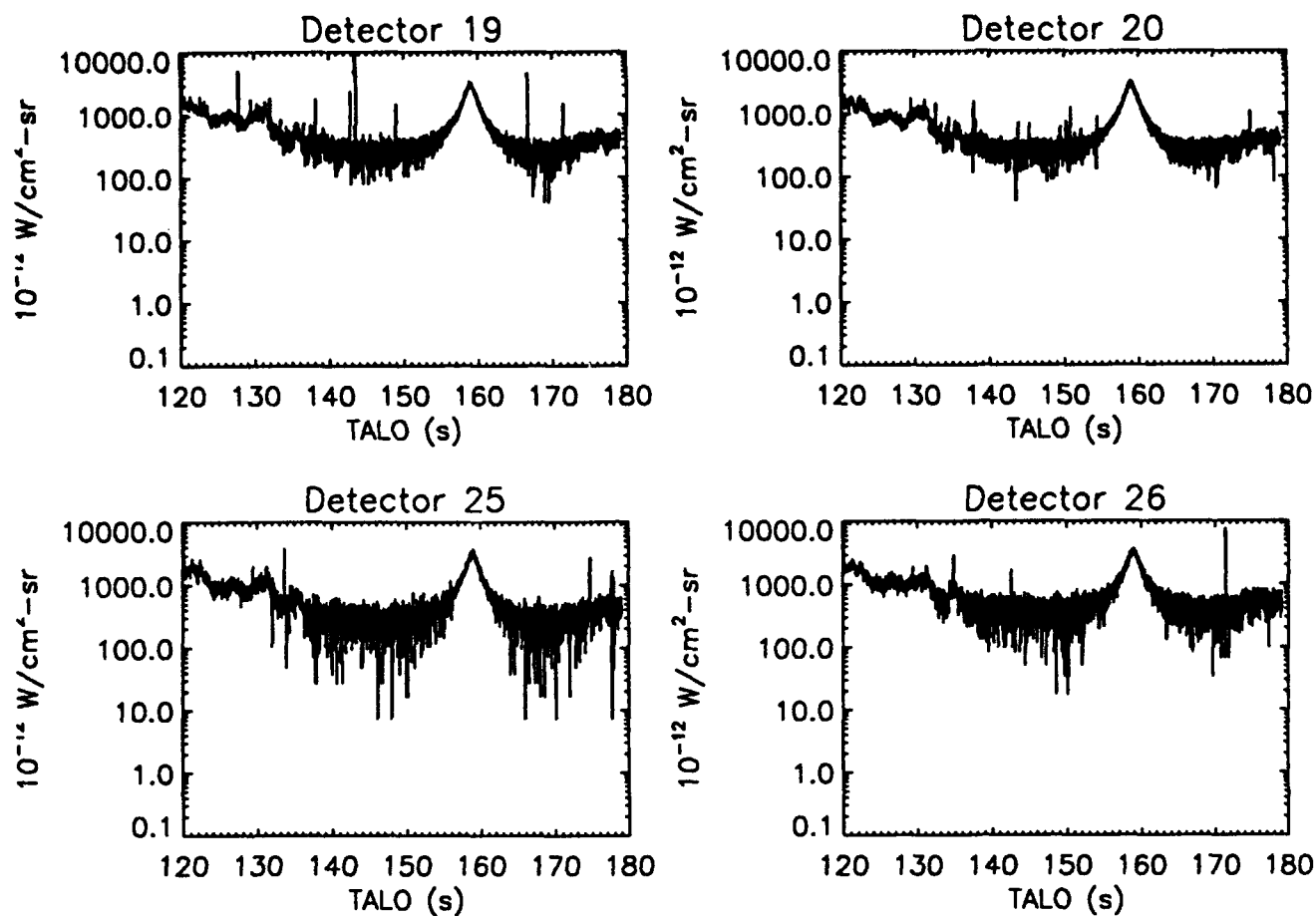


Figure 9: The unprocessed raw data for ELC Band 5 (12.0μ). The four panels correspond to the detectors which comprise Band 5.

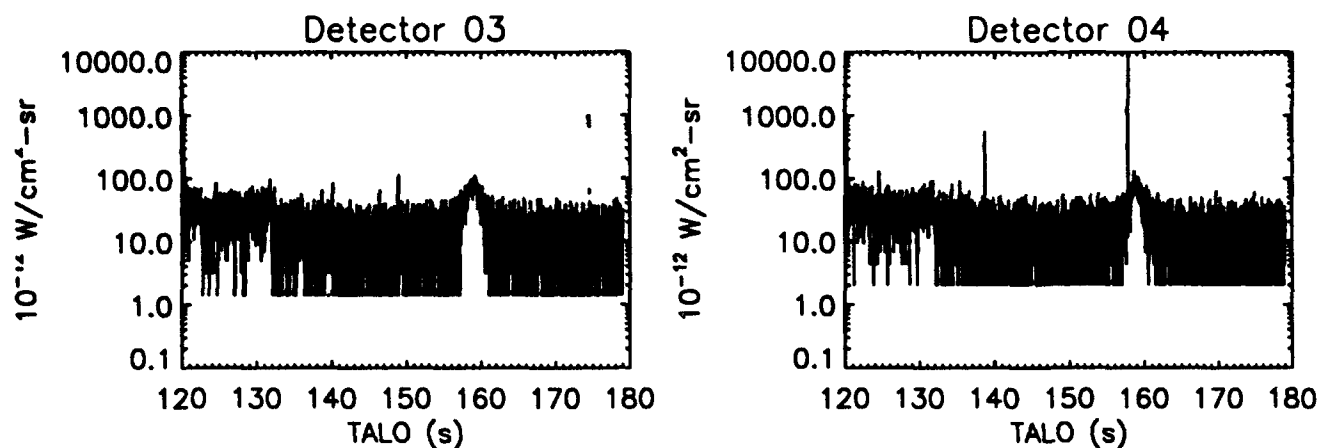


Figure 10: The unprocessed raw data for ELC Band 6 (12.5 μ). The two panels correspond to the detectors which comprise Band 6.

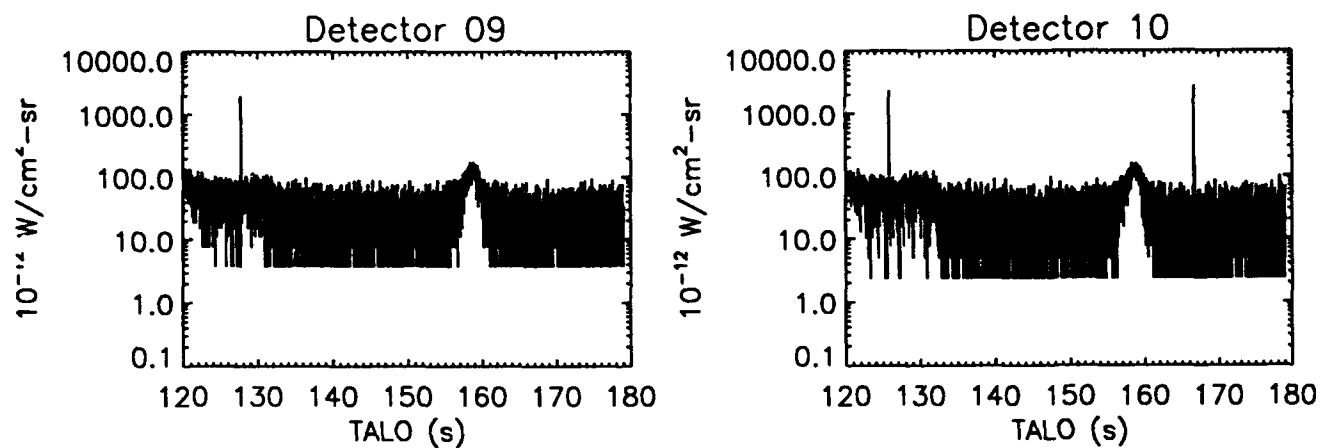


Figure 11: The unprocessed raw data for ELC Band 7 (13.7 μ). The two panels correspond to the detectors which comprise Band 7.

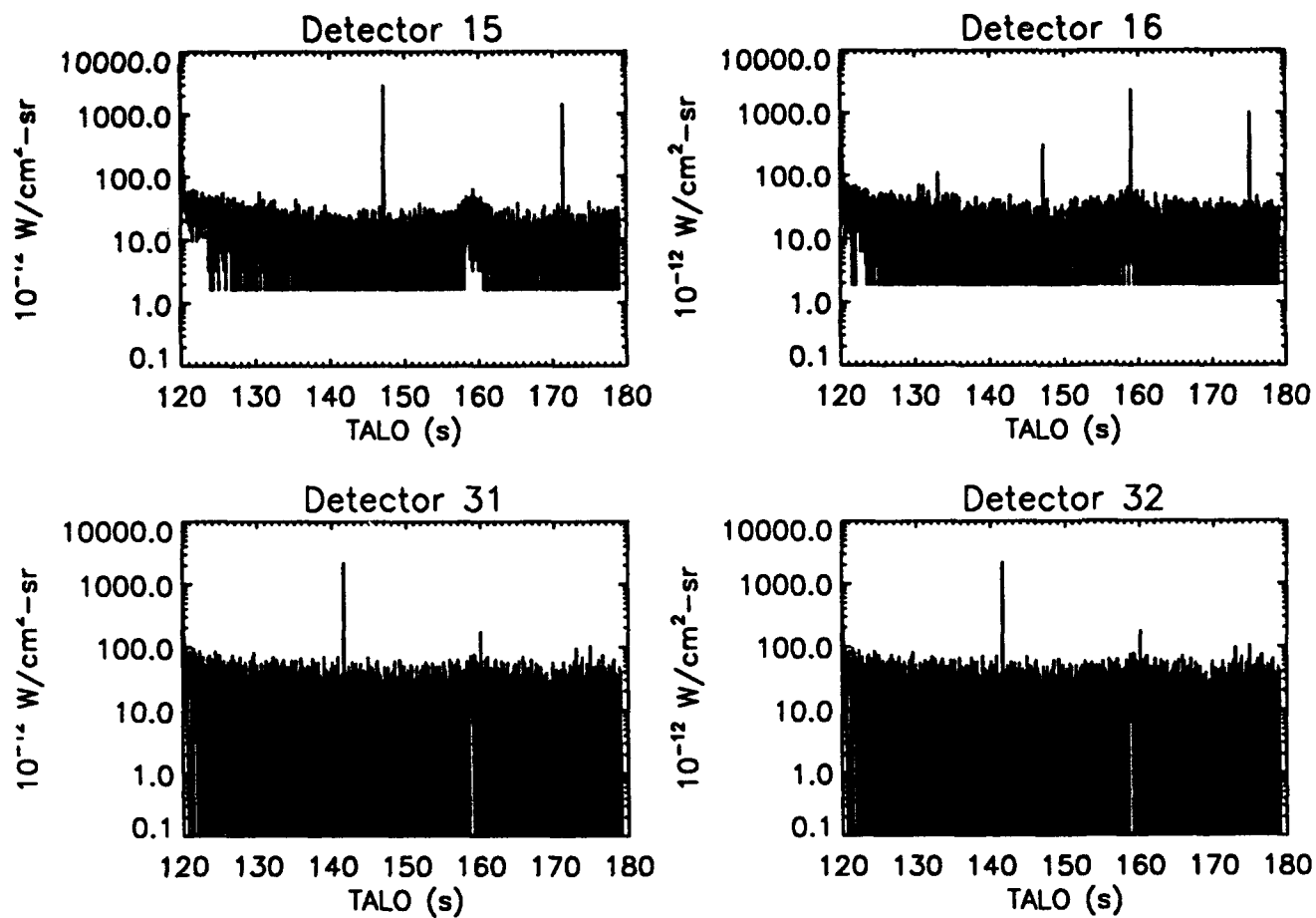


Figure 12: The unprocessed raw data for ELC Band 8 ($15.2\ \mu$). The four panels correspond to the detectors which comprise Band 8.

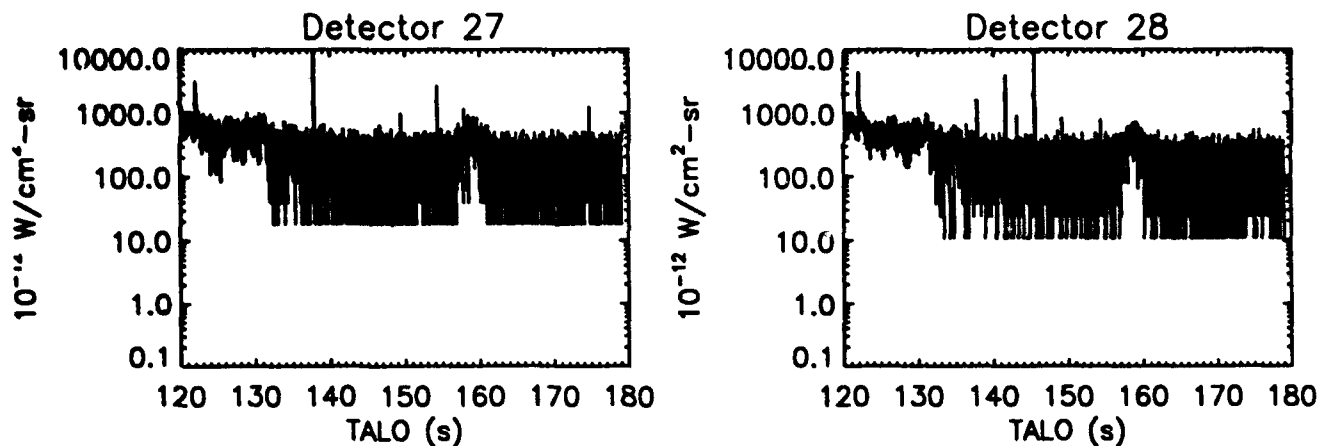


Figure 13: The unprocessed raw data for ELC Band 9 (26.3μ). The two panels correspond to the detectors which comprise Band 9.

2.2 SPIKE EXTRACTION

The ELC data as ingested contains numerous 'spikes' (primarily due to radiation 'hits') and 'drop-outs' (due to features of the electronics timing and the antenna pattern). Spikes typically manifest themselves by a several order of magnitude jump in signal for an extremely brief time, followed by a return to normal signal strengths. Drop-outs manifest themselves as places where the signal falls from normal signal strength down to zero momentarily and then returns to normal ranges. Depending on the source the spike could typically last from 1-5 samples (≤ 20 msec), although a "hard" radiation hit could perhaps drive a detector into saturation for as long as 20 samples.

A single algorithm was developed for extracting spikes and drop-outs from the data. Since both effects are typically characterized by extremely large short lived variations away from the typical signal, there were any number of approaches one might have tried in 'despiking' the data.

We had originally hoped that a simple Fourier filtering scheme might be used to extract spikes and dropouts from the ELC data, but we found that because of the degree of short timescale real variability present in the data, another method was needed. The approach we used begins with the initial data set, $\{r_0\}$, and creates two smoothed ancillary data sets, $\{a_1\}$ and $\{a_2\}$ by applying narrow (8 pt) and broad (32 pt) boxcar averages to the data. Averaging a spike over the much wider window in $\{a_2\}$ produces significantly less distortion in the boxcar average than is apparent in the narrow window

{a₁} case. Statistics were then obtained on the difference between these two averages, {d}. Spikes and drop-outs were then identified as extreme outlier points $\geq 5\sigma$ in {d}. The spike outlier regions are then excluded from the {a₂} data set to form a new data series {a*} containing gaps. Values in the original data set corresponding to values in the modified data set {a*} pass through the filtering process. Values in the original data set which are not contained in {a*} are replaced by interpolations of the {a₂} data across the gaps in {a*}. The results of this procedure are shown in Figures 14 to 22 for the 9 ELC bands.

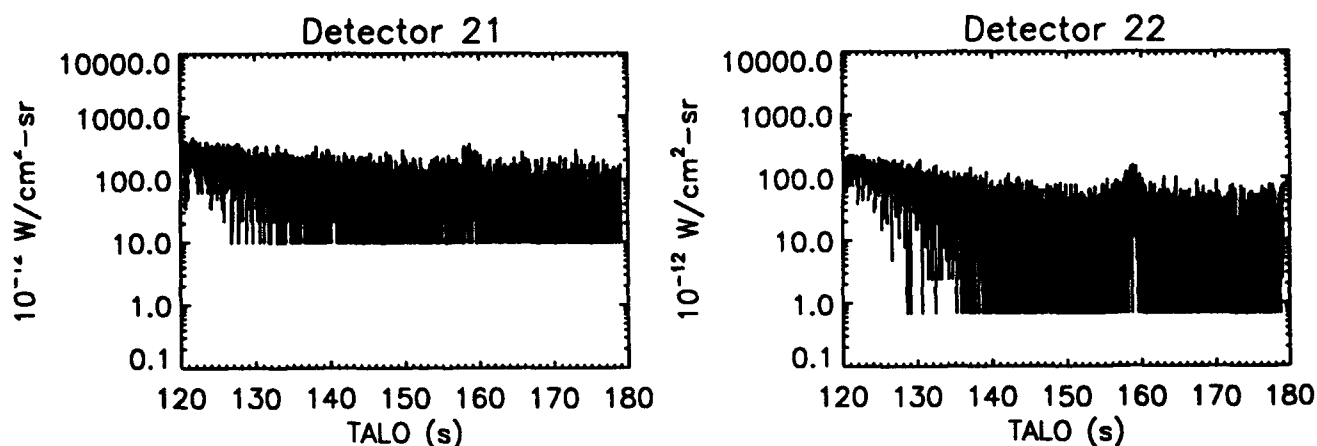


Figure 14: The data for ELC Band 1 after despiking. The two panels correspond to the detectors which comprise Band 1.

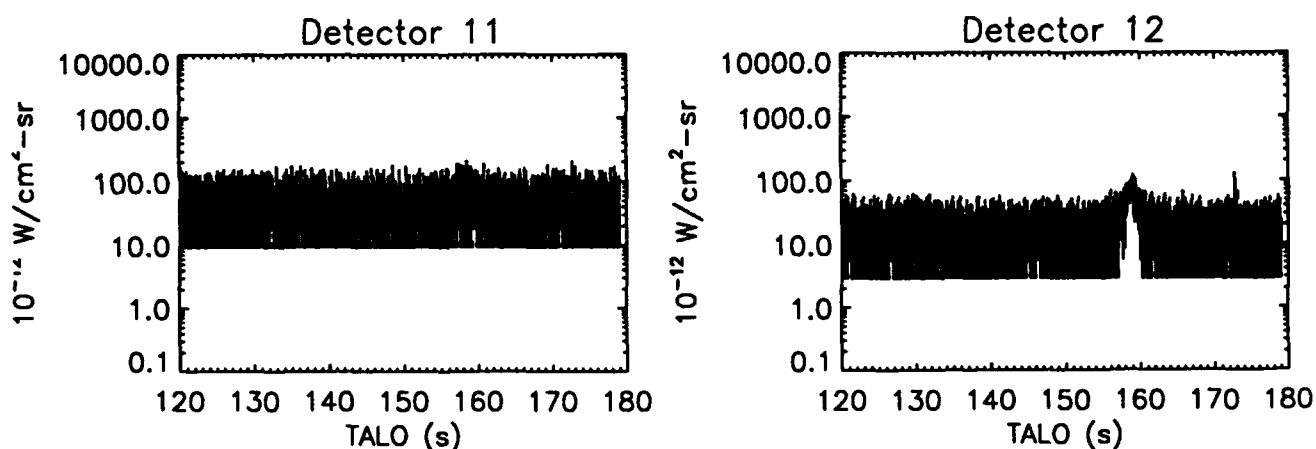


Figure 15: The data for ELC Band 2 after despiking. The two panels correspond to the detectors which comprise Band 2.

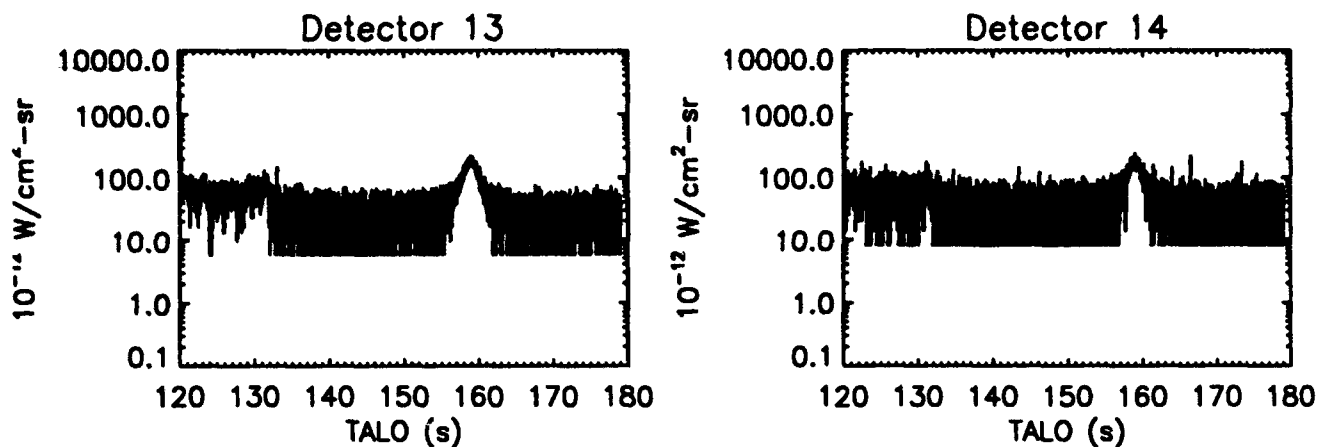


Figure 16: The data for ELC Band 3 after despiking. The two panels correspond to the detectors which comprise Band 3.

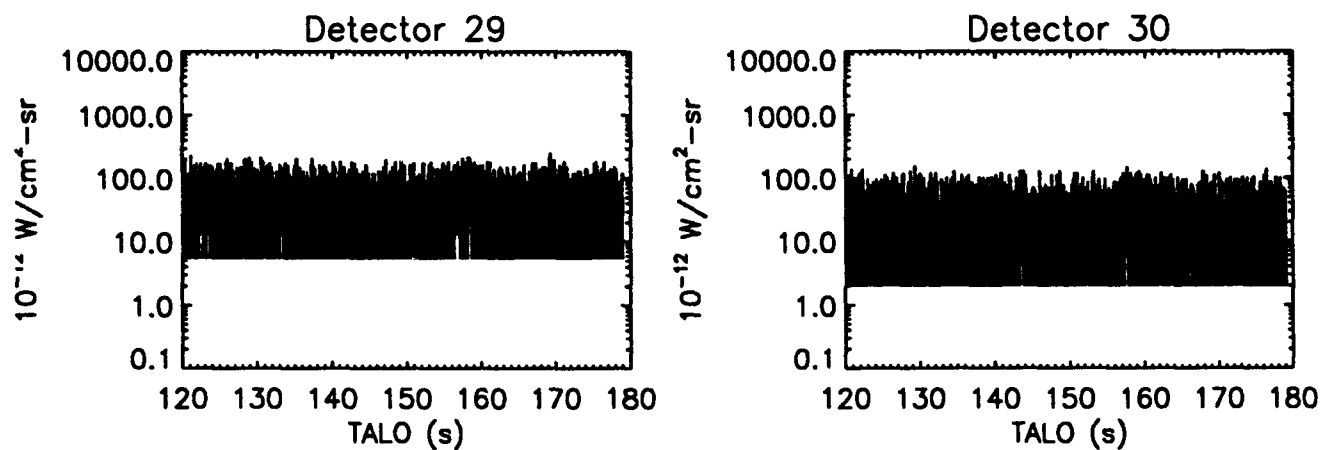


Figure 17: The data for ELC Band 4 after despiking. The two panels correspond to the detectors which comprise Band 4.

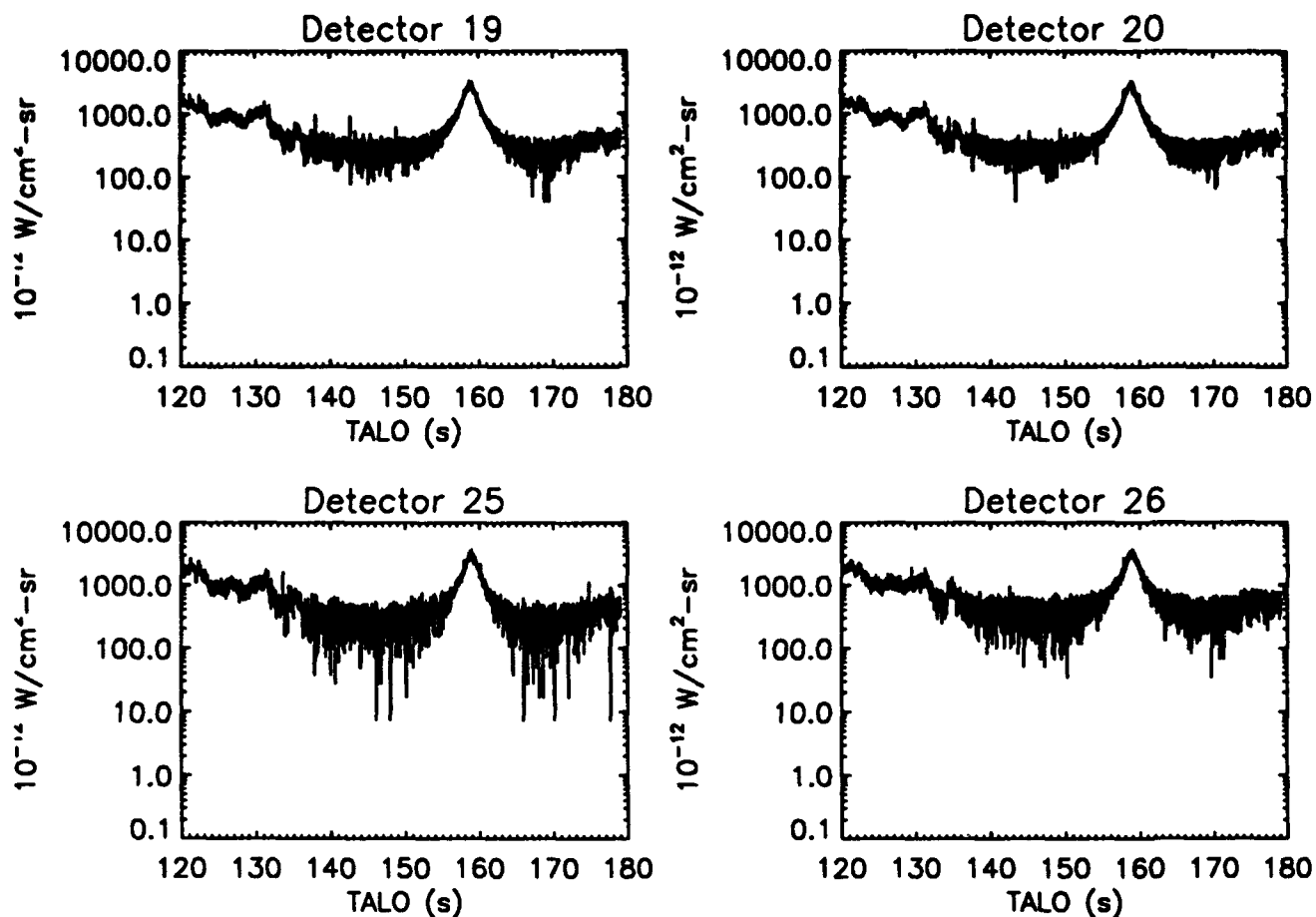


Figure 18: The data for ELC Band 5 after despiking. The four panels correspond to the detectors which comprise Band 5.

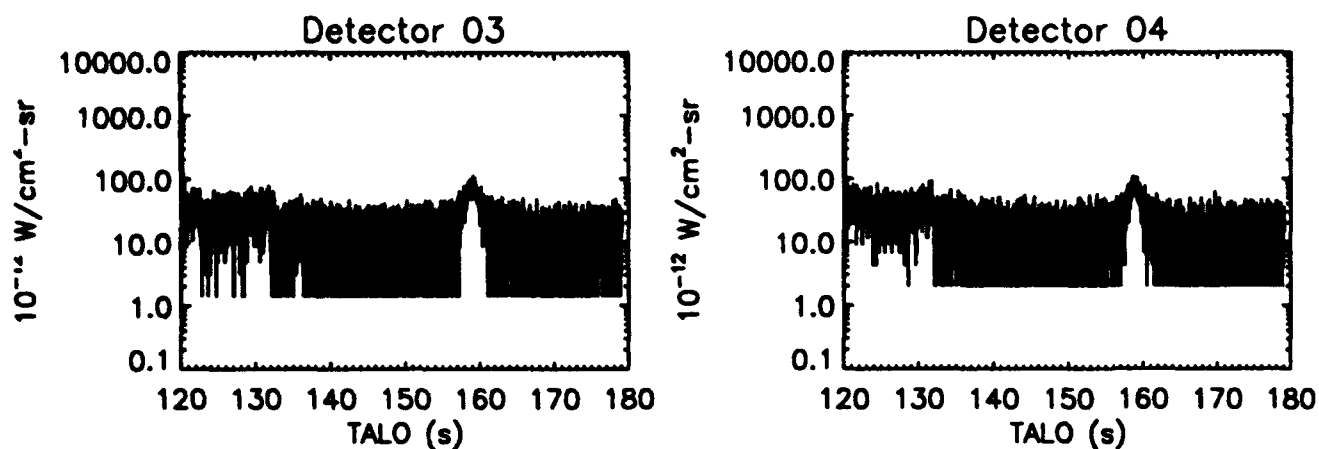


Figure 19: The data for ELC Band 6 after despiking. The two panels correspond to the detectors which comprise Band 6.

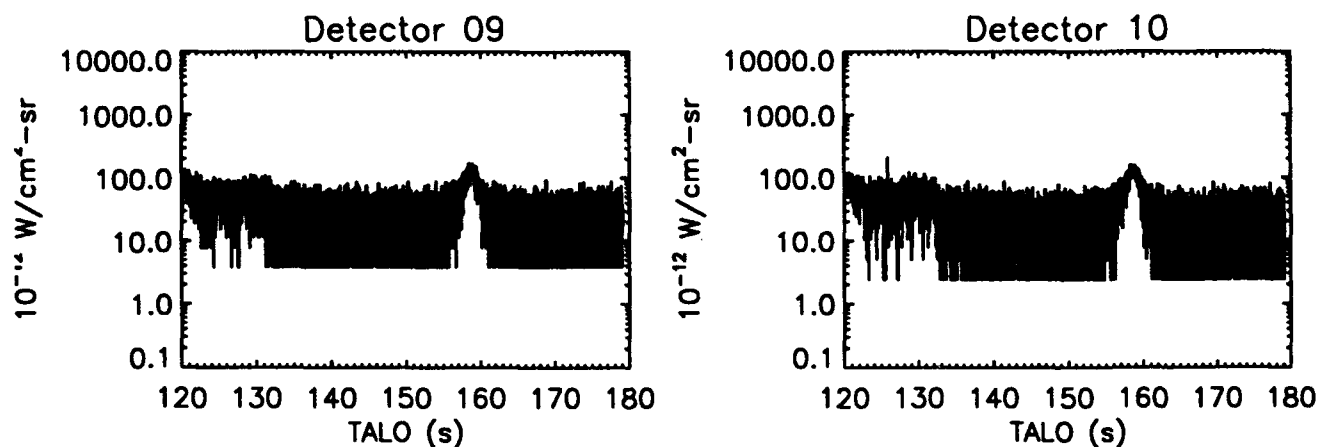


Figure 20: The data for ELC Band 7 after despiking. The two panels correspond to the detectors which comprise Band 7.

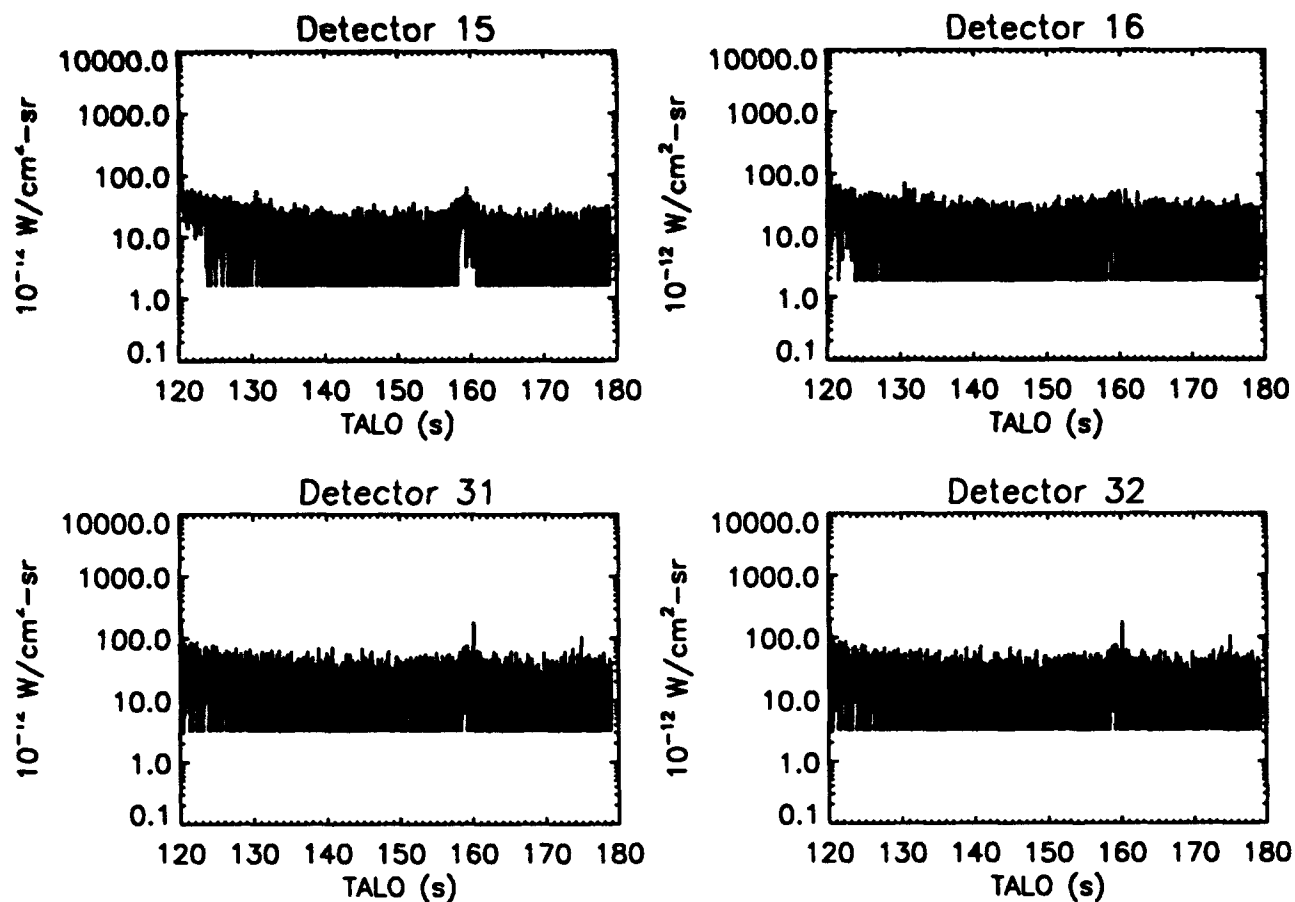


Figure 21: The data for ELC Band 8 after despiking. The four panels correspond to the detectors which comprise Band 8.

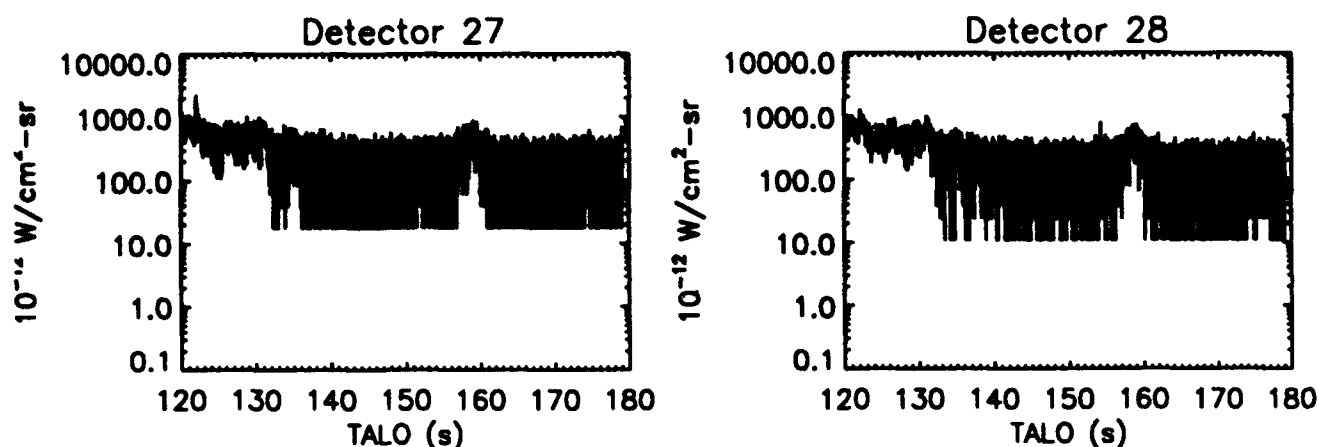


Figure 22: The data for ELC Band 9 after despiking. The two panels correspond to the detectors which comprise Band 9.

2.3 LOWPASS FILTER

ELC's detectors were designed for looking at the earthlimb. The zodiacal background signal is much fainter and so the zodiacal data obtained by ELC tend to be found at very modest signal-to-noise ratios. That is to say, the noise envelopes for most of the bands are large, and if sense is to be made of the signals, one must do a considerable amount of smoothing and averaging first.

The next stage in the signal processing was to pass the despiked data $\{r_1\}$, through a lowpass filter in order to produce data products that could more easily be used in analysis. The approach implemented in the present analysis uses a Lorentzian Butterworth filter⁽⁷⁾ to perform the lowpass filtering.

The lowpass filtered time ordered data set r_2 was created from the despiked data r_1 as follows.

$$r_2(t) = R_1(\omega) * f(\omega) \quad (1)$$

where $R_1(\omega)$ is the Fourier transform of r_1 ,

$$R_1(\omega) = \frac{1}{\sqrt{2\pi}} \int r_1(t) e^{i\omega t} dt$$

and $f(\omega)$ is the Butterworth lowpass filter centered at ω_c

$$f(\omega) = \frac{1}{1 + \left(\frac{\omega - \omega_c}{\gamma} \right)^2}$$

The parameter γ controls the severity with which the filter smooths the data. The filtered data sets for the 9 ELC bands are shown in Figures 23 to 31.

At Dr. Price's suggestion and to study outlier effects, we will also investigate the use of a parabolic filter as well⁽⁷⁾,

$$f(\omega) = [-\alpha(\omega - \omega_c)^2 + \beta] \theta(\beta - \alpha(\omega - \omega_c)^2) \quad (2)$$

which, unlike the Lorentzian Butterworth filter, has an absolute high-frequency cutoff, and a different weighting near ω_c .

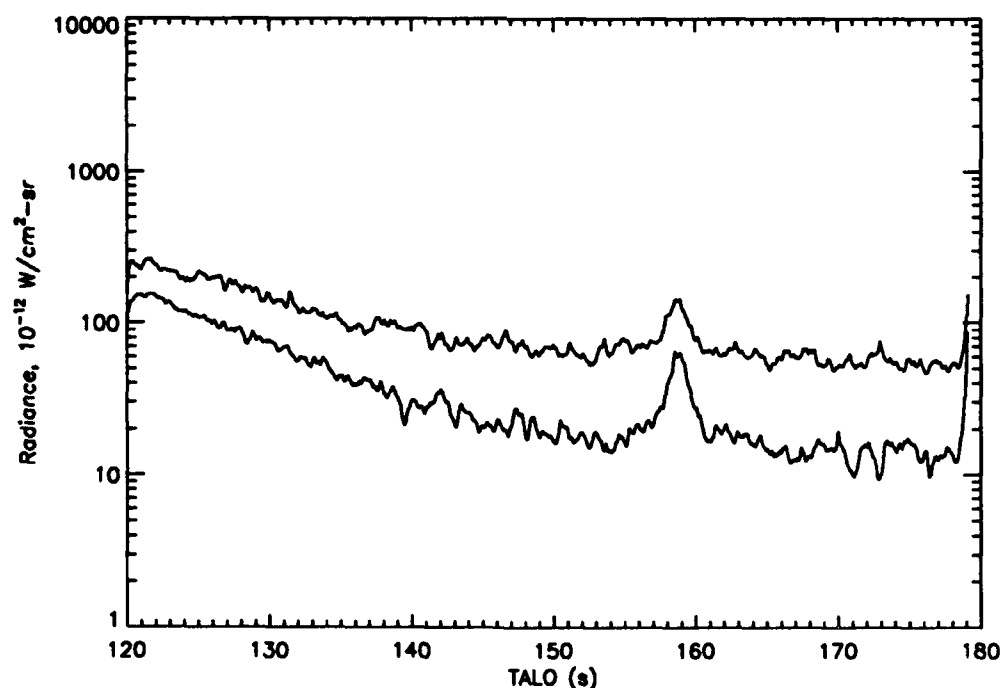


Figure 23: Composite of the lowpass filtered data for the two detectors making up ELC Band 1.

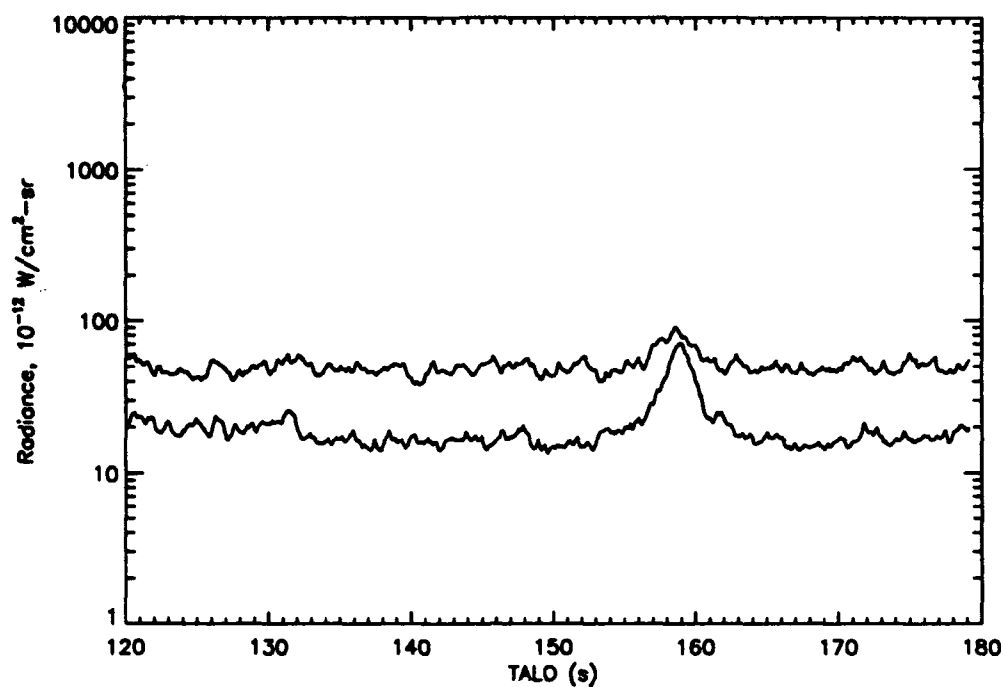


Figure 24: Composite of the lowpass filtered data for the two detectors making up ELC Band 2.

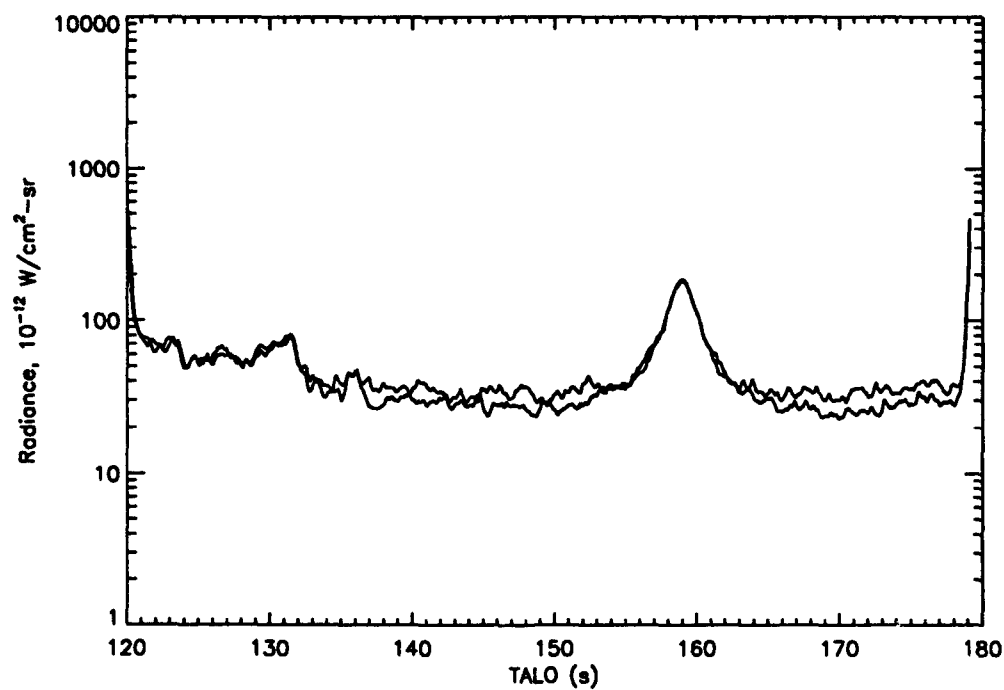


Figure 25: Composite of the lowpass filtered data for the two detectors making up ELC Band 3.

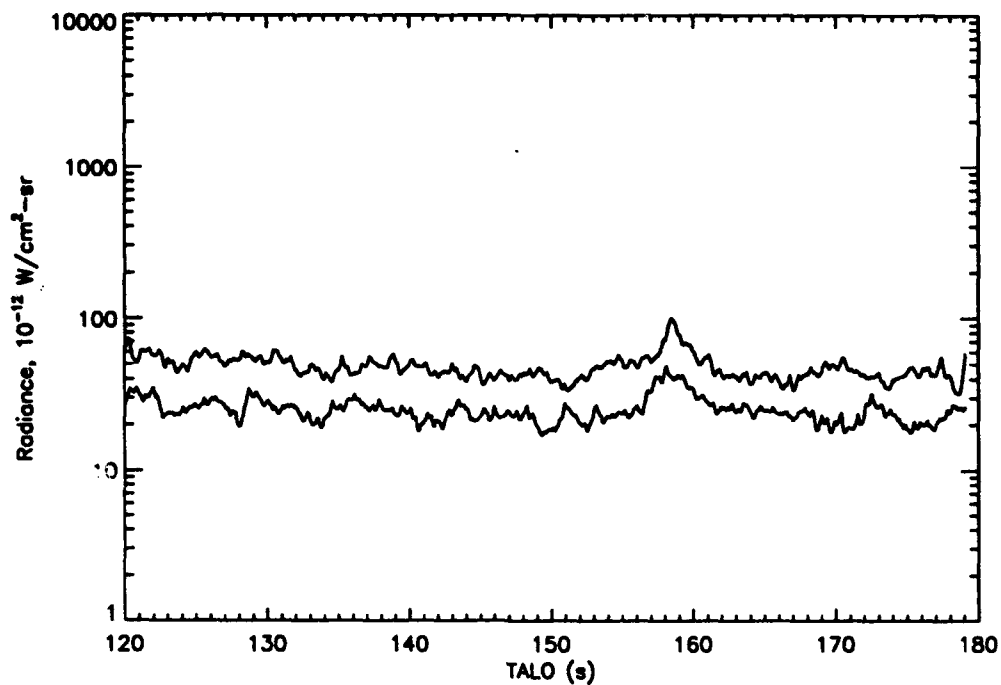


Figure 26: Composite of the lowpass filtered data for the two detectors making up ELC Band 4.

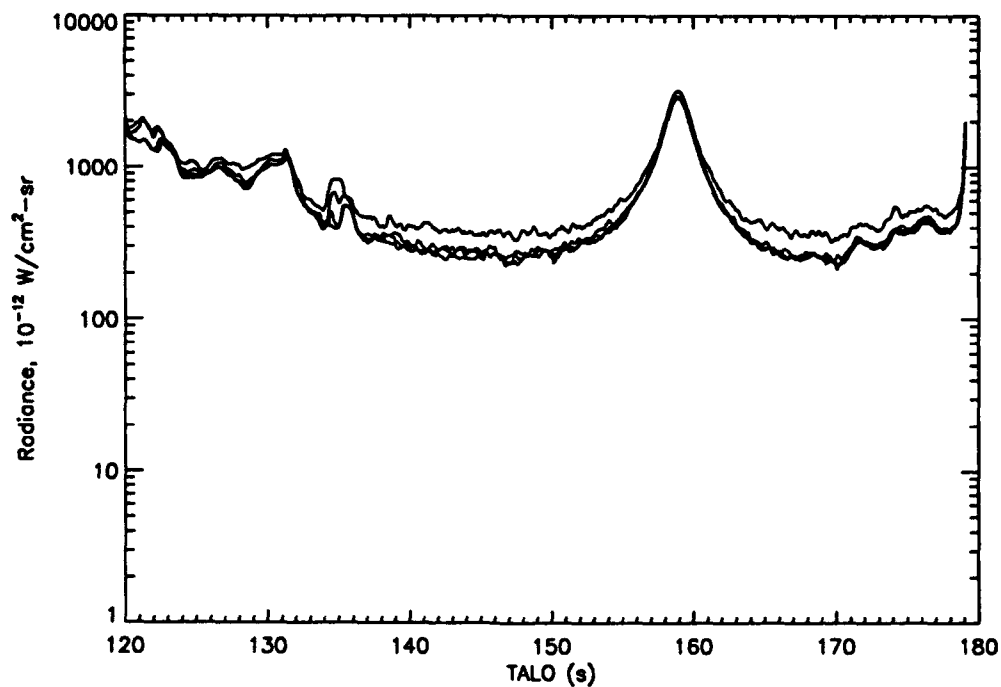


Figure 27: Composite of the lowpass filtered data for the four detectors making up ELC Band 5.

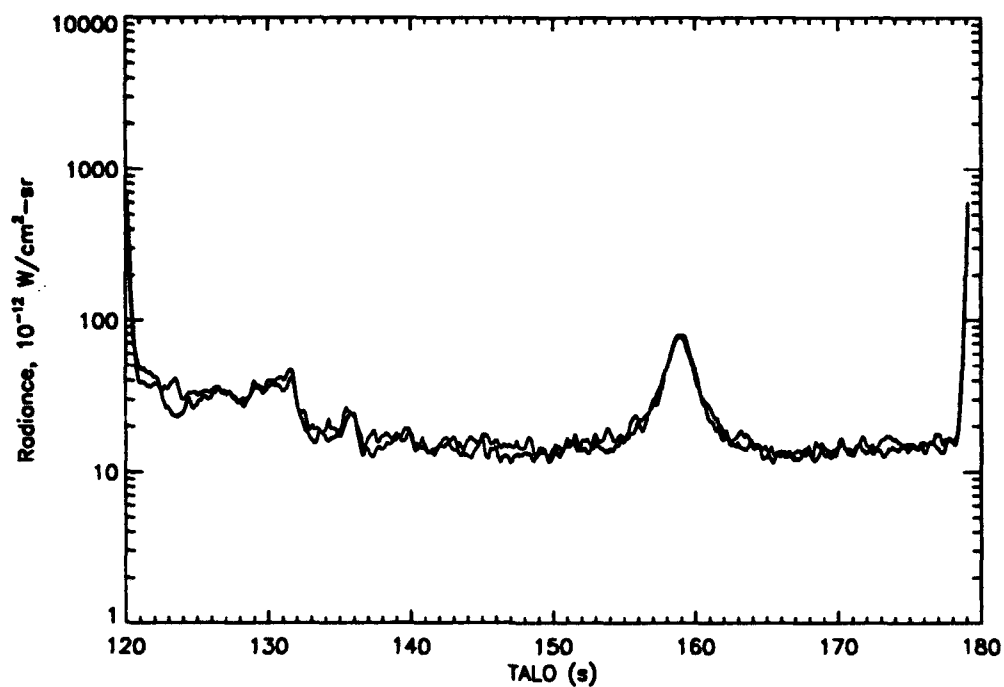


Figure 28: Composite of the lowpass filtered data for the two detectors making up ELC Band 6.

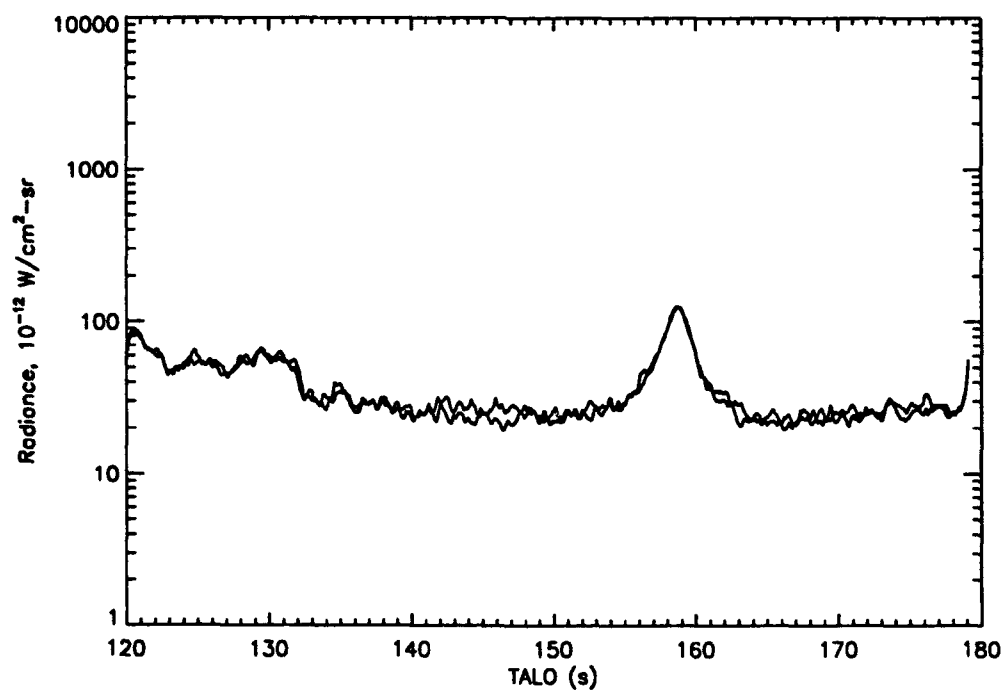


Figure 29: Composite of the lowpass filtered data for the two detectors making up ELC Band 7.

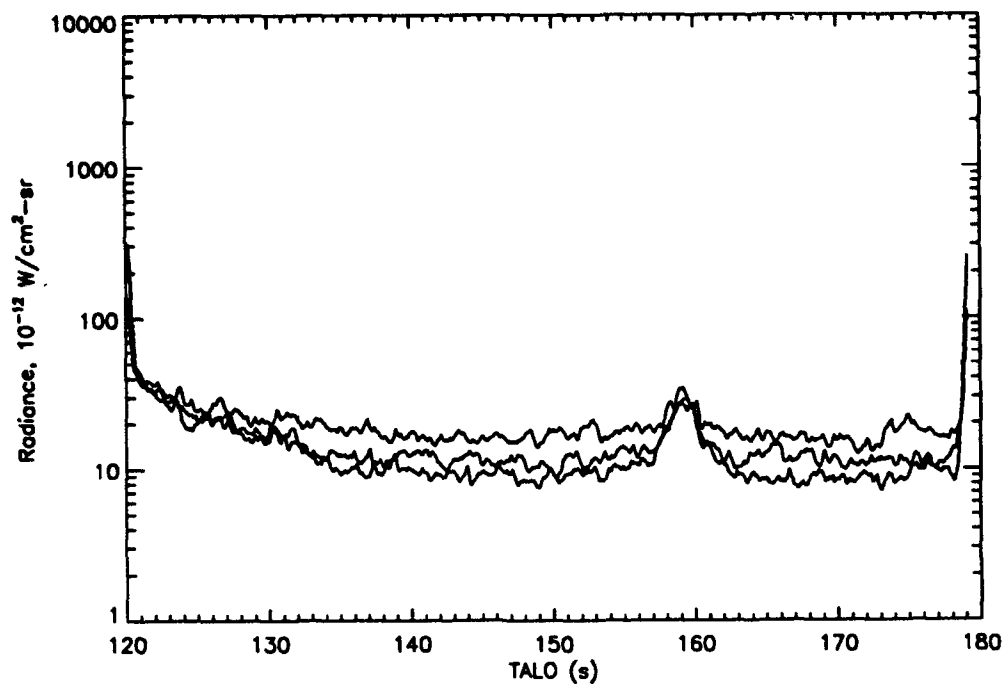


Figure 30: Composite of the lowpass filtered data for the four detectors making up ELC Band 8.

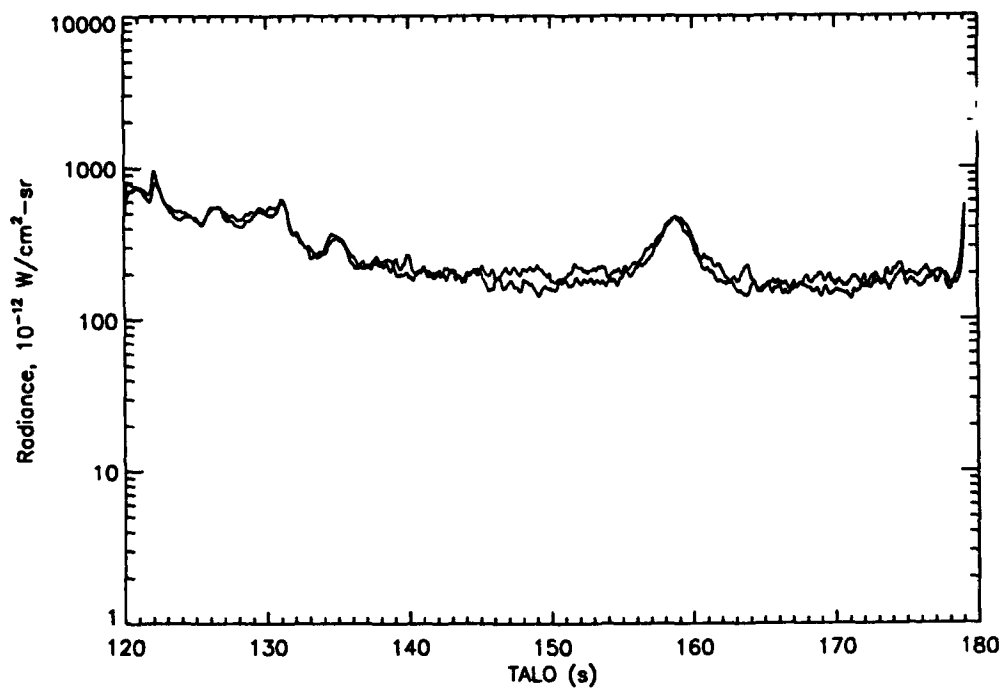


Figure 31: Composite of the lowpass filtered data for the two detectors making up ELC Band 9.

2.4 COADDITION

All nine of the ELC bands had at least two detectors worth of data, and two of the bands in fact had data in four detectors. Based on the detector signatures near the zodiacal peak, there were no systematic gain or offset problems with bands 3, 6, 7, 8, or 9, and the detectors in those bands were simply averaged in a trivial fashion: for 2 detector channels, $b = (b_1 + b_2)/2$; and for 4 detector channels, $b = (b_1 + b_2 + b_3 + b_4)/4$.

Bands 1, 2, and 4 had 2 detectors each, and showed significant gain differences between channels. Since there were only two detectors per channel there was no *a priori* means of identifying which (if indeed either) of the detectors was producing the proper signal and which was returning a somewhat aberrant signal. Since in any event the coadded band was ultimately to be normalized against IRAS data, the approach adopted was to arbitrarily adjust the gain and offset of the lesser of the two signals until it matched the higher signal at the zodiacal plane crossing and at the southern ecliptic pole. Because of the poor signal-to-noise problems at this zodiacal pole, it was actually the average signals over a window extending from -75° to -80° in both the ELC and IRAS data that were used in fitting the pole averages. Because the zodiacal background changes relatively linearly in this window, and only slowly near the ecliptic poles, averaging over the 5° window does not bias the data. The resulting signals were then coadded in the same way that band 3, 6, 7, and 9 were.

Band 5 had 4 detectors, 3 of which were in close agreement, and a fourth which was aberrant. As was seen in Figure 27, the fourth detector, (detector 26) agreed well with detectors 19, 20, and 25 at high signal strengths, but showed noise floor radiances typically 50% higher at low signal strengths. A gain correction was applied to detector 26 so that its pole and plane radiances both agreed (in the window-average sense mentioned above) with the other detectors. The detectors were then coadded in the same manner as band 8 above to produce the coadded band 5 results. The coadded data for each of the ELC bands are plotted in Figures 32 to 40.

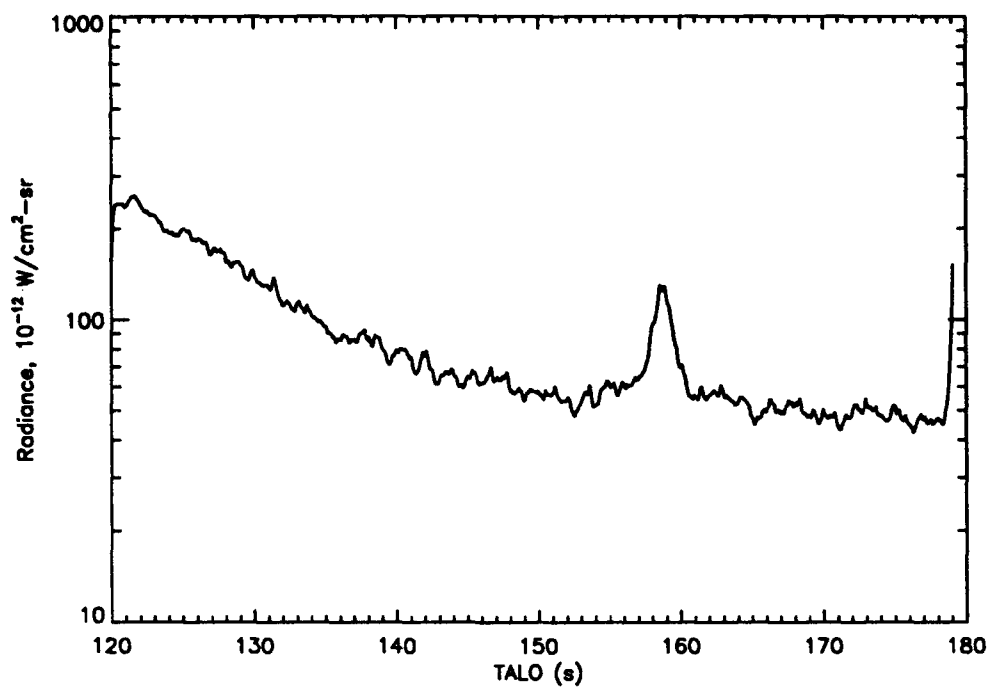


Figure 32: Coadded data for ELC Band 1.

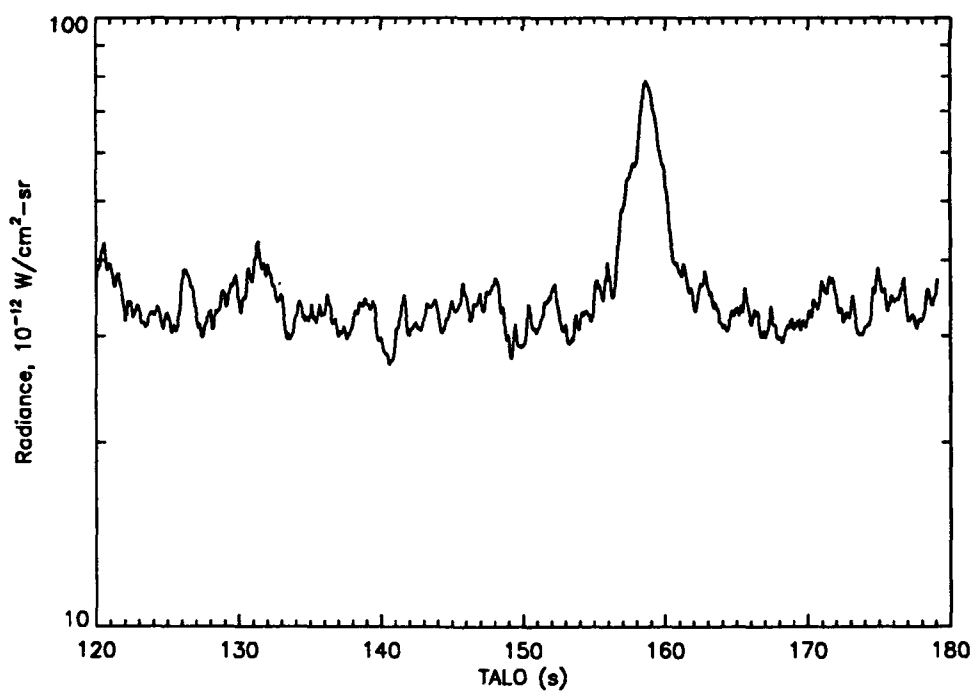


Figure 33: Coadded data for ELC Band 2.

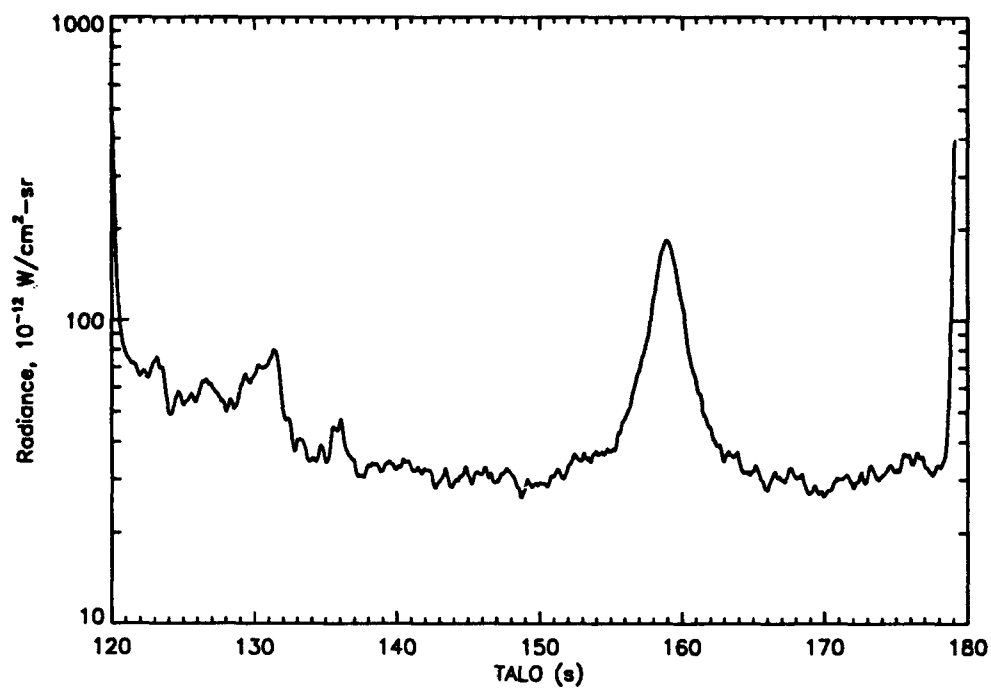


Figure 34: Coadded data for ELC Band 3.

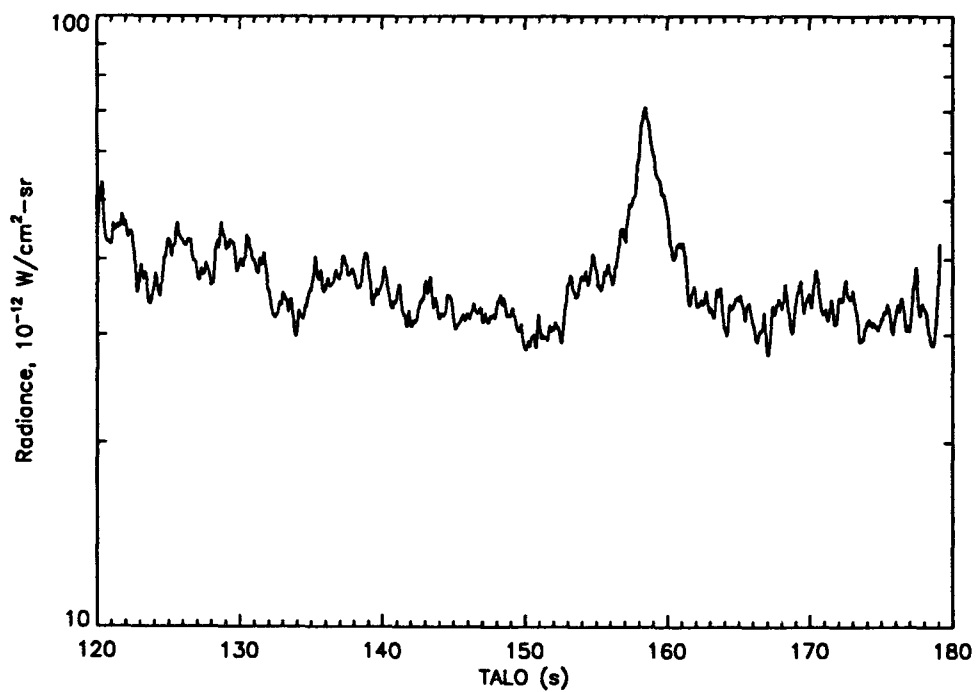


Figure 35: Coadded data for ELC Band 4.

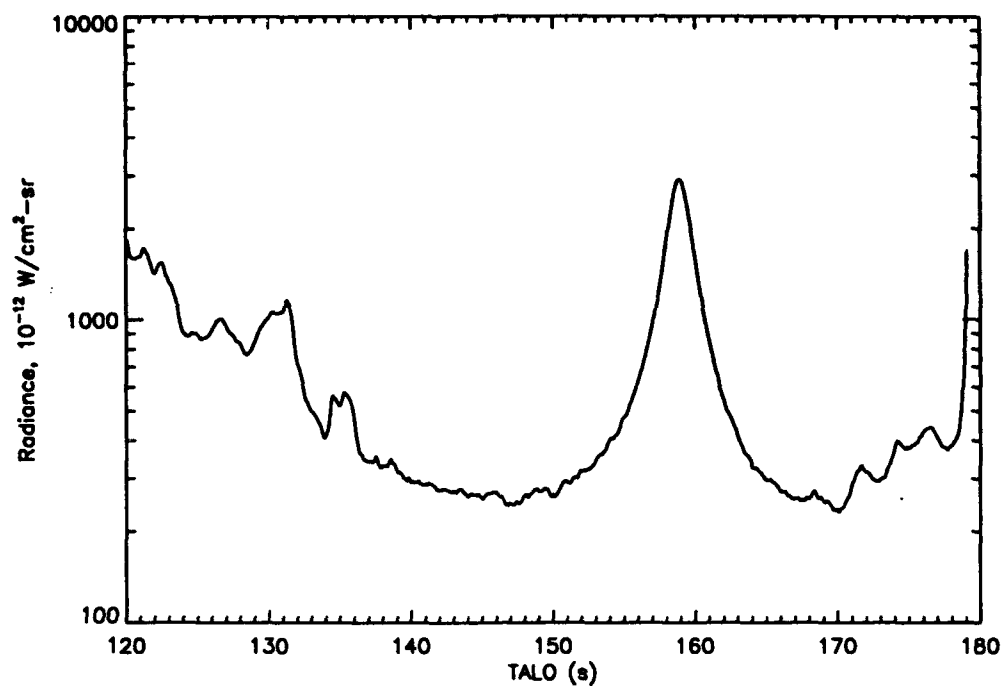


Figure 36: Coadded data for ELC Band 5.

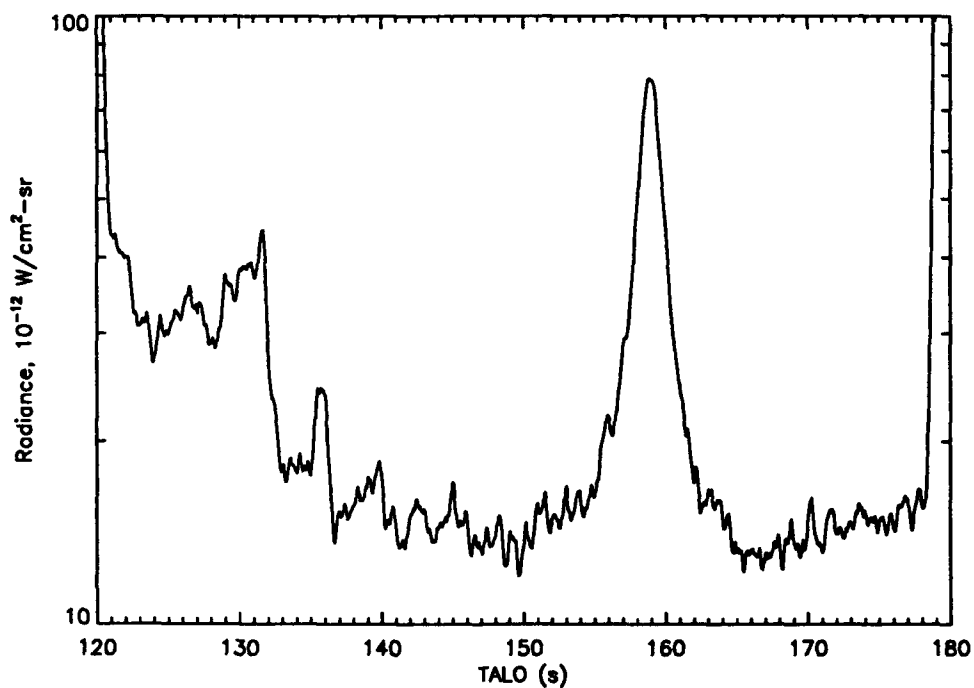


Figure 37: Coadded data for ELC Band 6.

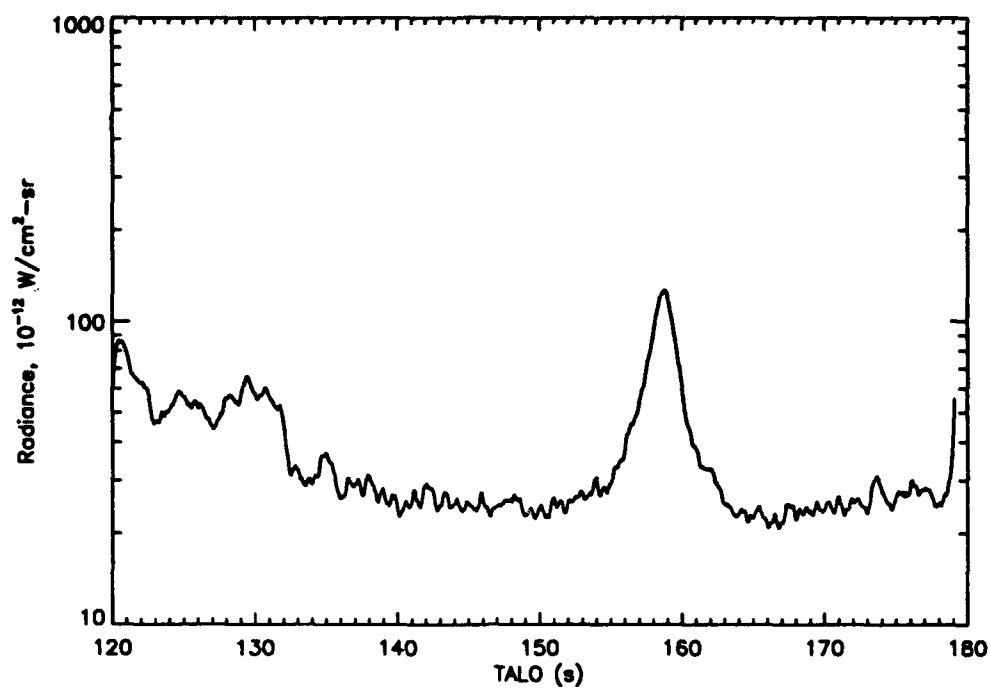


Figure 38: Coadded data for ELC Band 7.

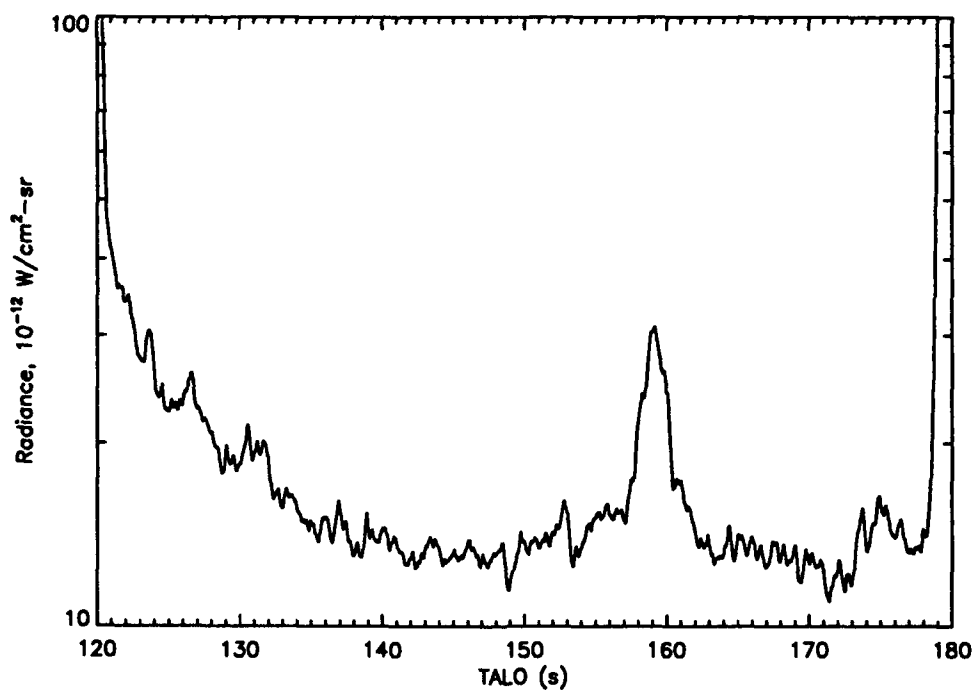


Figure 39: Coadded data for ELC Band 8.

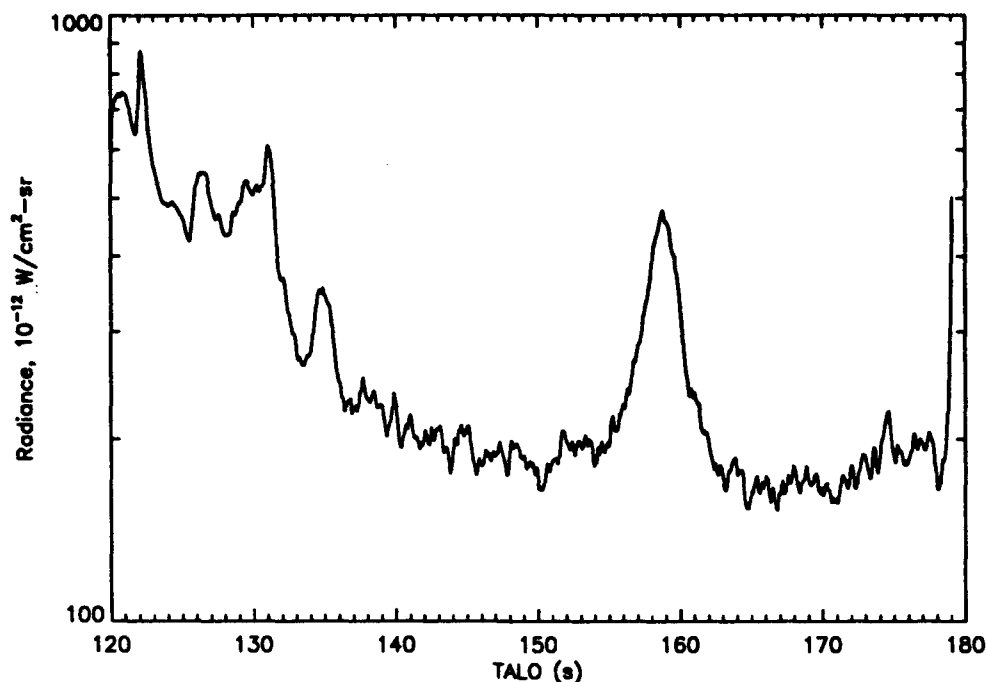


Figure 40: Coadded data for ELC Band 9.

2.5 ATMOSPHERE CORRECTIONS

During the ELC Long-Roll the sensor scanned through 430° in the local tangent plane and rose in altitude from 150 to 230 km. Since the scan geometry was so simple, it was possible to use the Night-Time-Quiescent-Half-Limb FAUST model directly.

Predicted atmospheric radiance values for each of the 9 ELC bands were tabulated at 5 km altitude intervals over the altitude range, and then an exponential atmosphere model was fit to the tabulated data. We experimented with power law fits to the atmospheric model as well, but under advice of Dr. Price, generally abandoned that approach in favor of the exponential model. The resulting models were then used to produce simple functions describing atmospheric radiance as a function of time of flight.

Since most of the ELC bands were narrow ($\leq 1 \mu\text{m}$), and since there were some inherent difficulties with the user interface in FAUST which limited the accuracy with which one could define the edges of spectral bands, we treated the absolute normalization of the atmospheric model as a free parameter -- to be fitted to the actual ELC data. This 'ELC knows best' approach significantly reduced systematic errors induced by the imprecision with which the band edges were defined in FAUST.

We found that bands 2 and 4 had no atmospheric contributions in the sense that there was no systematic tendency for the background amplitude to decay with time over the course of the long rolls. Bands 1, 3, 5, 6, 7, and 8 all had atmospheric contributions, but the FAUST-based models seemed to adequately account for the shape of the decay curves. ELC band 9 (26.2 μm) however, was anomalous. The atmospheric background predicted by FAUST for band 9 does not resemble the temporal behavior for the background seen in the ELC data for band 9. After some experimentation it was found that a $t^{-1/2}$ power law model fit the data nicely. In the subsequent analysis we have carried along two versions of band 9: Band 9A which uses the FAUST based atmosphere model for consistency with the other bands, and band 9B which uses the power law 'ELC knows best' atmosphere model. The two versions of band 9 differ dramatically when they are renormalized against IRAS because the different models lead to radically different backgrounds near the Zodiacal Poles. The FAUST-derived exponential atmospheric profiles are shown in Figure 41.

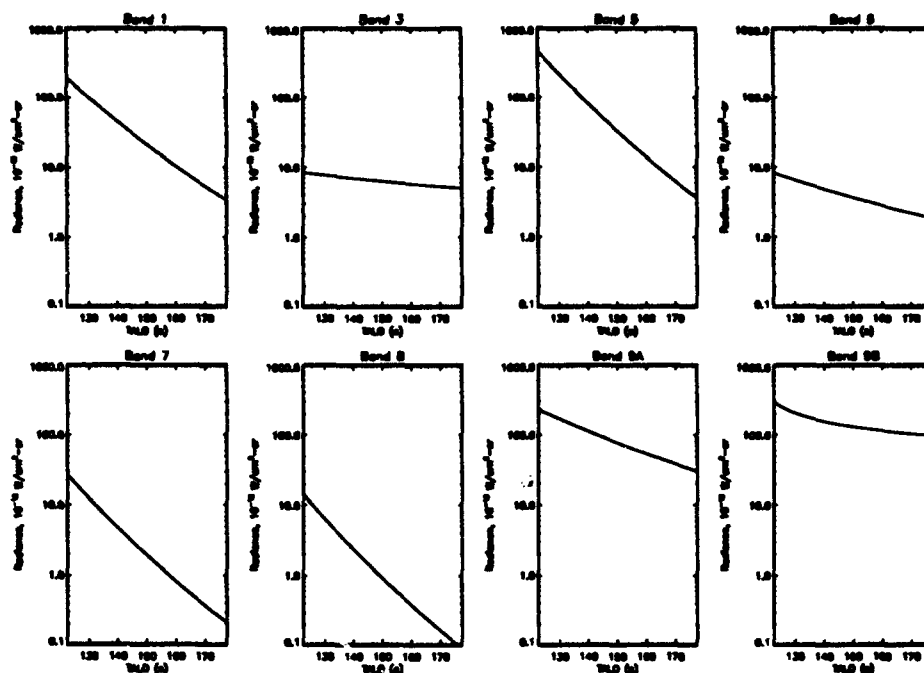


Figure 41: Plots showing the model atmospheric radiance curves derived from FAUST and used in making the atmospheric corrections.

One possible explanation for the apparent discrepancy between the FAUST model and the ELC measurements would be the presence of some form of outgassing contamination: that is, what we are calling an atmospheric signal in the present context, might in fact be a juxtaposition of an atmospheric signal and a decaying outgassing signal. We note that band 9 is broad ($5.63\text{ }\mu\text{m}$) and is located well out into the water continuum. Since it is quite plausible for water vapor outgassing to have occurred at this early time in the mission, we will be studying this matter in great detail as we investigate outgassing effects in ZIP.

2.6 RENORMALIZATION

The basic approach used in making the radiometric recalibration of ELC was to find (nearly) simultaneous observations of the same region of sky by ELC and IRAS at 12 and 25 microns, and then use those observations to renormalize the ELC data to the IRAS data in those bands. Then, using waveband scaling arguments, we extended these calibrated observations to the other ELC bands.

One might consider using galactic plane crossings as a convenient way to peg the ELC and IRAS calibrations. Unfortunately none of the ELC galactic plane crossings happens in favorable conditions. The first and third galactic crossings happen at about 122 s and 179 s after launch. The first when the sensor is still deep in the atmosphere, and the third just as the spacecraft performs the yaw correction to terminate the roll scan and begin ELCs first dip into the earthlimb. The second crossing (which occurs at ~149 s after launch) would have been ideal except for the fact that the crossing occurred at a large galactic longitude and by chance, crossed a particularly dim place on the galactic plane. Even in the 12μ band, which had by far the best signal-to-noise ratio of any of the ELC bands, the crossing is not observable.

Since the galactic plane crossings seem unusable for calibration purposes, we have concentrated our efforts on the ecliptic pole regions instead. The ELC data and the IRAS 2' Zodiacal History File (ZOHF) (Standard Observing Period (SOP) 547) both contain observations near the North Ecliptic Pole (NEP) and South Ecliptic Pole (SEP). The first question was then whether each of these potential cross-tie regions could be used.

The NEP data from ELC (at 172.77 s after launch) is virtually simultaneous with the IRAS NEP observations (roughly 2 minutes earlier) but although both sensors were observing at $+80^\circ$ Ecliptic latitude they differ significantly in longitude, and as ELC is approaching the end of the long roll and the galactic plane, there is a marked deviation from the background zodiacal signature. The ELC data for the SEP are spatially coincident with the IRAS SEP data, but there are, depending on the particular scan, as many as 8 hours separating the ELC and IRAS observations.

Figure 42 shows a superposition of 4 IRAS plane-pole-plane scans contained in SOP 547 of the IRAS 2' ZOHF. The data show that for the 16 hour period surrounding the ELC flight the zodiacal background was quite stable; the four zodiacal scans in this time period are virtually identical. This stability allows us to confidently use the data from the IRAS south ecliptic pole region observations in calibrating ELC even though the observations were made at different times on the day of the ELC flight.

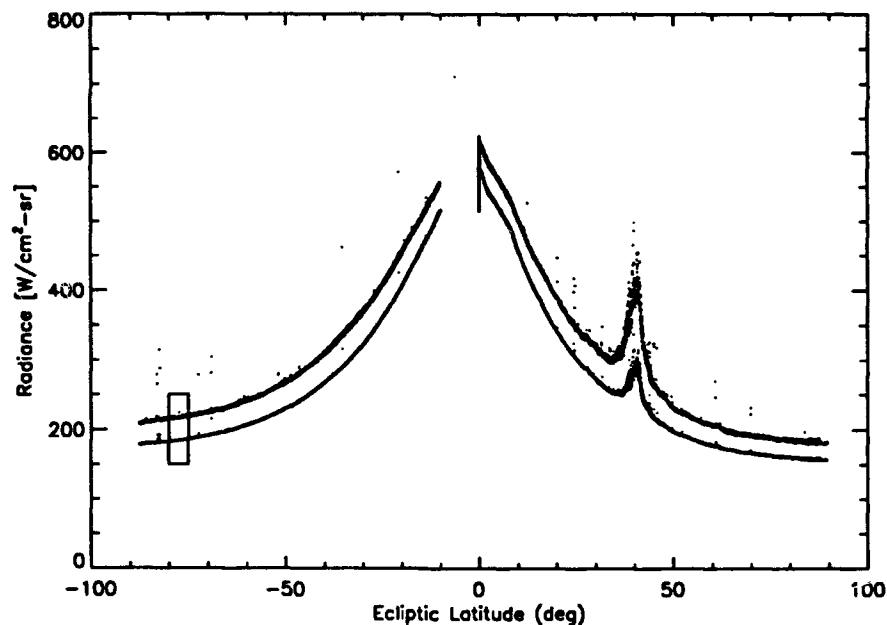


Figure 42: IRAS data for the date of the ELC flight. Each curve is a superposition of 4 separate sweeps made by IRAS. The upper curve corresponds to IRAS Band 1 ($12\ \mu$), while the lower curve represents IRAS Band 2 ($25\ \mu$) data.

2.6.1 Color Corrections

The 12 micron ELC band 5 and IRAS band 1 are quite similar -- they have the same band center, and nearly identical bandwidths. But IRAS' band 2 (25 microns) is 3 times broader than corresponding ELC band 9 (centered at 26 microns). The implied color corrections are derived using:

$$C_{ELC}^{IRAS}(T) = \frac{\int_0^\infty B(\lambda, T) R_{IRAS}(\lambda) d\lambda}{\int_0^\infty B(\lambda, T) R_{ELC}(\lambda) d\lambda} \quad (3)$$

Here the R 's are the spectral responsivities of the respective sensors for the wavebands in question, and T is the temperature of the source being observed. For Zodiacal dust observed near the ecliptic poles (and hence near the earth) one expects $T \sim 280 \pm 20$ K. The $T=280$ K color corrections for all of the ELC bands are summarized in Table 2. The $T=280$ K color correction for the 12 micron band is small, but the correction for the 25 micron band is large.

Table 2: ELC Color Corrections @ $T=280$ K

Band	λ_{eff}	$\delta\lambda_{eff}$	C_{ELC}^{IRAS}	Corrected Against
ELC-1	5.6	.92	$.119 \pm .052$	IRAS-1
ELC-2	9.6	.71	$.134 \pm .013$	IRAS-1
ELC-3	10.6	1.13	$.200 \pm .007$	IRAS-1
ELC-4	11.5	.99	$.160 \pm .001$	IRAS-1
ELC-5	12.0	7.01	$.943 \pm .002$	IRAS-1
ELC-6	12.5	.95	$.135 \pm .003$	IRAS-1
ELC-7	13.7	1.38	$.165 \pm .007$	IRAS-1
ELC-8	15.2	.73	$.074 \pm .030$	IRAS-1
ELC-9	26.2	5.63	$.270 \pm .005$	IRAS-2

ELC bands 2, 3, 4, 6, 7, and 8 are located in the spectral region covered by IRAS band 1 and can plausibly be calibrated against IRAS band 1 just as ELC band 5 was. ELC band 1 however, is another matter. ELC band 1 is a narrow band that does not

overlap IRAS band 1 at all and lies in a spectral region which is expected to have strong atmospheric contributions from NO. When data from COBE become available, it should be possible (using a model for the zodiacal pole brightness) to calibrate ELC band 1 directly against COBE/Diffuse Infrared Background Experiment (DIRBE) band 4. Until then we will use the same technique as we used on bands 2-8, with the caveat that the band 1 results are preliminary.

These color corrections were then used in converting IRAS measurements into predicted ELC values for the SEP. The differences between the predicted ELC inband radiances in the 12 and 25 micron bands and the observed ELC values were used to derive renormalization constants. Table 3 summarizes the predicted ELC radiance values (based on the IRAS data), the observed ELC radiance values, and the calibration renormalization factors at the calibration cross-tie point.

Table 3: ELC-IRAS Comparison

Band	Wavelength μm	IRAS-Predicted ELC Radiance $10^{-12} \text{ W/cm}^2\text{-sr}$	Observed ELC Radiance $10^{-12} \text{ W/cm}^2\text{-sr}$	Renormalization Factor
1	5.6	25.9	22.9	1.13
2	9.6	28.8	15.2	1.90
3	10.6	43.0	22.5	1.91
4	11.5	34.4	11.3	3.04
5	12.0	203.0	223.0	0.91
6	12.5	29.0	8.24	3.52
7	13.7	35.5	19.3	1.84
8	15.2	15.9	4.76	3.34
9A	26.2	48.6	86.8	0.56
9B	26.2	48.6	37.4	1.30

As noted earlier in the section on atmosphere subtractions, ELC band 9 is something of a problem. If we use the FAUST based model for the band 9 atmospheric corrections (case 9A in the table) then the recalibration which we must apply to band 9 is a very large renormalization factor: $\sim 1/2$. On the other hand, if we use the powerlaw

model discussed earlier (case 9B in the table), then band 9 need only be recalibrated by a factor of 4/3. Since the model used in 9B seems to fit the atmospheric profile better, and since the resulting renormalization factor is more consistent with the results for band 5, we prefer the latter approach. Figure 42 shows the IRAS data used in the comparison, Figures 43 to 52 show the ELC data renormalized to the IRAS data.

2.7 SMOOTHING

In preparing data products for the ELC data which are intended to show broad features of the zodiacal background, we applied a sliding boxcar average with a 1s timewidth (~256 samples) to the renormalized data of Section 2.6. The smoothed data for the 9 ELC bands are shown in Figures 53 to 62.

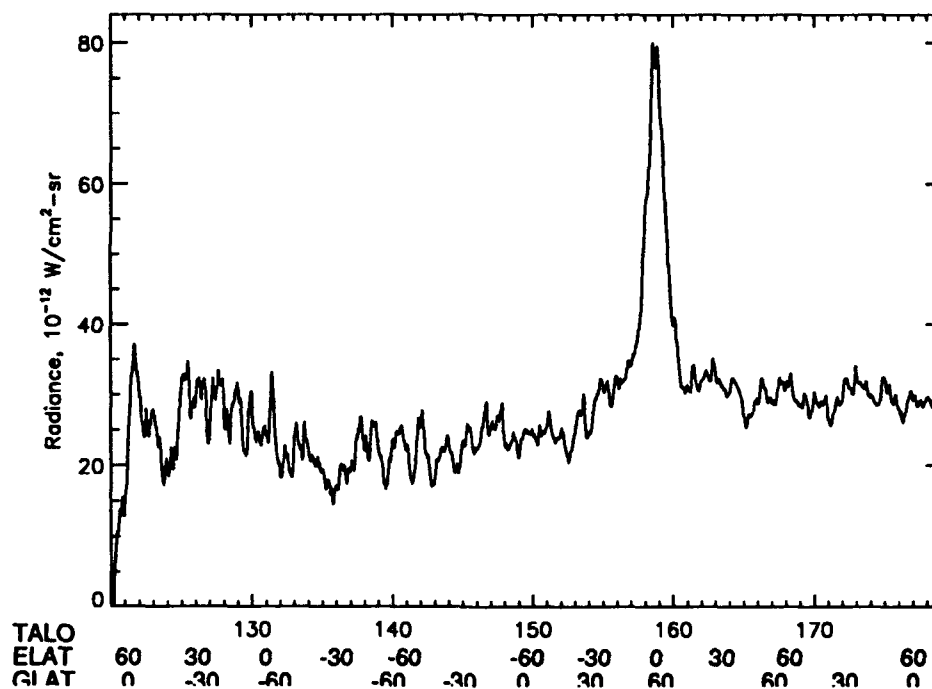


Figure 43: Recalibrated ELC data for Band 1 (5.6 μ).

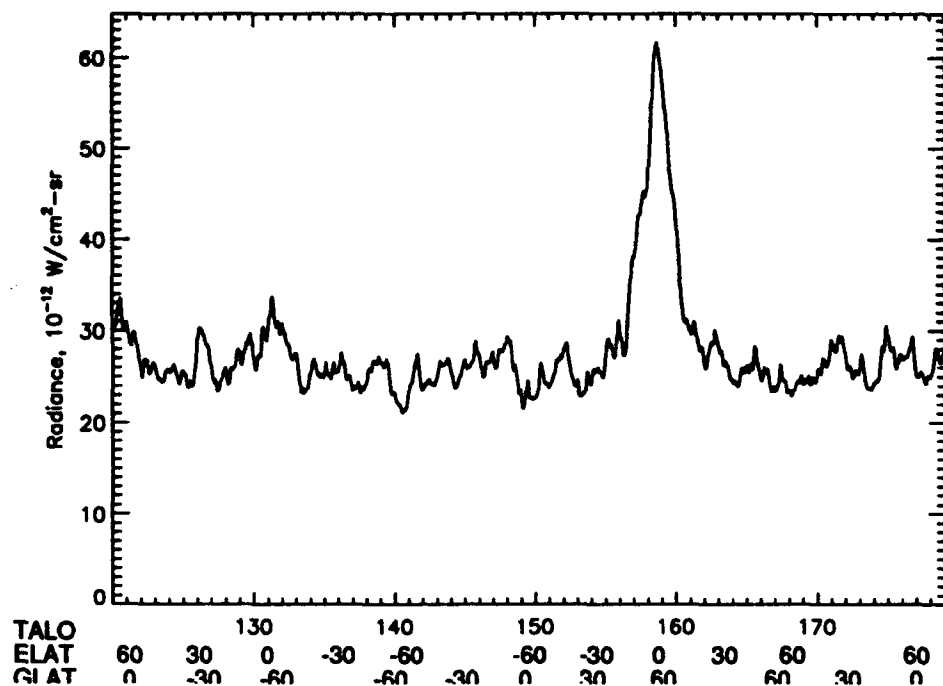


Figure 44: Recalibrated data for ELC Band 2 (9.6 μ).

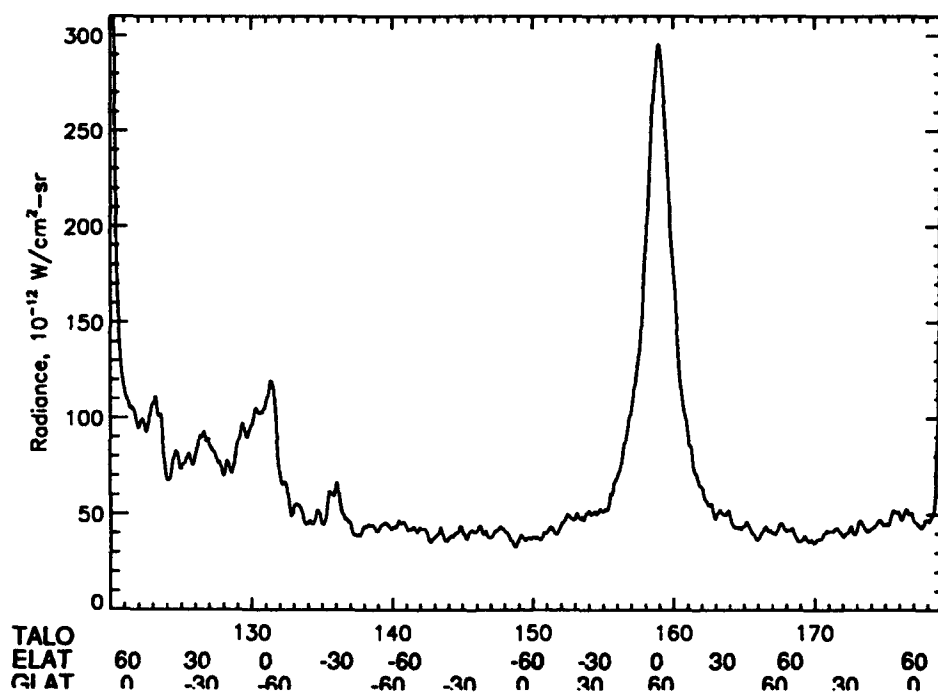


Figure 45: Recalibrated data for ELC Band 3 (10.6 μ).

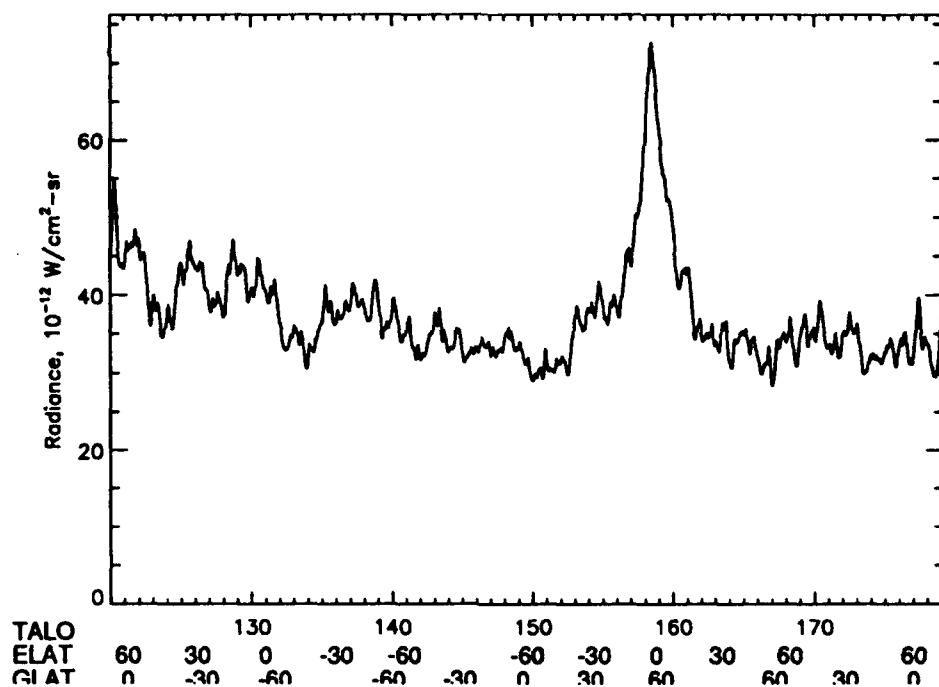


Figure 46: Recalibrated data for ELC Band 4 (11.5 μ).

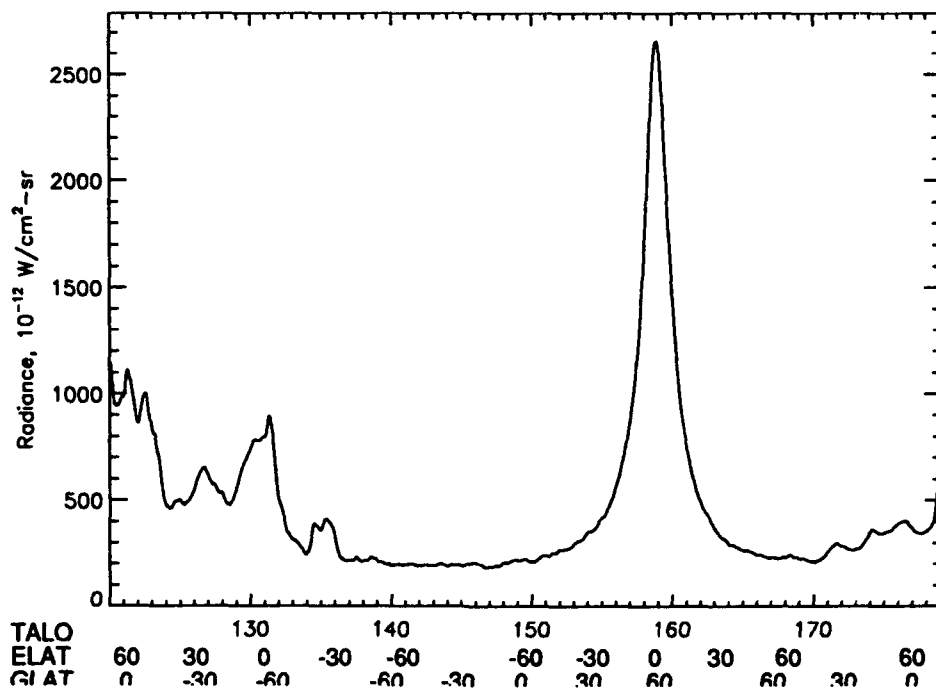


Figure 47: Recalibrated data for ELC Band 5 (12.0 μ).

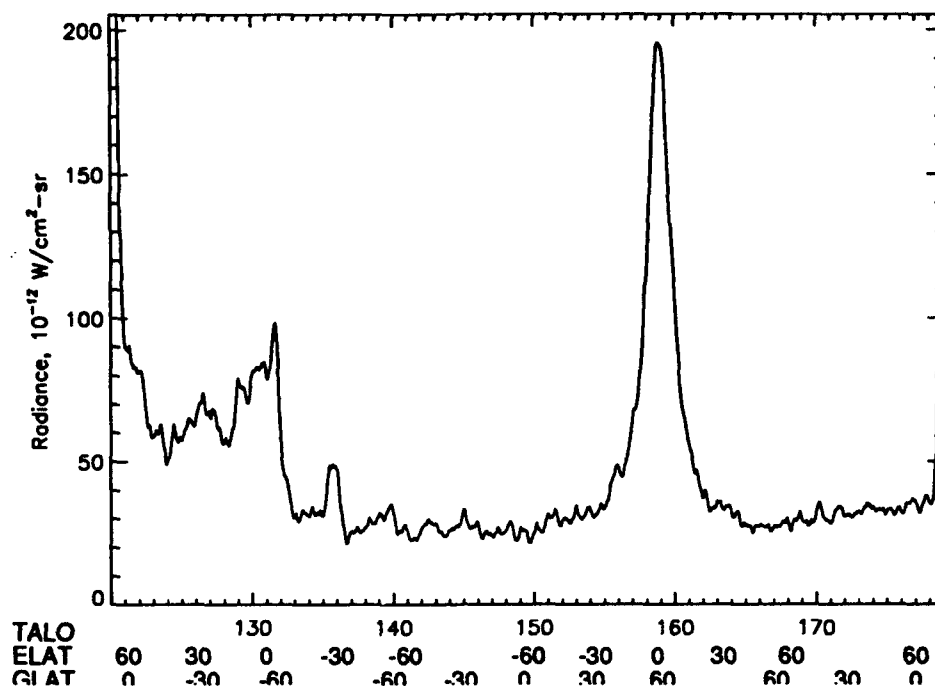


Figure 48: Recalibrated data for ELC Band 6 (12.5 μ).

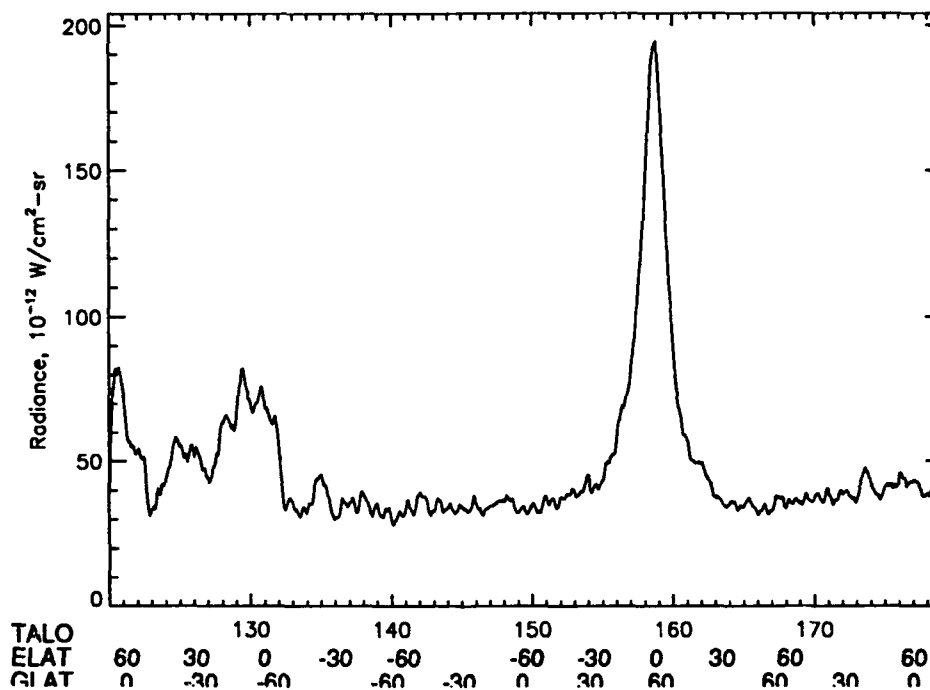
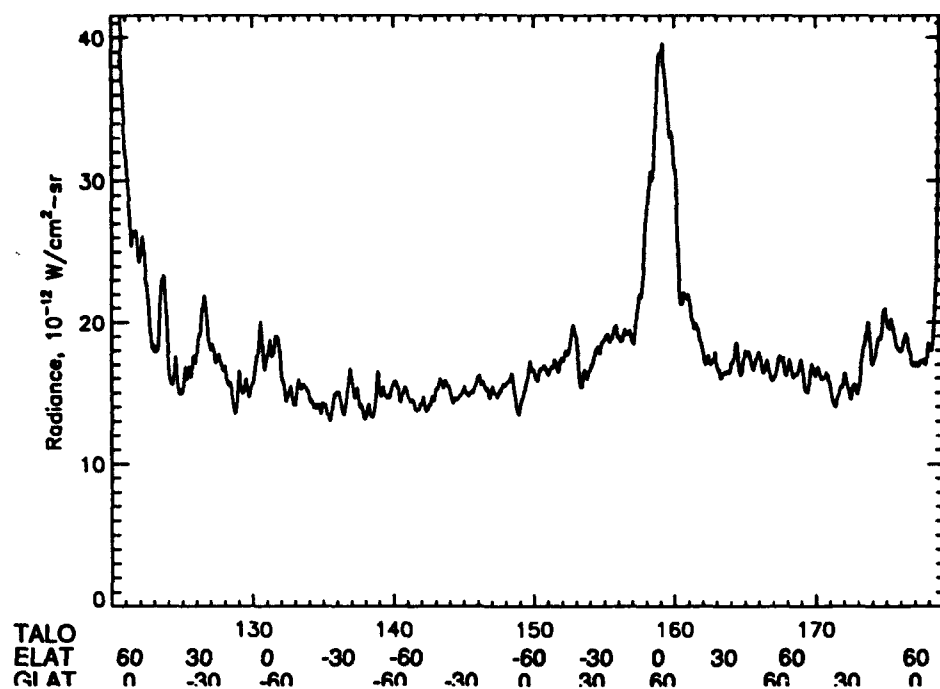


Figure 49: Recalibrated data for ELC Band 7 (13.7 μ).



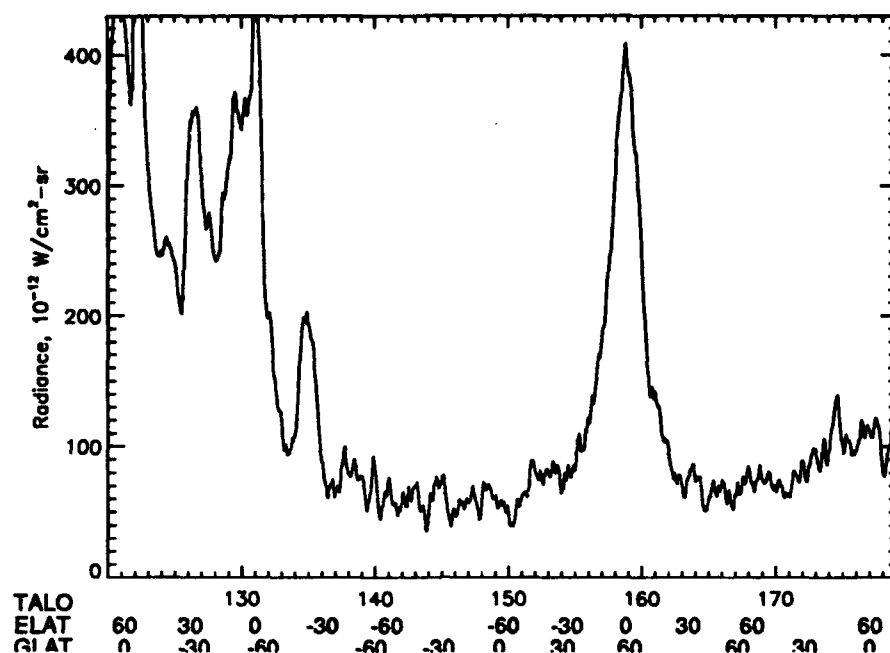


Figure 52: Recalibrated data for ELC Band 9b (26.3 μ). The calibration used for Band 9b is based on a power law model rather than the FAUST model. See discussion in the text.

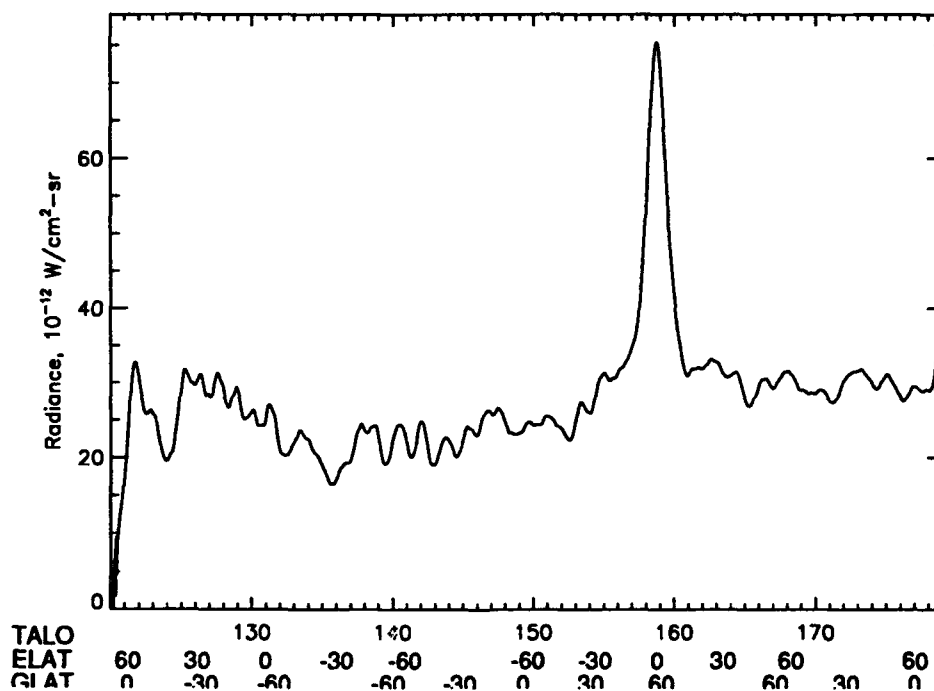


Figure 53: Smoothed, recalibrated ELC data for Band 1.

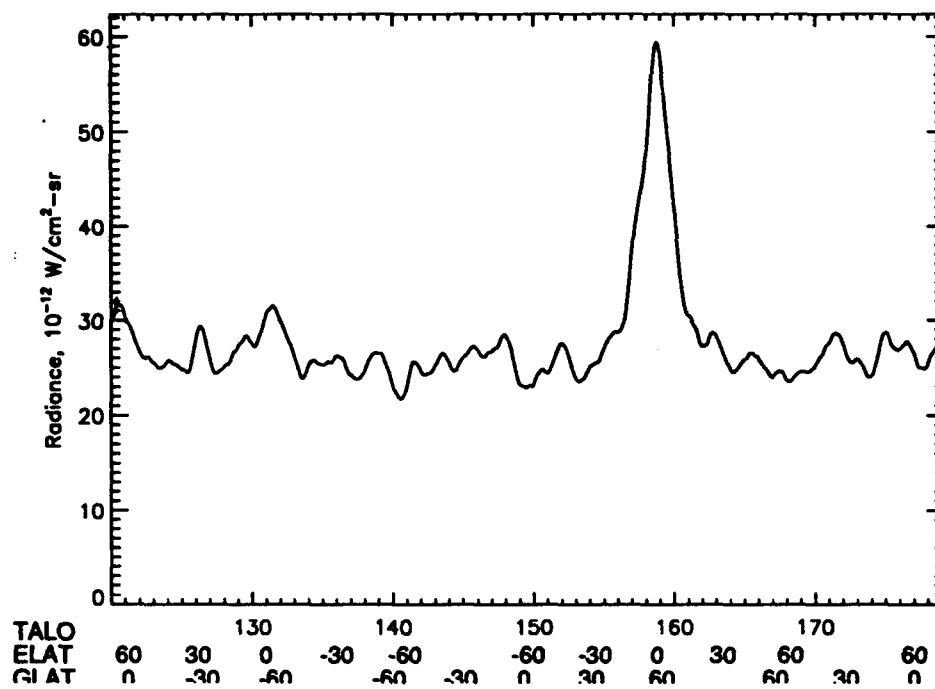


Figure 54: Smoothed, recalibrated ELC data for Band 2.

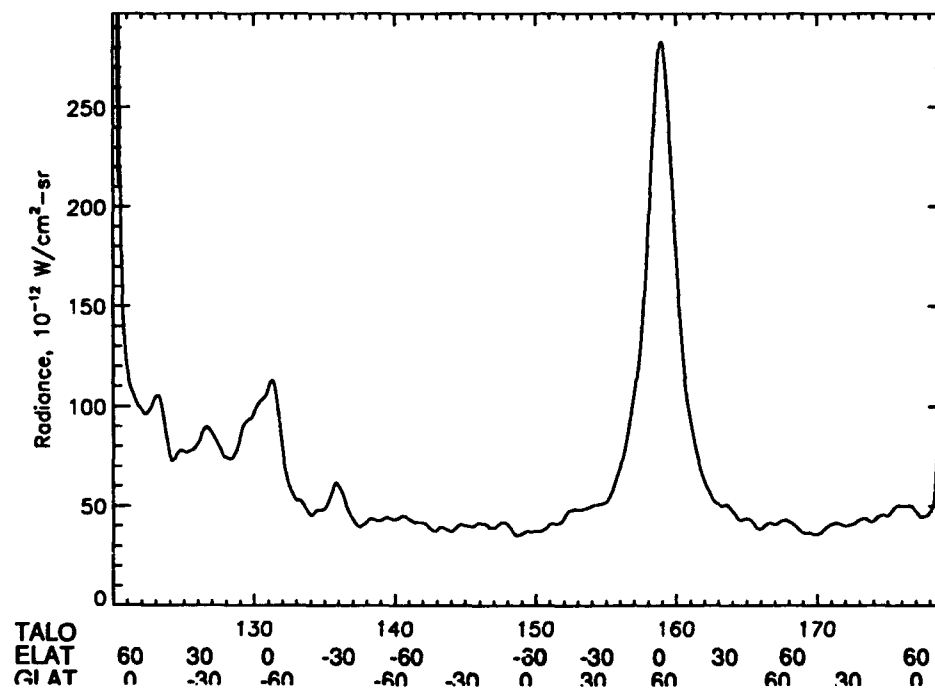


Figure 55: Smoothed, recalibrated ELC data for Band 3.

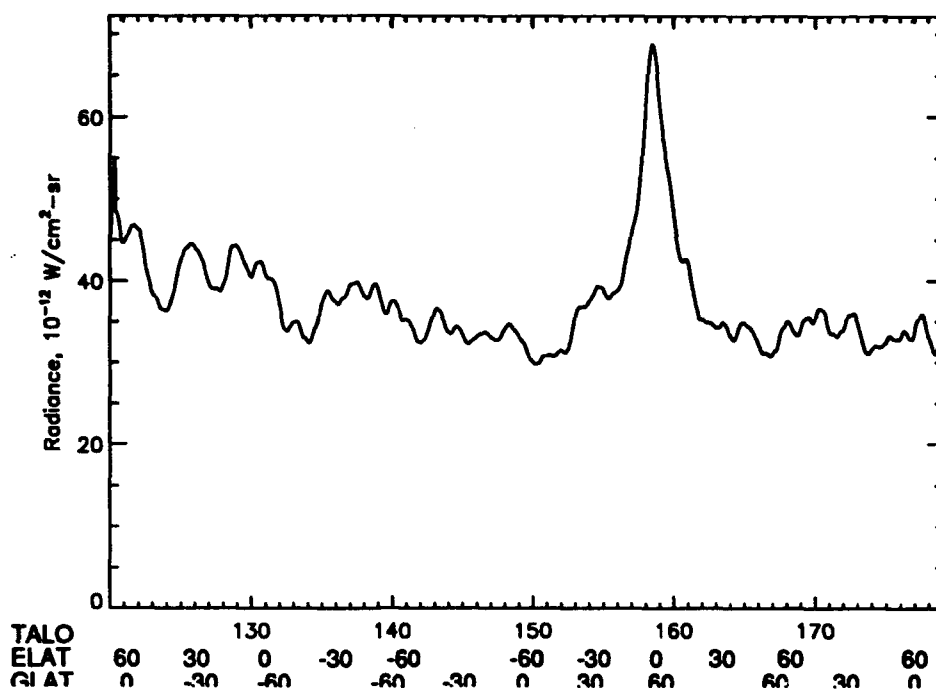


Figure 56: Smoothed, recalibrated ELC data for Band 4.

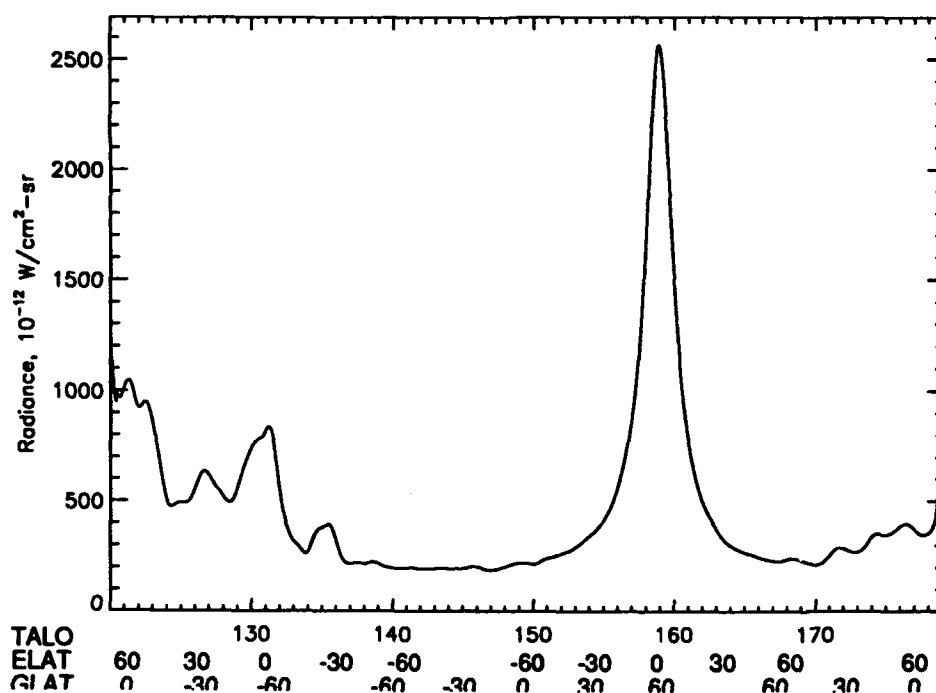


Figure 57: Smoothed, recalibrated ELC data for Band 5.

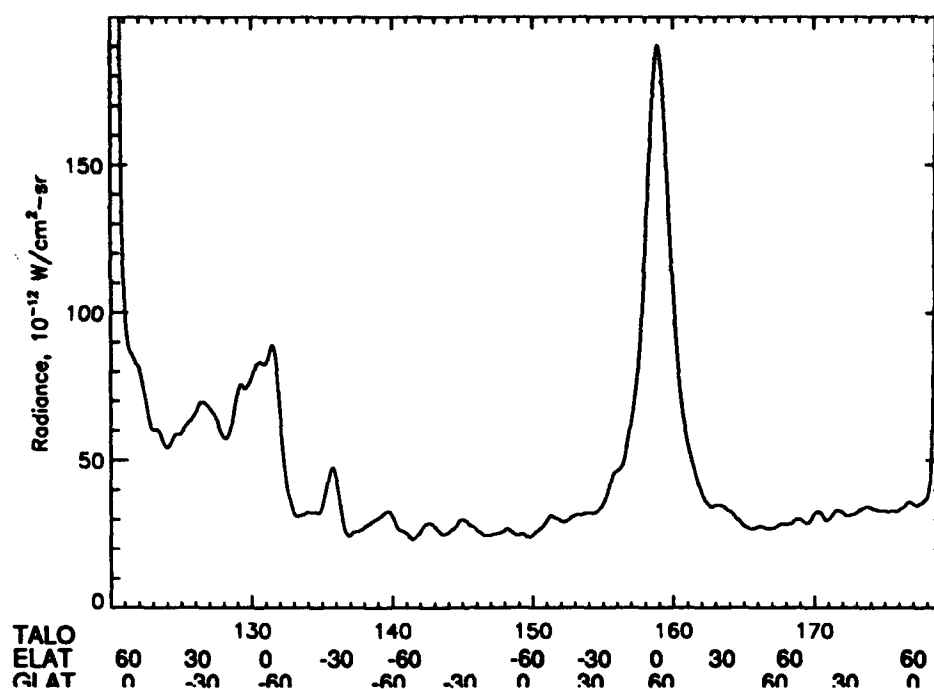


Figure 58: Smoothed, recalibrated ELC data for Band 6.

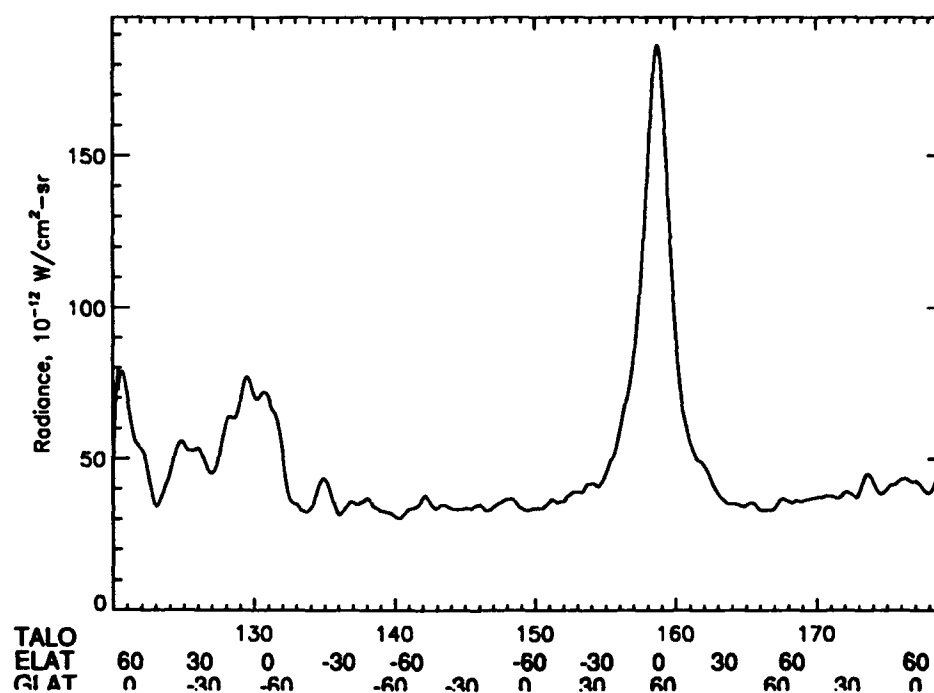


Figure 59: Smoothed, recalibrated ELC data for Band 7.

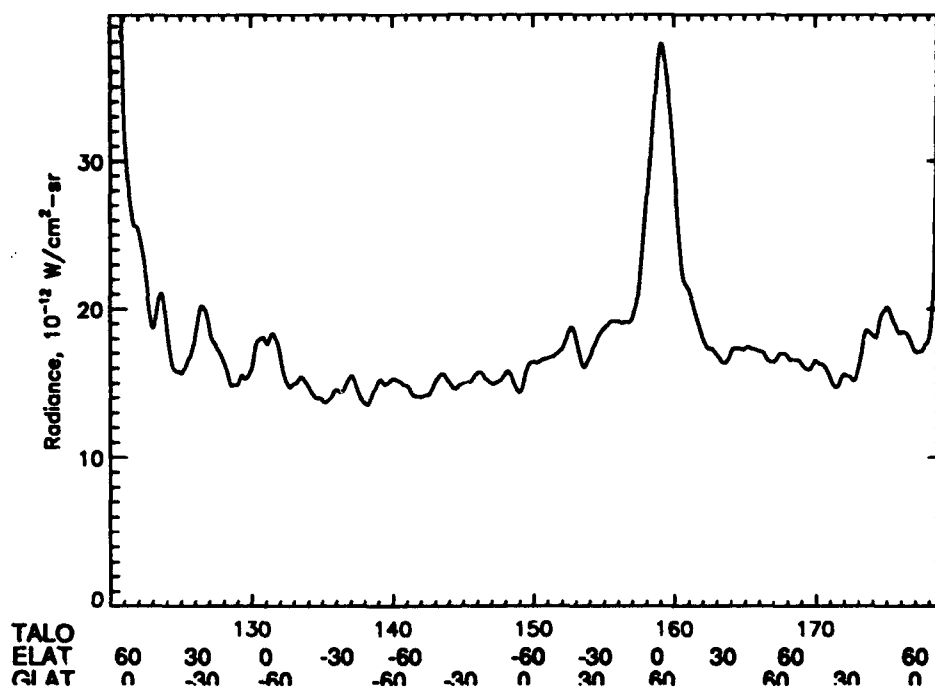


Figure 60: Smoothed, recalibrated ELC data for Band 8.

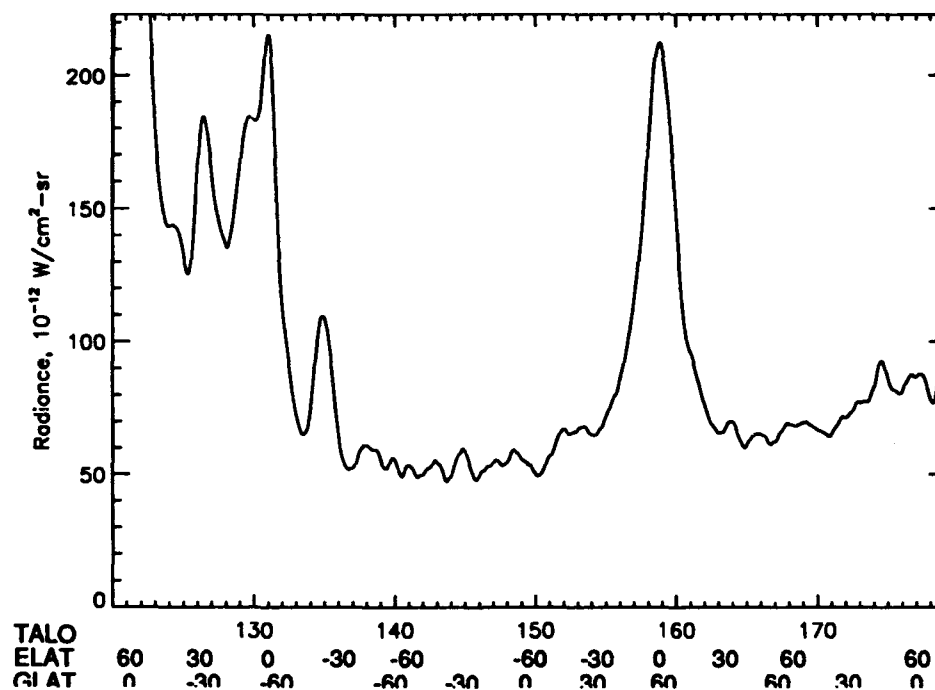


Figure 61: Smoothed, recalibrated ELC data for Band 9a.

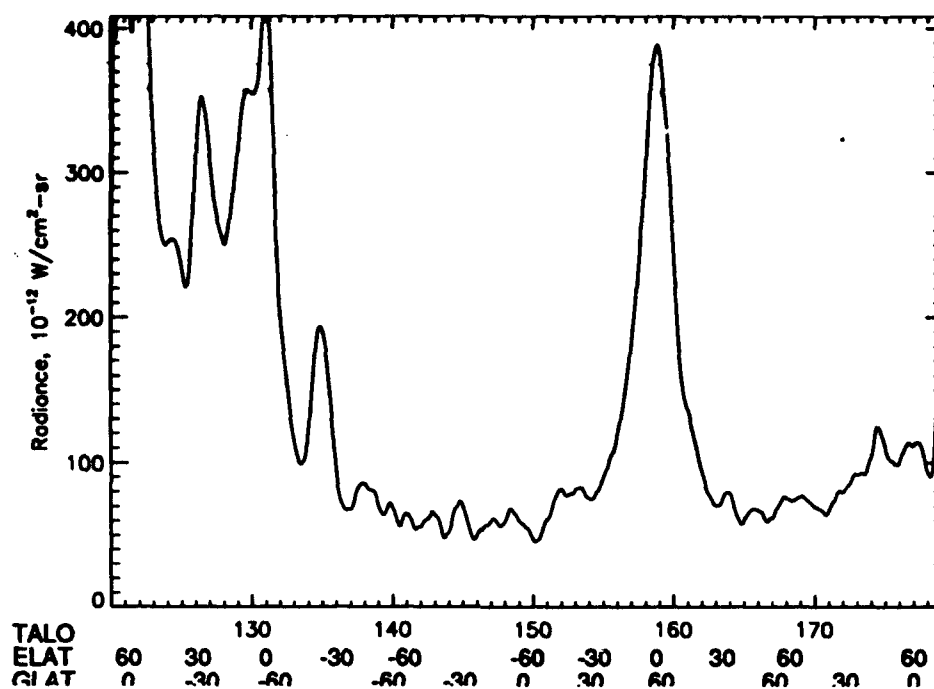


Figure 62: Smoothed, recalibrated ELC data for Band 9b.

3 DISCUSSION

Virtually nothing has been said thus far in this report regarding offaxis response. This is not due to lack of interest or relevance, but rather due to the fact that as with outgassing effects, the ZIP data, with its many zodiacal crossings and profiles, provides a more practical arena in which to develop the needed models. Properly speaking, the interpretation of the ELC results should wait until the ZIP data have been processed and the ZIP-based outgassing and offaxis models have been carefully applied to ELC. But, having arrived at the "final" (i.e. despiked, lowpass-filtered, coadded, atmosphere-corrected, IRAS-recalibrated, and smoothed) form of the ELC data, it is tempting to search the data for interesting features which might manifest themselves in the ELC data alone.

As was shown in Figures 53-62 there are two zodiacal plane crossings, a near sun one at 158s and 19° elongation, and an anti-solar one at 131s and 167° elongation. In some bands (2, 4 & 8) the signal-to-noise at the zodiacal pole calibration point was sufficiently bad that the error bars on the recalibrated data are as large as 50% (band 4).

Unfortunately the anti-solar crossing happens quite early in the flight, and is only observable at a reasonable signal-to-noise level in 5 of the bands. The near-sun crossing on the other hand, shows up clearly in the reprocessed data in all 9 bands and has been used to produce preliminary zodiacal dust spectra. Figures 63 and 64 show the entire processed ELC data set as a function of both time and wavelength. Figure 65 is a spectrum at the near-sun plane crossing. Figure 66 shows spectra of the anti-sun plane crossing and two associated peaks visible in Figure 64. The horizontal extent of the boxes in Figures 65 and 66 represent the bandwidth, while the vertical extent represents the error bar. On the face of it the data seem to show considerable spectral structure in the 9-15 micron region, implying a strong wavelength dependence to the dust emissivity. Referring back to Figures 8 and 12 is more sobering however; neither band has a signal-to-noise ratio, even for the near-sun zodiacal plane crossing, that much exceeds unity. As a result the error bars in Figures 65 and 66 are quite large for these bands and the apparent strong spectral feature of Figures 63 and 64 must be viewed with skepticism.

The strong secondary peaks visible on either side of the anti-solar zodiacal plane crossing are a remarkable feature of the data. These peaks occur at $\pm 28^\circ$ on either side

of the zodiacal plane, and are visible in bands 3, 5, 6, 7, and 9. These peaks may represent zodiacal dust bands which (due to parallax effects) have diverged significantly from the 3° dust bands found by IRAS and COBE at 90° elongation. Note that these side peaks in the antisolar direction are smaller in an absolute sense than the dust band peaks observed at 90° , but they are much larger relative to the zodiacal plane. The surprising difference in amplitude of the peaks relative to the zodiacal plane can perhaps be explained as a geometrical effect. The 90° dust bands and antisolar dust bands are both produced by relatively dense zodiacal dust populations infalling toward the sun in restricted solid angles of sun-centered ecliptic latitude. The apparent band structure is due primarily to the geometry of the observer and the edge of the dust region itself, with the peak amplitude of the dust band occurring in that direction which both maximizes the volume emissivity of the zodiacal dust (a strong function of distance from the sun) and the actual line of sight through the 'dust band' (a strong function of observer viewing angle). The geometry of the peak due to the zodiacal plane crossing on the other hand is not dominated by the intersection of the observer's line of sight with some restricted solid angle, and is instead most effected by the volume emissivity effects.

It appears possible for both the zodiacal plane and dust band brightnesses to decrease as one moves from 90° to 180° in elongation, but for the relative decrease in the dust band brightness to be much less. This coupled with the effect of parallax on the apparent direction of peak dust band brightness may be able to account for the observed structure. While there are some difficulties with such an interpretation, if one assumes instead that the peaks are instead *not* a feature of the zodiacal dust, and instead represent some local phenomenon, then one has several unlikely coincidences to explain:

- If the peaks are assumed to come from some sort of outgassing or contamination event, then one must explain the fact that there are two peaks, both of which are of nearly identical amplitude and width, that are observed at symmetrical positions above and below the zodiacal plane. One might suppose that the trajectory of the booster might trace an arc on the sky which could have intersected the scan path of the Long Roll twice, but the scan geometry was chosen (in part) precisely to exclude such a possibility. Furthermore, it would have been an astoundingly unfortunate trick of geometry for any such intersections to have occurred symmetrically spaced about the anti-solar zodiacal plane crossing.

- The locations of the peaks do not correspond to any known extrasolar objects. There is a galactic plane crossing approximately 4.5 seconds before the first of the peaks in question, but the slew rate of the sensor is nearly 7° per second, so the peak appears some 30° away from the galactic plane. In addition, the second peak is nowhere near the galactic plane.
- The peaks' spectral signatures closely resemble the signature of the zodiacal plane crossings. Furthermore, if the peaks were due to outgassing it seems unlikely that their relative sizes would be nearly identical (as compared to the zodiacal peaks) across all of the bands.
- If the peaks were assumed to be signal processing artifacts, then one must explain why the peaks are evident in the ELC band 5 data (e.g. Figure 9) prior to the application of the first of our pipeline stages.

All of these factors suggest to us that these putative dust bands are a real feature of the zodiacal background. If they should in fact prove to be genuine, then they would represent a *major discovery about the zodiacal dust*. We will be investigating this matter intensely as we process the ZIP data, and the project moves into the analysis phase.

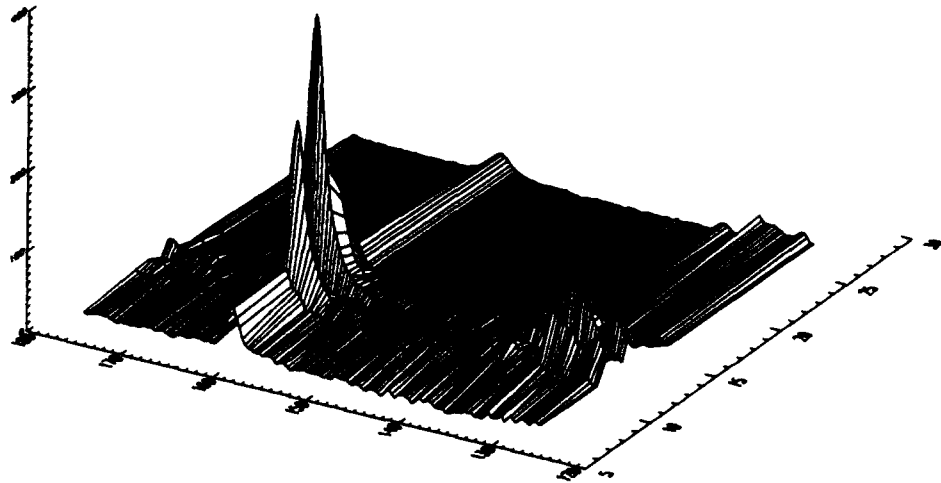


Figure 63: Surface plot showing ELC sensor response ($10^{-12} \text{ W/cm}^2 \cdot \text{sr} \cdot \mu$) as a function of time and wavelength. The temporal response is derived from the recalibration ELC data using a bilinear rebinning which reduces the data resolution by a factor of 100.

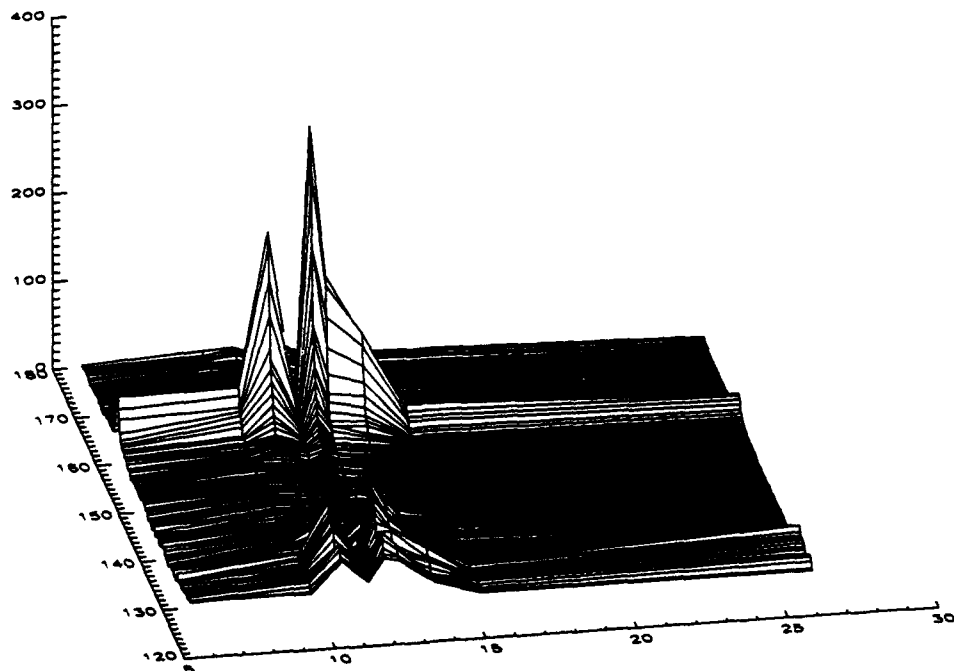


Figure 64: Surface plot showing ELC sensor response ($10^{-12} \text{ W/cm}^2 \cdot \text{sr} \cdot \mu$) as a function of time and wavelength, but with the projection chosen to emphasize the spectral features in the data.

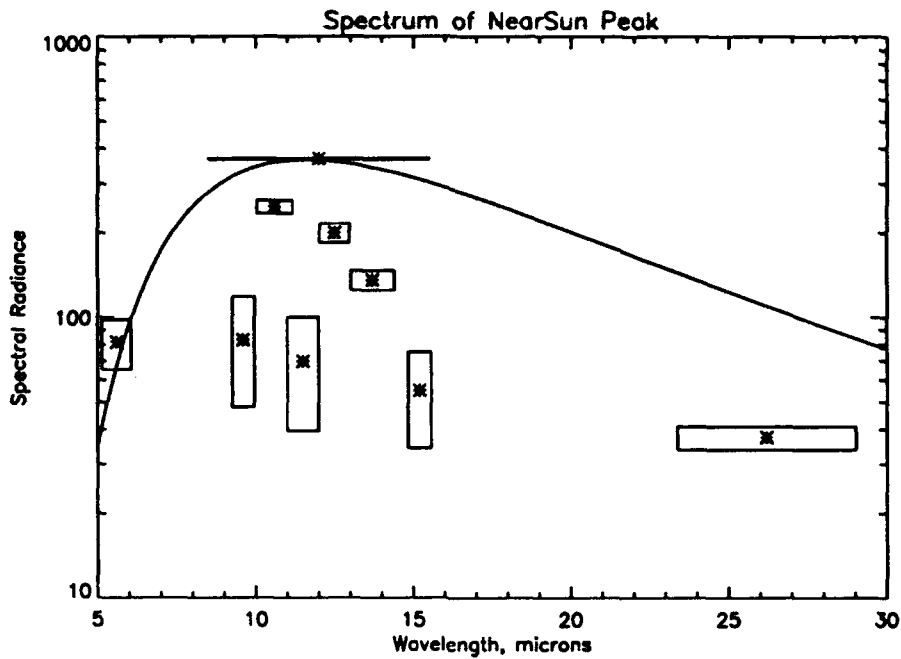


Figure 65: Spectrum of the zodiacal plane as measured by ELC in the near sun crossing at 158s TALO.

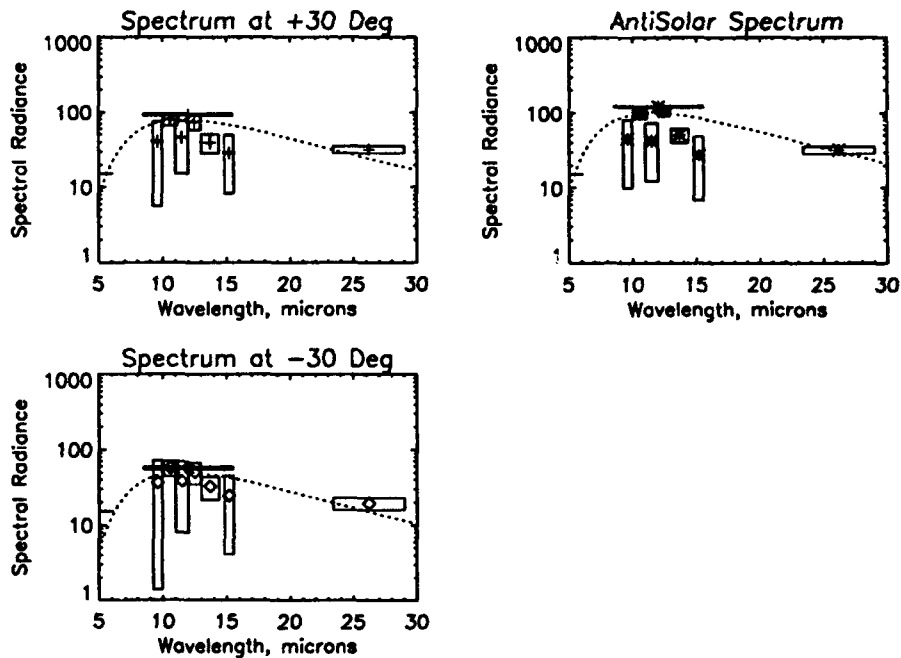


Figure 66: Spectrum of the zodiacal plane and putative 'dust-band' features measured by ELC.

4 SUMMARY

We have completed a preliminary reprocessing of the ELC Long Roll data, and have extracted much useful information about the zodiacal light from it.

Two zodiacal plane crossings were observed (one was of high quality, and one was of fair quality). The spectra from the two plane crossings appear to show features consistent with astronomical silicates, or possibly crystalline olivine. In addition, in the time series we see structures that may be related to zodiacal bands.

The reader is cautioned that our present results are incomplete in the sense that to date, we have not applied any outgassing or out of field of view rejection (OFVR) corrections to the data. As our analysis of the ZIP-1 and ZIP-2 data proceeds we will be able to use the outgassing and OFVR models which we develop from ZIP to add additional stages to the ELC pipeline (after the present coaddition stage and before the present atmospheric correction phase).

It is also possible that in its final form the ELC data will be processed using a parabolic low-pass filter rather than the present Butterworth filter.

REFERENCES

1. A.J. Mazzella, R.M. Rao, and S.A. Lacaire, in "ELC Data Re-processing", TR #8504, RDP Corporation (October 1985).
2. "ELK-1 [sic] Design Review Handbook", Air Force Geophysics Laboratory (December 1982), internal report.
3. "ELC-1 Tech Data, Payload Information, Background Measurements Program, (Payload No. A24.260)", Air Force Geophysics Laboratory, Aerospace Instrumentation Division (September 1983), internal report.
4. "Critical Design Review of ELK [sic] I", TR 1516-CDR-14, Space Vector Corporation (December 1982).
5. "Mission Readiness Review of ELC I", TR 1516-MRR-20, Space Vector Corporation (July 1983).
6. W.L. Wolfe, and G.J. Zissis, "The Infrared Handbook", Infrared Information Analysis Center, Environmental Research Institute of Michigan, (1989).
7. W.H. Press, B.P. Flannery, S.A. Teukolsky, and W.T. Vetterling, "Numerical Recipes in C", Cambridge University Press (1990).
8. A.J. Mazzella, J.R. Palys, W.A. Smith, and S.A. Lacaire, "The ELC-1 Aspect Solution", TR #8505, RDP Corporation (March 1986).
9. W.K. Cobb, S.V. Burdick, and T.L. Murdock, "Infrared Contamination From Solid Rocket Motor Thrust Termination Exhaust Plumes", General Research Corporation, 1597-01-90TR (August 1990).
10. L.J. Rickard and S.W. Stemwedel, "ZIP-IRAS Inter-Calibration", in IR Celestial Backgrounds Review Meeting Proceedings, Mission Research Corp. (Oct 1990).
11. L.J. Rickard and S.W. Stemwedel, private communication with Dr. Stephan D. Price.

APPENDIX A: ELC DETECTOR INTERCOMPARISONS

This appendix contains a series of figures showing how various ELC detectors within the same ELC bands behave relative to one another. For the two band detectors there are two panels shown; the first shows the radiance of one detector against the radiance of the other, the second shows the ratio of the two detectors as a function of time. For the four band detectors there are three pairs of panels shown corresponding to various combinations of the detectors.

The graphs in all of these figures show radiance on a logarithmic scale -- as a result, when one goes to low radiance levels, there is considerable quantization due to the digital readout electronics observable in the signals. In the ratio plots for bands 3 and 5 in particular, at low background signals (i.e., from 139 - 152 s), the dispersion in the ratios gets quite large.

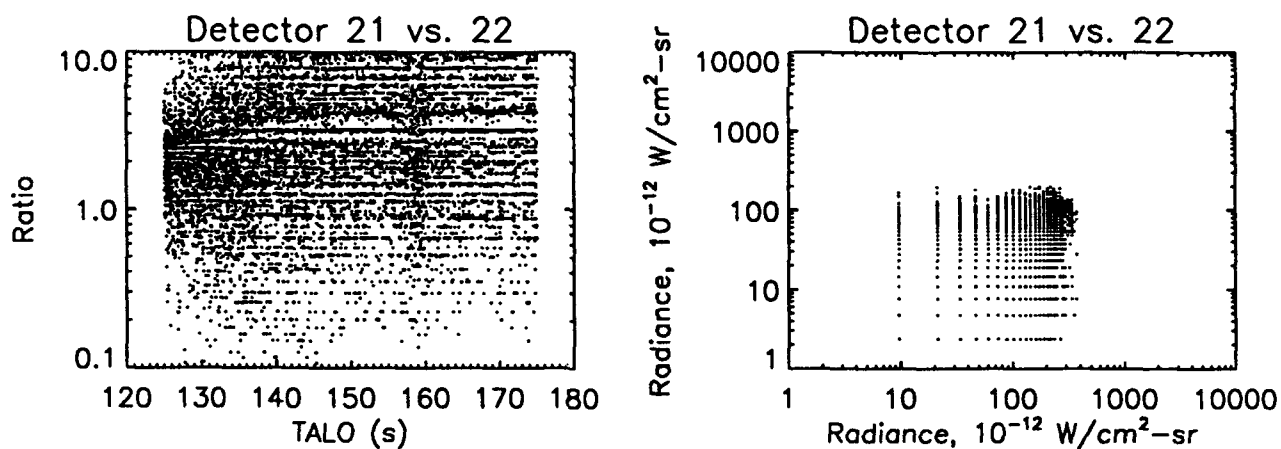


Figure A-1: Detector responses for ELC Band 1. The right hand panel shows detector 21 plotted against detector 22. The left hand panel shows the time evolution of the ratio of the two detector signals.

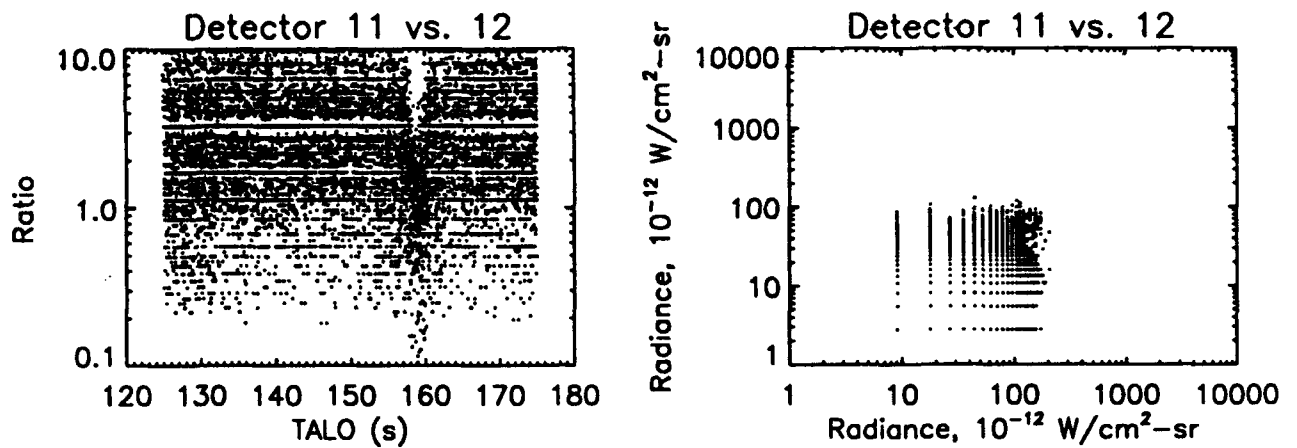


Figure A-2: Detector responses for ELC Band 2. The right hand panel shows detector 11 plotted against detector 12. The left hand panel shows the time evolution of the ratio of the two detector signals.

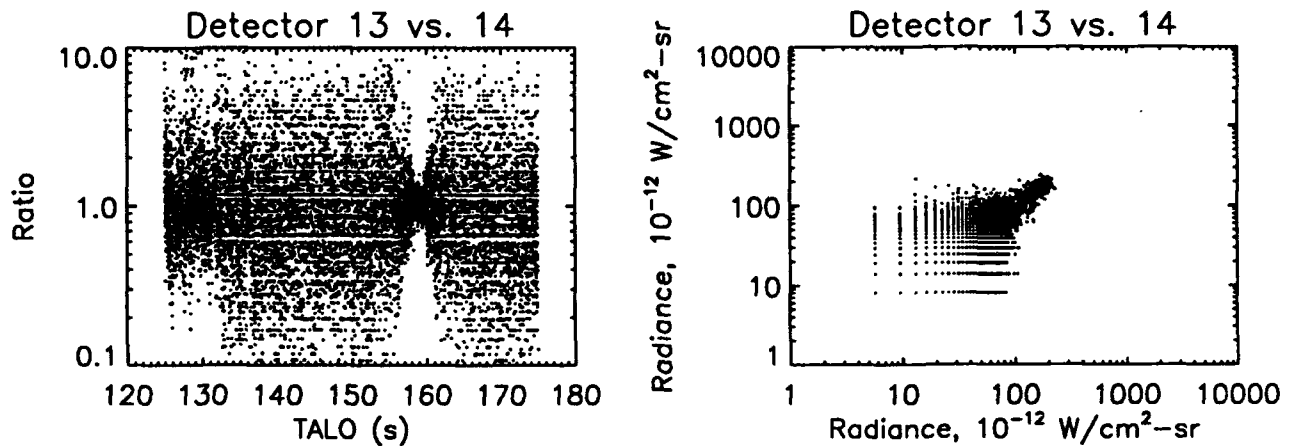


Figure A-3: Detector responses for ELC Band 3. The right hand panel shows detector 13 plotted against detector 14. The left hand panel shows the time evolution of the ratio of the two detector signals.

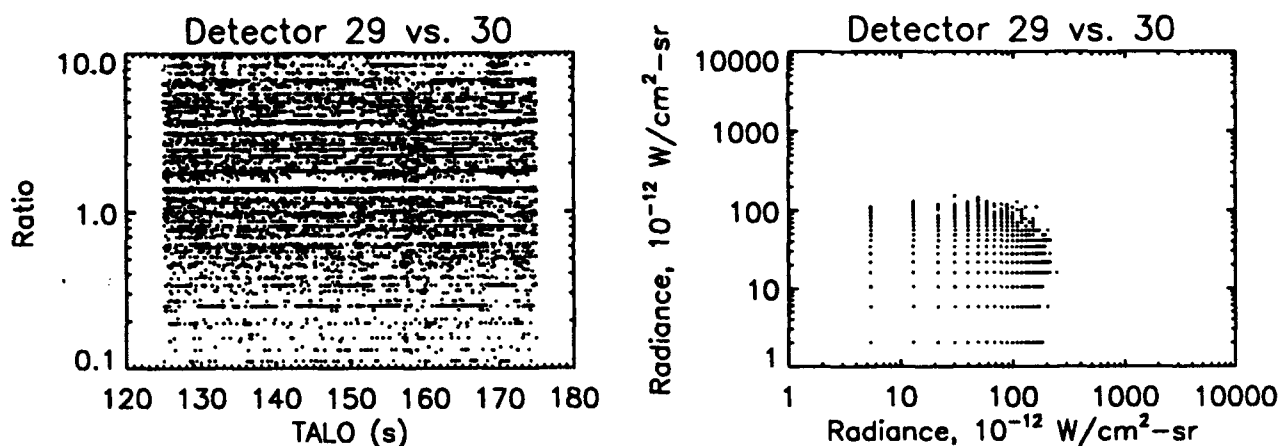


Figure A-4: Detector responses for ELC Band 4. The right hand panel shows detector 29 plotted against detector 30. The left hand panel shows the time evolution of the ratio of the two detector signals.

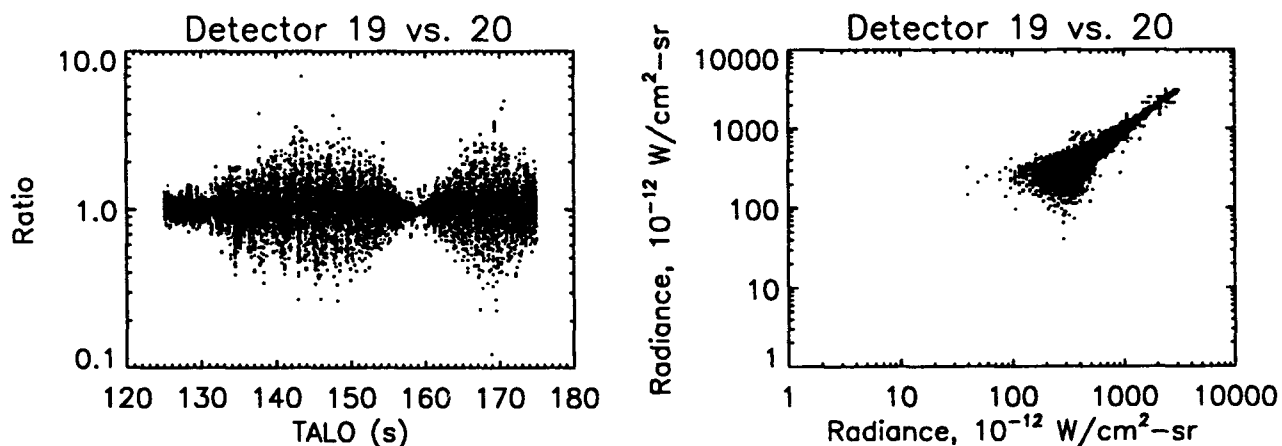


Figure A-5: Detector responses for ELC Band 5. The right hand panel shows detector 19 plotted against detector 20. The left hand panel shows the time evolution of the ratio of the two detector signals.

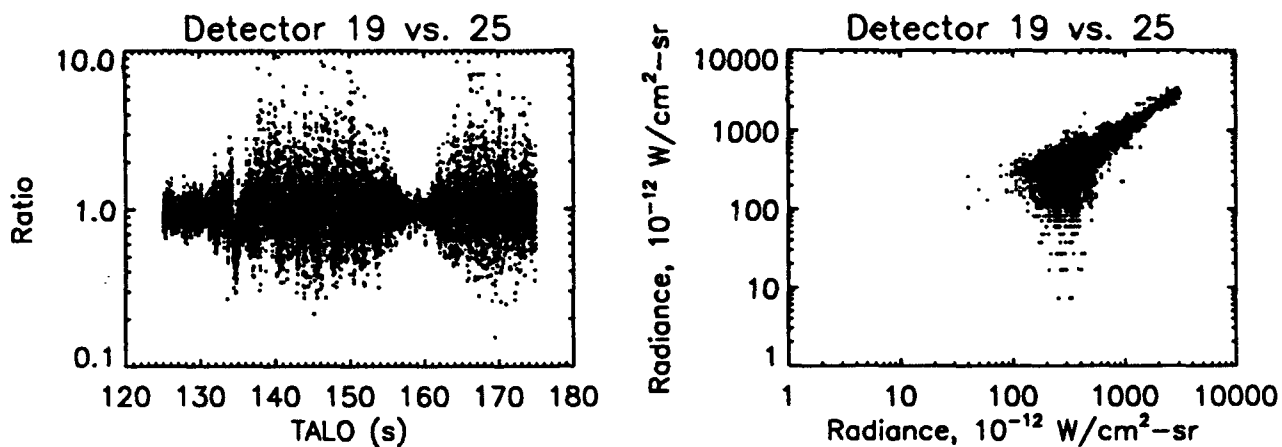


Figure A-6: Detector responses for ELC Band 5. The right hand panel shows detector 19 plotted against detector 25. The left hand panel shows the time evolution of the ratio of the two detector signals.

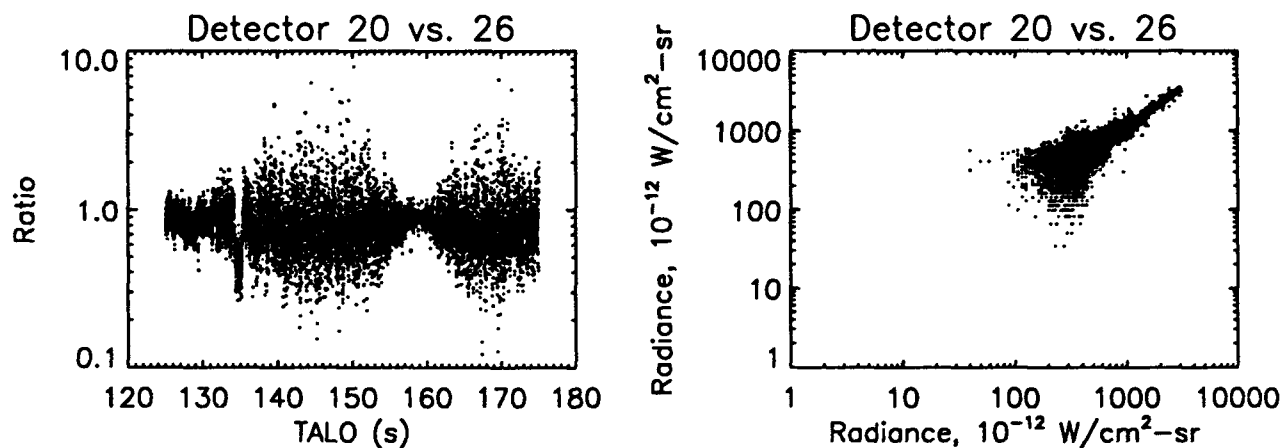


Figure A-7: Detector responses for ELC Band 5. The right hand panel shows detector 20 plotted against detector 26. The left hand panel shows the time evolution of the ratio of the two detector signals.

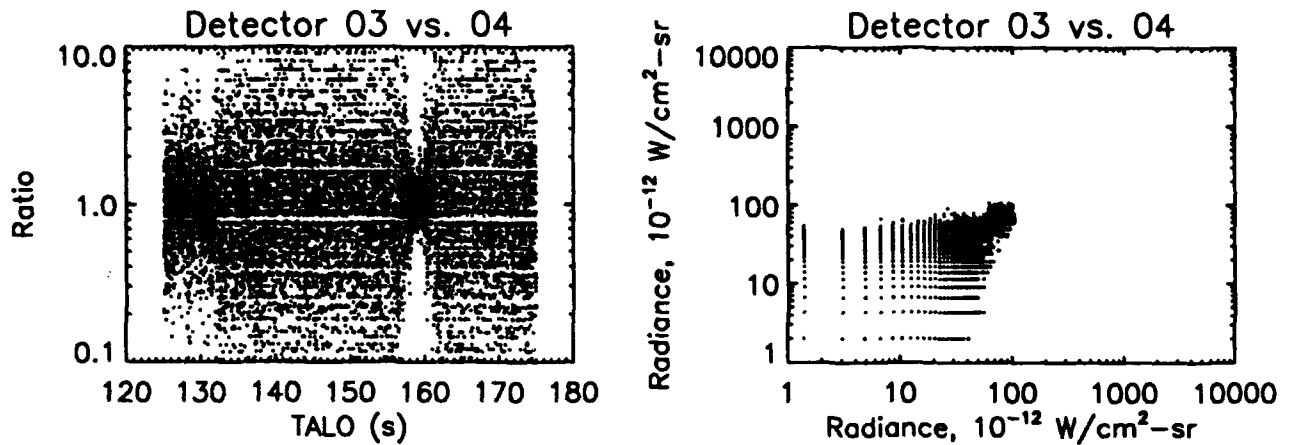


Figure A-8: Detector responses for ELC Band 6. The right hand panel shows detector 3 plotted against detector 4. The left hand panel shows the time evolution of the ratio of the two detector signals.

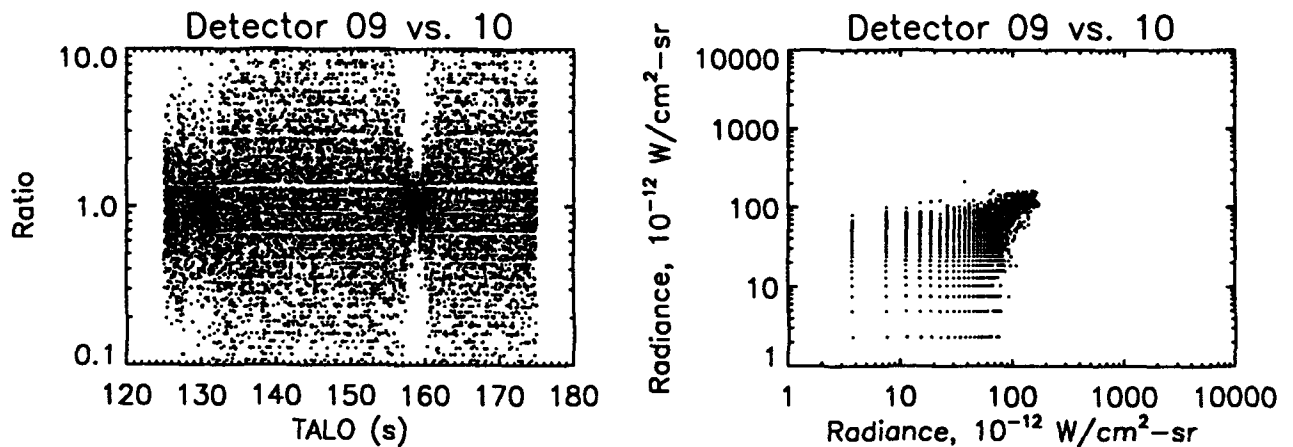


Figure A-9: Detector responses for ELC Band 7. The right hand panel shows detector 9 plotted against detector 10. The left hand panel shows the time evolution of the ratio of the two detector signals.

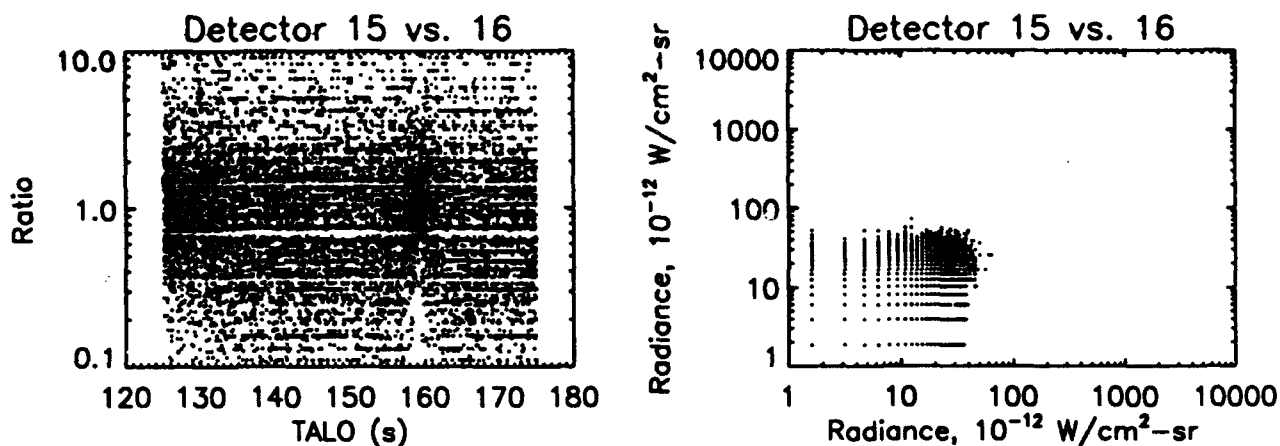


Figure A-10: Detector responses for ELC Band 8. The right hand panel shows detector 15 plotted against detector 16. The left hand panel shows the time evolution of the ratio of the two detector signals.

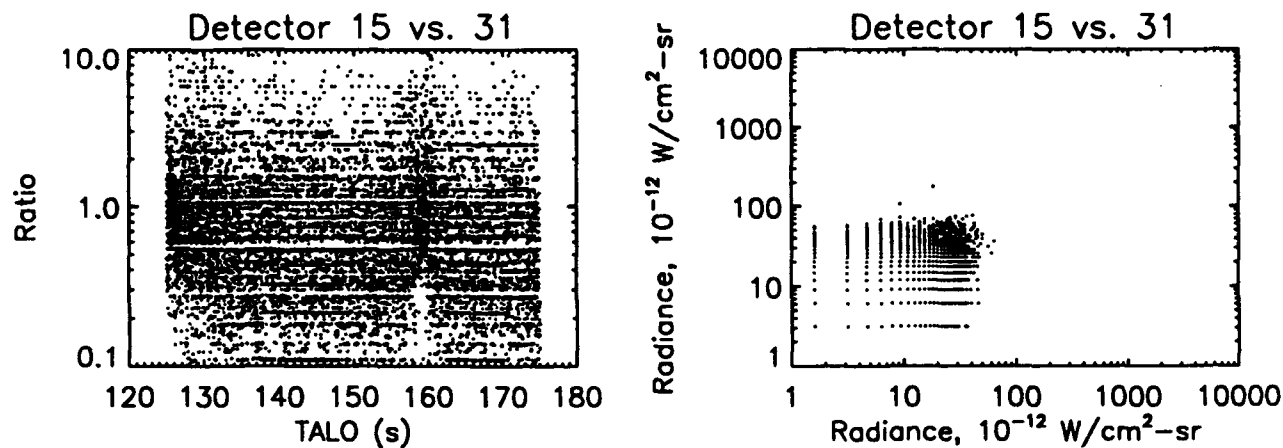


Figure A-11: Detector responses for ELC Band 8. The right hand panel shows detector 15 plotted against detector 31. The left hand panel shows the time evolution of the ratio of the two detector signals.

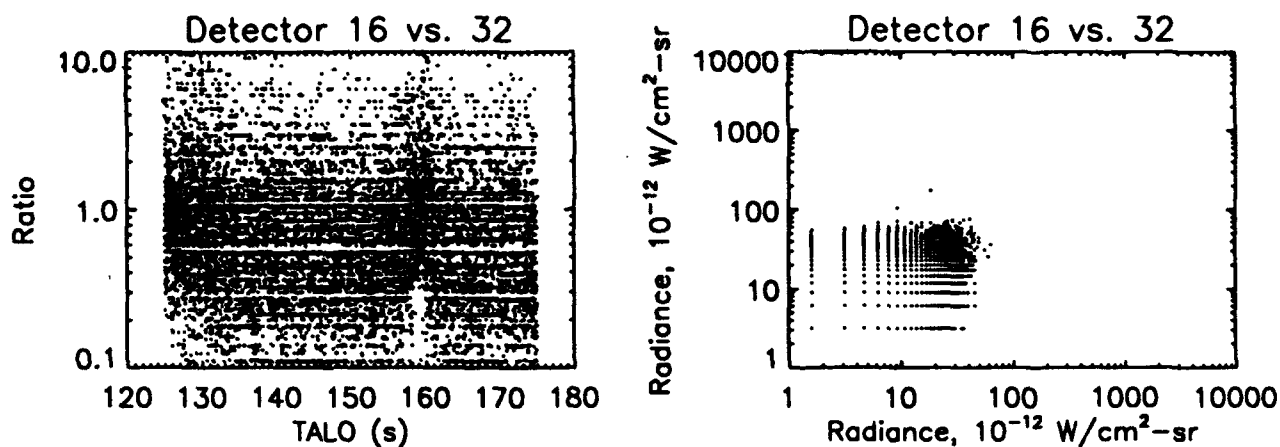


Figure A-12: Detector responses for ELC Band 8. The right hand panel shows detector 16 plotted against detector 32. The left hand panel shows the time evolution of the ratio of the two detector signals.

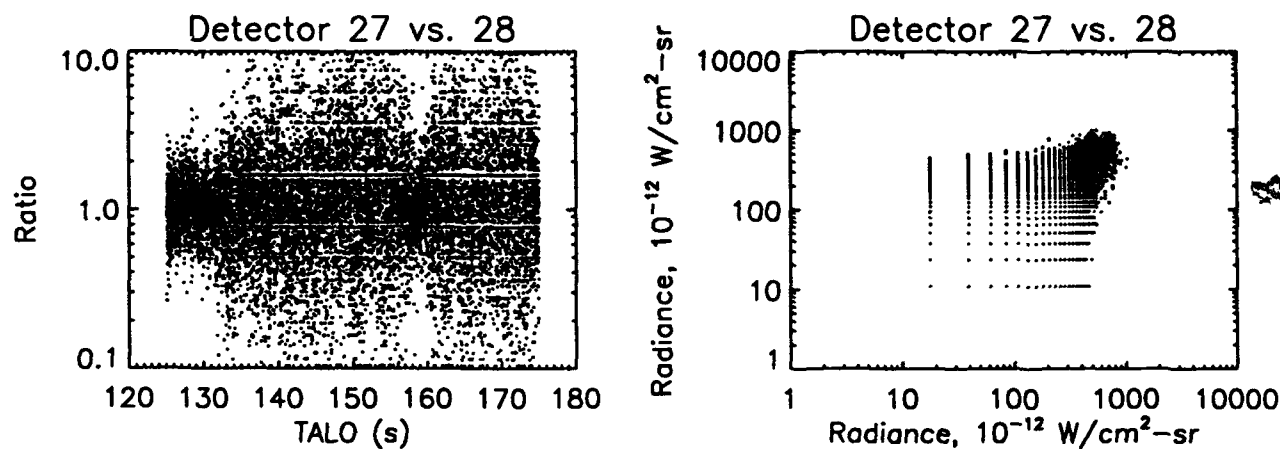


Figure A-13: Detector responses for ELC Band 9. The right hand panel shows detector 27 plotted against detector 28. The left hand panel shows the time evolution of the ratio of the two detector signals.

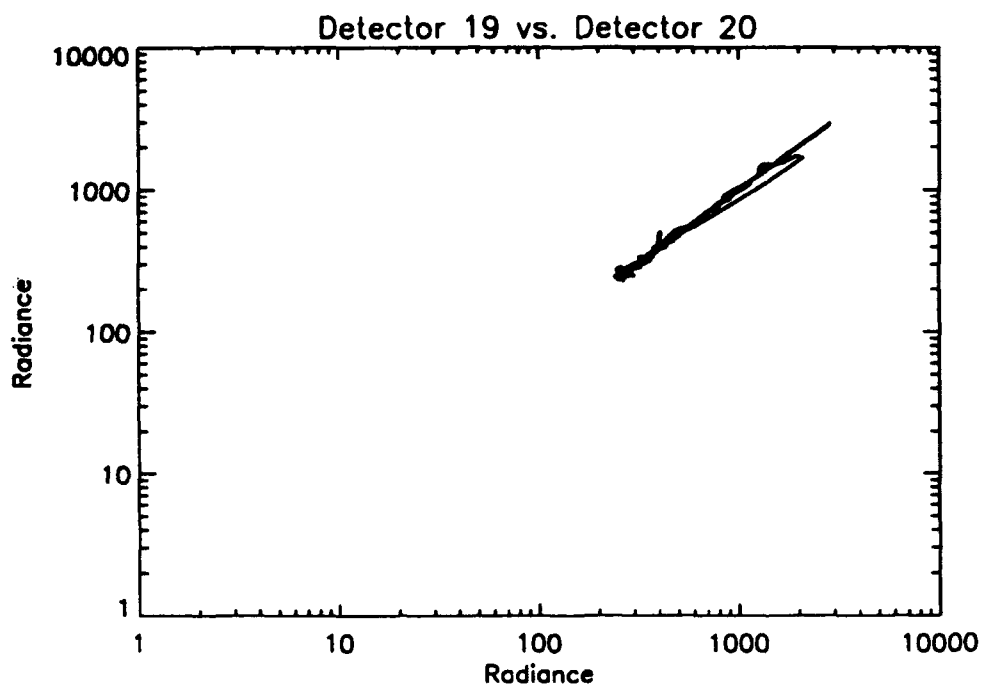


Figure A-14: Diagram showing improvement in detector vs. detector behavior after cleaning and despiking for representative pair of detectors within the same band.